

# Dissertation

---

## First-principles studies of CrN-based materials

carried out for the purpose of obtaining the degree of PhD, submitted at TU Wien, Faculty of  
Mechanical and Industrial Engineering

**MSc. Liangcai Zhou**

Mat.Nr.: 1135521

Getreidemarkt 9/E308

A-1060 Wien

under the supervision of

Univ.Prof. Dipl.-Ing. Dr.mont. Paul Heinz Mayrhofer

Institute of Materials Science and Technology, E308

Vienna, May 2015

---

This work was supported by the Austrian Science Fund in the  
framework of START Project Y371.

*Affidavit*

I declare in lieu of oath, that I wrote this thesis and performed the associated research myself, using only literature cited in this volume.

---

Wien, May 2015

---

Liangcai Zhou

---

# Abstrakt

---

Das ansteigende Anforderungsprofil an Schneidwerkzeuge macht die Entwicklung von neuartigen Hartstoffschichten bezüglich Härte, thermischer Stabilität, Zähigkeit, tribologischer Eigenschaften, Verschleiß-, Korrosions- und Oxidationsbeständigkeit erforderlich. CrN ist für seine große Härte, Verschleiß- und Oxidationsbeständigkeit sowie chemische Reaktionsträgheit bekannt, womit es Eigenschaften besitzt, die allesamt wichtig für die Anwendung von Hartstoffschichten sind. Darüber hinaus ist CrN, aufgrund seiner magnetischen und elektronischen Eigenschaften, auch für die Grundlagenforschung von großem Interesse. Das Ziel dieser Arbeit ist es, mittels „ab initio“ Berechnungen im Rahmen der Legierungstheorie, ein physikalisches Verständnis für das Verhalten von auf CrN basierenden Werkstoffen zu entwickeln sowie eine Brücke zwischen Theorie und Experiment zu schlagen um letztlich Vorhersagen für die Herstellung neuer Hartstoffschichten treffen zu können.

Zunächst wurden die Auswirkungen verschiedener Berechnungsmethoden auf die berechneten Eigenschaften von CrN sorgfältig untersucht. Es konnte gezeigt werden, dass magnetischer Grundzustand, Korrelationseffekte und auch Temperatur einen signifikanten Einfluss auf die Phasenstabilität von CrN haben. Um auch mögliche Abweichungen der „as-deposited“ Schichten von einer perfekten 1:1 Stöchiometrie zu berücksichtigen, wurde der Einfluss von Stickstoffleerstellen auf die Phasenstabilität, die strukturellen und mechanischen Eigenschaften und die elektronische Struktur von kubischem B1 CrN und Cr-TM-N (TM = Mo und W) analysiert. Die Ergebnisse deuten darauf hin, dass die experimentell beobachtete Stickstoffunterstöchiometrie eher auf Stickstoffleerstellen als auf andere Punktdefekte zurückzuführen ist. Eine Tendenz zu Bildung von Stickstoffleerstellen in kubischem Cr-Mo-N und Cr-W-N konnte anhand einer gekoppelten Auswertung von Gitterparameter, Mischungsenthalpie und elastischer Eigenschaften theoretisch vorhergesagt und experimentell bestätigt werden. Der chemischen Zusammensetzung von Substitutionsmischkristallen in

---

kubischem Cr-Mo-N und Cr-W-N und der auftretenden Stickstoffleerstellen kann mit der Summenformel  $\text{Cr}_{1-x}\text{TM}_x\text{N}_{1-0.5x}$  exakt beschrieben werden. Die gute Übereinstimmung von experimentell bestimmten Gitterparametern, Mo- und W-abhängigen Stickstoffleerstellen, elastischen Eigenschaften und den jeweiligen berechneten Werten der Modelle mit der chemischen Zusammensetzung  $\text{Cr}_{1-x}\text{Mo}_x\text{N}_{1-0.5x}$  und  $\text{Cr}_{1-x}\text{W}_x\text{N}_{1-0.5x}$  erlauben ein besseres Verständnis dieser komplexen Materialsysteme.

Die Einflüsse des Legierens wurden hinsichtlich chemischer Trends bezüglich Phasenstabilität, struktureller und mechanischer Eigenschaften systematisch untersucht. Eine starke Abhängigkeit der elastischen Konstanten und der strukturellen sowie mechanischen Eigenschaften bezüglich der chemischen Zusammensetzung konnte für ternäre kubische B1  $\text{Cr}_{1-x}\text{Al}_x\text{N}$  Legierungen vorausgesagt werden.

Die Elektronische Struktur und die Gitterfehlpassung konnten mit der Mischungsenthalpie verknüpft werden und diese ermöglichen Vorhersagen bezüglich der Tendenz zur isostrukturellen Entmischung. Die Auswirkungen der chemischen Zusammensetzung auf die Duktilität wurden für die ternären und quaternären kubischen B1 Phasen  $\text{Cr}_{1-x}\text{TM}_x\text{N}$  und  $\text{Cr}_{1-x-y}\text{Al}_x\text{TM}_y\text{N}$  untersucht. Es konnte gezeigt werden, dass die Duktilität in erster Linie vom Bindungscharakter (und nicht nur von der Valenzelektronenkonzentration) der Phasen abhängt und somit stark mit der elektronischen Struktur zusammenhängt.

Zusätzlich wurde gezeigt, dass die maximale Löslichkeit von Al in quaternären kubischen  $\text{Cr}_{1-x-y}\text{Al}_x\text{TM}_y\text{N}$  (TM=Sc, Y, Ti, Zr, Hf, V, Nb, und Ta) Phasen mit dem Gitterparameter der entsprechenden TMN in Verbindung gesetzt werden kann.

Die erarbeiteten chemischen Trends (mit Hilfe detaillierter Dichtefunktionaltheorie Berechnungen) ermöglichen eine tiefere Einsicht in experimentelle Beobachtungen und dienen als wichtige Richtlinien für die Entwicklung von neuartigen Hartstoffschichten.

---

# Abstract

---

The increasing demands on the performance of cutting tools foster the development of novel hard coatings in terms of hardness, thermal stability, toughness, tribological properties, wear, corrosion and oxidation resistance. From the application point of view, CrN is valued for its high hardness, wear and oxidation resistance, and chemical inertness, all being important for protective coating applications. It also receives considerable attention from the basic materials science due to its interesting magnetic properties and electronic structures. The aim of this thesis is to reveal physics behind CrN-based materials behavior, to bridge theoretical calculations and experimental observations, and to provide materials trends to allow a design of new coatings, all using first principles calculations within the framework of the alloy theory.

Firstly, the impact of various calculational approaches on the predicted properties of CrN is thoroughly studied. It is demonstrated that the magnetic state, strong correlations effects, and temperature show significant influence on the phase stability of CrN. Due to the deviation of the nitrogen composition from a perfect 1:1 stoichiometry in the as-deposited coatings, the influence of nitrogen vacancies on phase stability, structural and mechanical properties, and electronic structures is discussed for cubic B1 CrN and Cr-TM-N (TM = Mo and W). The results indicate that the experimentally observed N understoichiometry is likely to be related to N vacancies rather than to any other point defect. The tendency for nitrogen deficiency in cubic Cr-Mo-N and Cr-W-N solid solutions is predicted by a comprehensive evaluation of the lattice spacing, mixing thermodynamics, and elastic properties, and experimentally confirmed by means of X-ray diffraction. A more precise and informative chemical formula of  $\text{Cr}_{1-x}\text{TM}_x\text{N}_{1-0.5x}$  is proposed to describe the chemical composition of cubic Cr-Mo-N and Cr-W-N solid solutions. The excellent agreement between experimentally obtained lattice parameters, Mo- and W-dependent nitrogen content, elastic properties and their calculated values for our model descriptions,  $\text{Cr}_{1-x}\text{Mo}_x\text{N}_{1-0.5x}$  and  $\text{Cr}_{1-x}\text{W}_x\text{N}_{1-0.5x}$ , allows to understand

---

these complex material systems.

The alloying effects are systematically investigated in terms of chemical-related trends, including phase stability, structural and mechanical properties. A strong compositional dependence of the elastic properties is self-consistently predicted for cubic B1  $\text{Cr}_{1-x}\text{Al}_x\text{N}$  ternary alloys. The connection between electronic structures and lattice mismatch with the mixing enthalpy is illustrated and used to predict the tendency for isostructural decomposition. The chemical-related trend for the ductility is predicted for cubic B1 ternary  $\text{Cr}_{1-x}\text{TM}_x\text{N}$  and quaternary  $\text{Cr}_{1-x-y}\text{Al}_x\text{TM}_y\text{N}$  solid solutions. The ductility trends show predominant dependence on the bonding character of phases, which is strongly linked with the electronic structure and indicates that using valence electron concentrations, as a sole indicator of the ductility trends, is not enough. Finally, it is found that the maximum solubility of Al in the quaternary cubic  $\text{Cr}_{1-x-y}\text{Al}_x\text{TM}_y\text{N}$  (TM=Sc, Y, Ti, Zr, Hf, V, Nb, and Ta) phase can be related to the corresponding lattice spacing of TMN. These chemical-related trends provide insight to the experimental observations and are important guidelines for the design of novel hard coatings.

---

# Acknowledgements

---

First of all, I would like to express my sincerest gratitude to my supervisor Prof. Paul Heinz Mayrhofer and my mentor Dr. David Holec for their guidance, great help and constant support during the whole research work and also the period of more than three years in Austria. I am very lucky to find a great supervisor, and a great mentor.

I would like to especially thank the whole members of thin Film Group for their friendship and support in many difficult ways, who gave me a feeling that I am in a big family with so enjoyable atmosphere and so much fun. Special thanks for their great help in life.

I am very thankful to Prof. Jörg Neugebauer, Dr. Blazej Grabowski, and Dr. Fritz Körmann from the Max-Planck-Institut für Eisenforschung GmbH for the stimulating discussion and also the kind permission to use their super-cluster, as well as the great assistance from Martin Friák and other people there.

I also thank gratefully to the people at the Department of Physical Metallurgy and Materials Testing in Leoben for the great time and support from my previous research group in China.

Finally, I want to say thank to my parents, my wife and also my two little angels, who always remind me what is really important in life and thank all my friends and study colleagues for the great time in Austria.

---

# Contents

---

Abstrakt .....	iii
Abstract.....	v
Acknowledgements .....	vii
Contents.....	viii
1 Introduction .....	1
1.1 Hard Ceramic Coatings .....	1
1.2 CrN .....	2
1.3 State-of-the-art coating design.....	7
1.3.1 CrAlN .....	8
1.3.2 Alloying CrN with transitional metal .....	10
1.3.3 Quaternary Cr-Al-TM-N .....	12
1.4 Computational Materials Science.....	14
1.4.1 Recent theoretical work .....	14
1.4.2 The aim of present thesis .....	17
References .....	18
2 Calculational methods .....	24
2.1 Density Functional Theory.....	24
2.1.1 Formulation of the many-body problem .....	24
2.1.2 Theorems of Hohenberg and Kohn.....	27
2.1.3 Kohn-Sham equations .....	28
2.1.4 Exchange-correlation potential .....	29
2.1.5 Projector Augmented Wave method .....	31
2.2 Treatment of disordered alloys .....	33
2.3 Phonons.....	37
2.3.1 Lattice dynamics .....	37

---

2.3.2	Finite displacement method .....	39
2.3.3	Quasiharmonic approximation.....	40
2.4	Prediction of mechanical properties.....	42
2.5	Introduction to VASP and phonopy .....	45
	References .....	46
3	Structural stability and thermodynamics of CrN magnetic phases.....	48
3.1	Motivation.....	48
3.2	Methods.....	51
3.2.1	Static DFT calculations .....	51
3.2.2	Phonon calculations .....	53
3.2.3	Thermodynamic properties .....	56
3.2.4	Experimental details.....	57
3.3	Results and Discussion .....	58
3.3.1	Elastic constants and mechanical stability .....	58
3.3.2	Dynamical stability .....	60
3.3.3	Thermodynamic stability and thermodynamic properties of CrN.....	65
3.4	Conclusions.....	72
	References .....	73
4	Impact of point defects on the electronic structure of paramagnetic CrN.....	77
4.1	Motivation.....	77
4.2	Calculational details.....	77
4.3	Results and discussion .....	78
4.3.1	Stability of point defects in CrN .....	78
4.3.2	N K-edge of CrNx.....	80
4.4	Conclusions.....	84
	References .....	85
5	First-principles study of elastic properties of cubic Cr <sub>1-x</sub> Al <sub>x</sub> N alloys .....	87
5.1	Motivation .....	87

---

5.2	Methodology .....	87
5.3	Results and discussion .....	90
5.3.1	Equilibrium properties .....	90
5.3.2	Accuracy of paramagnetic state model .....	92
5.3.3	Elastic properties.....	95
5.4	Conclusions.....	99
	References .....	101
6	Impact of TM elements alloyed in CrN on structural and thermodynamic properties .....	104
6.1	Motivation .....	104
6.2	Computational methods.....	104
6.3	Results and discussion .....	105
6.3.1	Structural properties .....	105
6.3.2	Phase stability .....	109
6.3.3	Alloying influence on mechanical behavior .....	112
6.4	Conclusions.....	113
	References .....	115
7	Off-stoichiometry in $\text{Cr}_{1-x}\text{TM}_x\text{N}_y$ (TM=Mo and W).....	117
7.1	Motivation.....	117
7.2	Methods .....	117
7.2.1	Calculation details.....	117
7.2.2	Experimental details.....	118
7.3	Results and discussion .....	119
7.4	Conclusions.....	126
	References .....	127
8	Structure, mechanical and electric properties of quaternary Cr-Al-TM-N.....	129
8.1	Motivation .....	129
8.2	Computational methods .....	129
8.3	Results and discussions .....	130

---

8.3.1 Impact of the quaternary additions on maximum Al solubility in the cubic phase .....	130
8.3.2 Structural properties .....	131
8.3.3 Mechanical properties .....	134
8.4 Conclusions.....	137
References .....	139
APPENDIX A.....	140
List of publications .....	145
Other publications .....	147
Curriculum Vitae .....	148

# Chapter 1

## Introduction

### 1.1 Hard Ceramic Coatings

The most prominent property of hard ceramic coatings, e.g. thin films designed to protect bulk tools, is their hardness, which is a macroscopic property describing the resistance against a plastic deformation mediated through dislocation motion [1,2]. There are two main factors greatly influencing hardness: microstructure of the films, and nature of the bonding [3]. Resulting microstructural features are mostly related to the experimental procedure, such as ageing temperature, deposition method *etc* [1].

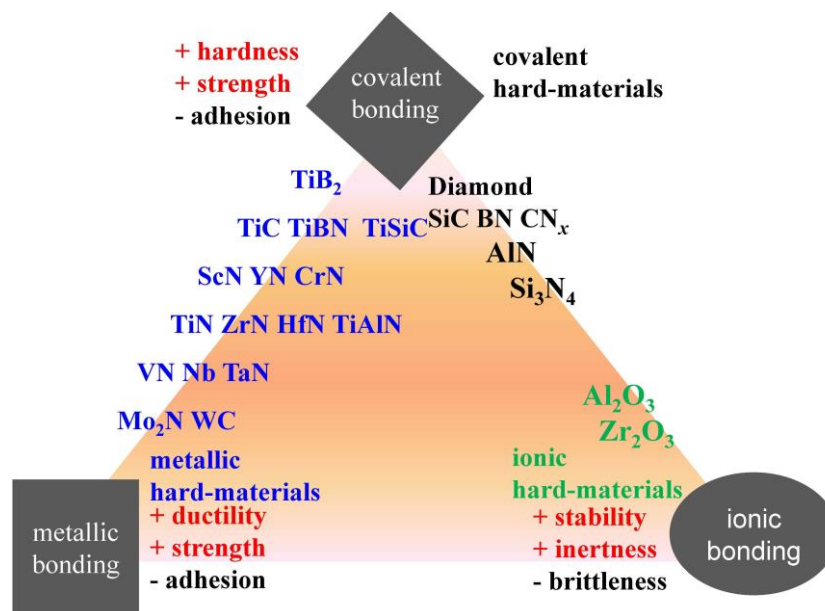


Figure 1.1: Classification of hard coatings according to their bonding character and their change in properties (modified after Ref. [3,4,7]).

The bonding character of a material, on the other hand, is an intrinsic property highly determining materials properties, and generally is a mixture of metallic, ionic, and covalent

---

contributions [4-6]. These describe the type of an interaction of electrons between the atoms. Figure 1.1 shows a schematic diagram distributing the hard ceramic materials into three groups according to their chemical bonding, and the corresponding change in their properties. The covalent and/or ionic bonding are the essential contributions to the high hardness and phase stability, while a distinct metallic character is strongly responsible for ductility as well as good adhesion strength. The mixture of bonding character endows the carbides, borides, nitrides and oxides with outstanding properties for various applications. Each of the different groups of hard materials exhibits advantages and disadvantages with respect to special applications. In particular, the transition metal nitrides (TMN), crystallizing in the face centered cubic (fcc) B1 structure (space group  $Fm-3m$ , NaCl prototype), are widely used as protective hard coatings of cutting tools, due to their outstanding properties such as high hardness, thermal stability, wear, and corrosion resistance [8-10].

## 1.2 CrN

Among the transition metal nitride family, chromium nitride (CrN) is especially valued for its high hardness ( $\sim 24$  GPa), wear resistance, oxidation resistance, and chemical inertness [11-13]. Due to these excellent physical and chemical properties, CrN coatings show great potential for a wide range of applications in automotive, aerospace, tooling *etc.* areas [12]. It adopts a paramagnetic (PM) cubic B1 (space group  $Fm-3m$ , NaCl prototype) structure with a lattice constant  $a=4.14$  Å [14] at room temperature, and becomes antiferromagnetic (AFM) orthorhombic ( $Pnmm$ ) below the Néel temperature  $T_N$  (273-283K) [14-17], which was firstly reported by Corliss in 1960 [17]. Figure 1.2 presents the structures of CrN below and above the Néel temperature, respectively. In the left panel, the  $a$  and  $b$  axes of the orthorhombic lattice show a relationship with the cubic axes defining the (001) plane of the B1 lattice. In the  $z$ -direction, the  $c$  axis coincides with the lattice axis of the cubic B1 structure. The magnetic order consists of alternating double [110]-planes of spin up and spin down Cr moments. There is a small structural distortion from the underlying B1 lattice with the angle  $\alpha \approx 88.3^\circ$ , being slightly less than in the cubic case [17]. The transition from the cubic to the orthorhombic state

is a first-order phase transition, and results in a discontinuous volume reduction by  $\sim 0.59\%$  upon cooling.

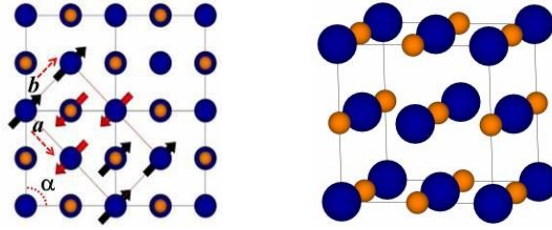


Figure 1.2: The unit cell of the antiferromagnetic orthorhombic CrN below the Néel temperature. The relationship of the orthorhombic unit cell axes to the cubic axes defining the (001) plane of the B1 lattice is shown (left panel). The paramagnetic cubic B1 structure of CrN at room temperature is shown in the right panel. Cr atoms and N atoms are represented with blue and orange color, respectively.

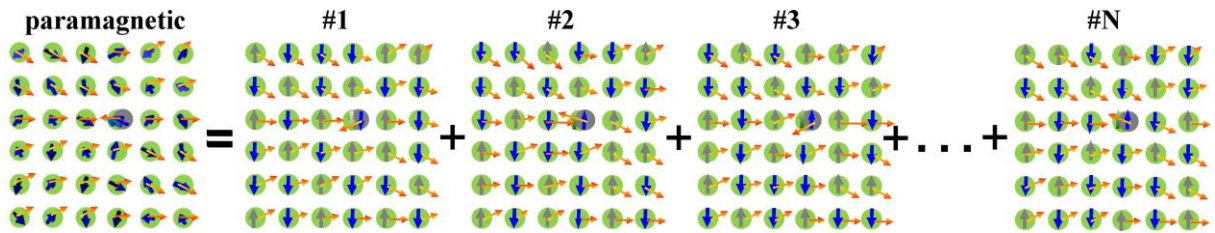


Figure 1.3: Sketch of a model representation of a paramagnetic state using disordered collinear magnetic moments (modified after [18]). The orange arrows denote the forces due to a small perturbation (gray atom) and the magnetic spins are denoted by gray or blue arrows.

Ferromagnetic and antiferromagnetic states describe situations with ordered collinear magnetic moments aligned in a parallel or antiparallel sense. In the paramagnetic state, the long-range order is lost resulting in a zero net magnetic moment, but large disordered local moments remain present. This makes it substantially different from a non-magnetic (NM) state which has also a zero net magnetic moment, but being a consequence of all local magnetic moments equal to zero. Figure 1.3 introduces a model [18] for the harmonic treatment of paramagnetic state (left hand side) represented as a series of special quasirandom structures (SQSs, right hand side) [19,20], where the local magnetic moments are collinear and randomly distributed over the lattice. This approach is known as spin-space averaging method (SSA) [18] and will be used in

evaluation of thermodynamics properties of CrN in Chapter 3.

The most interesting parts from the basic science standpoint are magnetic properties of CrN and its electronic structure [21,22]. The magnetic transition from antiferromagnetic to paramagnetic state at the Néel temperature is a process of disordering the ordered magnetic state [21-23]. The actual magnetic state greatly influences the electronic structure. Figure 1.4 shows the electronic density of states (DOS) of CrN with assumed different magnetic states calculated within the framework of GGA-PBE scheme.

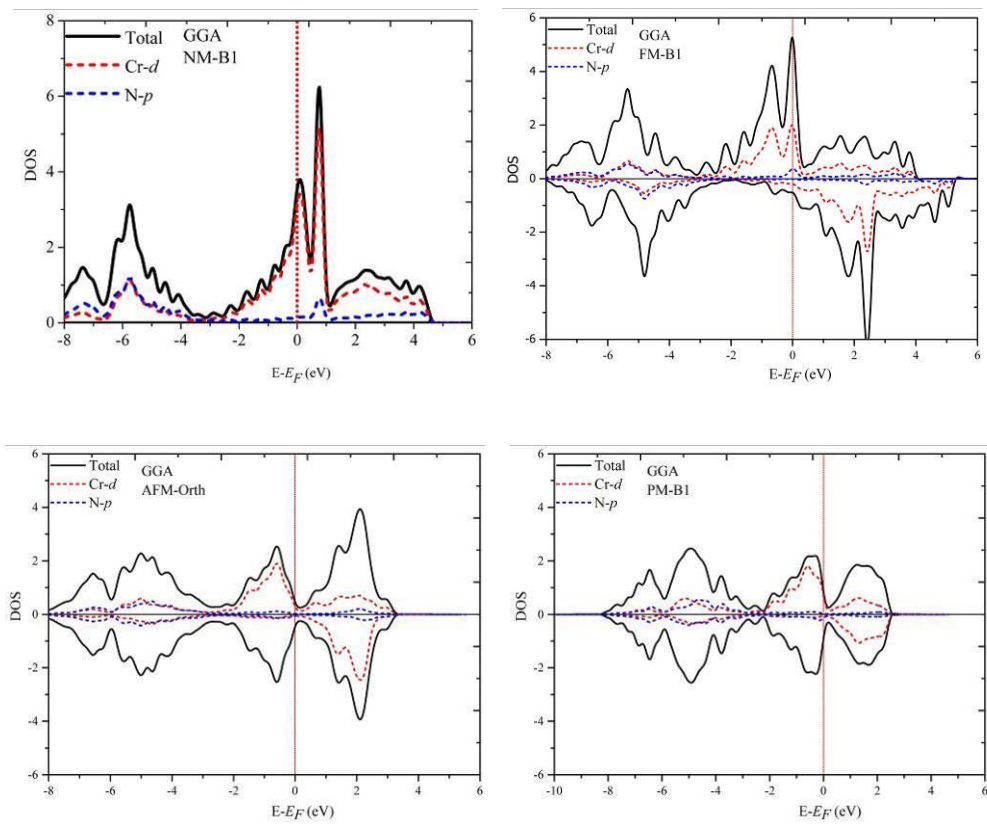


Figure 1.4: The electronic density of states of CrN for different magnetic configurations, including non-magnetic (NM), ferromagnetic (FM), antiferromagnetic (AFM), and paramagnetic (PM) states calculated within the GGA-PBE framework.

The electronic DOS of cubic B1 CrN with non-magnetic state has a very sharp peak directly at the Fermi level ( $E_F$ ), which is mostly contributed by the  $d$  electrons of Cr atoms. Concerning the electronic DOS of the ferromagnetic state, it is shifted to lower energies, but yielding a higher

DOS at  $E_F$  as compared with all other configurations. The high DOS at  $E_F$  is an indicator for a structural or magnetic instability, or anomalous phonon behavior, which will be discussed in Chapter 3 in more details. On the contrary, the electronic DOS of CrN with antiferromagnetic and paramagnetic configurations clearly show that there is a significant decrease of DOS at  $E_F$ , as the peak is shifted down below  $E_F$ .

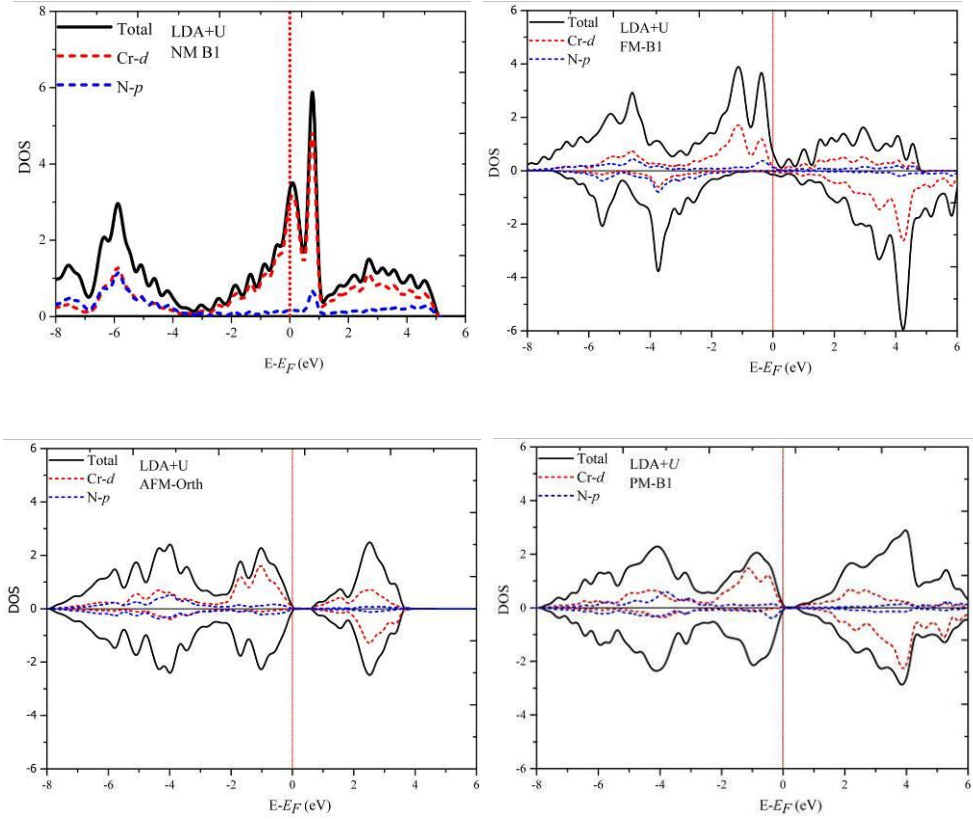


Figure 1.5: The electronic density of states of CrN with different magnetic states, including non-magnetic (NM), ferromagnetic (FM), antiferromagnetic (AFM), and paramagnetic (PM) configuration calculated using the LDA+U scheme.

Another often debated issue related to the electronic structure, is the electronic conduction of CrN, where both, the orthorhombic and the cubic B1 phases of CrN below and above the Néel temperature, respectively, have been experimentally determined to be both semiconducting and metallic, depending on specific conditions [16,24-27]. This non-consistency can be understood considering that the experimentally prepared CrN does not have always a perfect 1:1 ratio of metal/nonmetal atoms, that there are unavoidable defects in the experimental samples, and that

surface effects related to CrN thin films have non-negligible influence on the electronic conduction, too [26]. The electronic DOS presented in Fig. 1.4 clearly suggests that there is no band gap for any of the magnetic states. However, this metallic behavior mainly results from the neglected strong electronic correlation effects.

Figure 1.5 shows the electronic DOS with the strong correlations effects included employing the LDA+U framework. Compared with the results in Fig. 1.4, one prominent change introduced by the LDA+U scheme is that the high DOS at  $E_F$  decreases to zero, and finally a small band gap opens for antiferromagnetic and paramagnetic CrN. The electronic DOS of the CrN ferromagnetic state is shifted towards lower energies, nevertheless small DOS remains at  $E_F$ . Finally, the DOS of non-magnetic state from LDA+U scheme is almost the same as that of GGA-PBE.

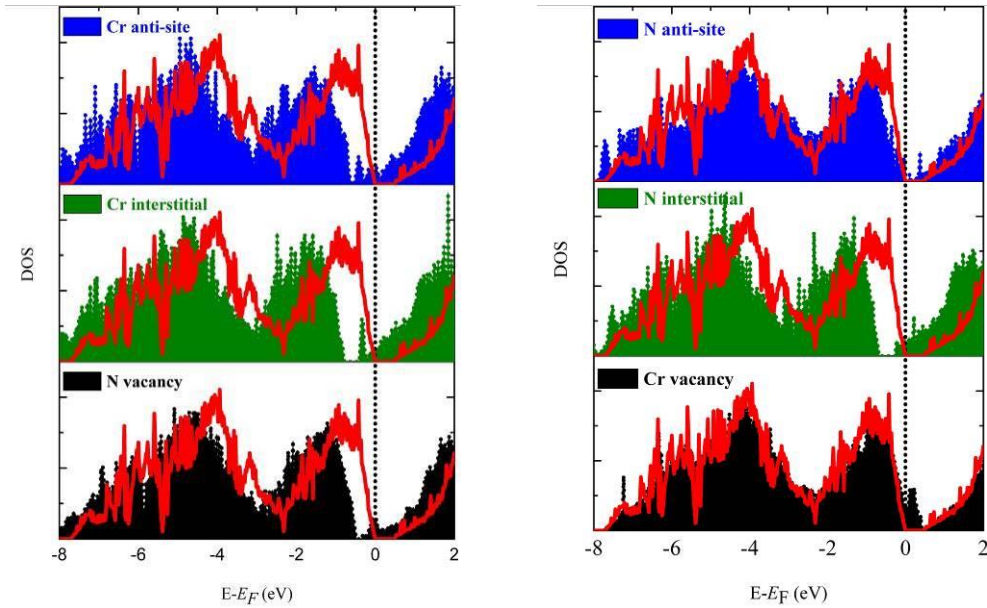


Figure 1.6: The electronic density of states of defected PM cubic B1 CrN with nitrogen understoichiometry (left panel) and overstoichiometry (right panel) calculated within the LDA+U framework. The electronic DOS of PM cubic B1 CrN without defects is shown with the red lines for the comparison.

A possible mechanism causing the metallic behavior of CrN, as indicated by a non-zero DOS at  $E_F$ , is demonstrated in Fig. 1.6. Defects can act as electron donors, finally increasing the band

---

filling, and hence closing the band gap. This topic has been recently investigated in detail by Mozafari *et al.* [28].

### 1.3 State-of-the-art coating design

Nowadays, the ever increasing demands for improved mechanical and thermal properties foster a development of novel hard coatings, which are mainly based on two approaches to overcome the limitations of individual TMN with respect to specific application-orientated requirements [1,29-31]. The most straightforward and successful strategy is the alloying concept which enables a creation of materials with enhanced properties. Group IIIB-VB TM-alloying is mainly achieved by a substitution of metal atoms at the metallic sublattice [32-38], while non-metal alloying of C, Si O, and B takes mainly place by incorporation of the non-metals on the N sublattice [39-42], which allows for a huge variety in size and bonding types, due to their different electronic configuration. For example, the substitution of Cr by Y in the CrAlN solid solutions results in the depletion of nonbonding states and increases the phase stability [37]. The oxygen incorporation into the non-metal sublattice of TiAlN induces the formation of metal vacancies for the charge balance and forms relatively weak Ti-O and Al-O bonds as compared to the corresponding metal nitride bonds [40]. Going beyond nitrides, the Si additions into amorphous alumina coatings significantly increase their thermal stability and retard the phase transformation of the as-deposited alumina thin films into their thermodynamically stable structure, due to the formation of shorter and stronger Si-O bonds as compared to Al-O bonds [39].

A systematical investigation of the IIIB-VB TM-alloying into TiAlN solid solutions reveals that Y weakens the bonding, Zr and Hf shows almost negligible effect on the electronic configurations [32,34,43,44]. On the other hand, Nb and Ta alloying shows a pronounced strengthening effect on the bonding, due to the enhanced  $sp^3d^2$  hybridization [34,43,45]. Alloying V, Nb, Ta, Mo, and W into TiAlN increases the ductility, which originates from the enhanced occupancy of  $d-t_{2g}$  metallic states induced by the valence electrons of substitutional elements [46-49]. In addition to the subtle electron configuration changes, the alloying induced

---

lattice strain due to the lattice mismatch plays an important role on the materials behavior. The different volume mismatch in, as well as the significantly different electronic structures of the cubic TiAlN and ScAlN are responsible for their different decomposition behavior [50,51].

Another alternative method to the alloying approach is the multilayer architectural coating design, which assembles the individual TMN phases in two- (multilayers) or three-dimensional (precipitates, nanocomposites) configurations, and makes significant improvements in terms of hardness, toughness, tribological properties, wear, corrosion, and oxidation resistance [52]. As compared with monolithic coatings, the chemical and physical properties of the multilayers are not only dependent on the properties of TMNs, but also highly related with the layer thickness, bilayer period and interfacial structures, which are adjustable in the state-of-the-art deposition techniques [53-55]. A comprehensive investigation on the CrN/AlN superlattices performed by Schlögl *et al.* [56-59] shows that the mechanical properties, thermal stability, and oxidation resistance are highly dependent on the bilayer period, thicknesses of individual nitride layer, as well as their structures. An interface-directed spinodal decomposition behavior was found in the TiAlN/CrN multilayered hard coatings, which shows drastic differences with the normal isotropic spinodal decomposition in the monolithic TiAlN coatings [60]. Interfaces in general, and fully or semi-coherent ones in particular, in multilayer structures act as obstacles for crack propagation and hence contribute to the enhanced fracture toughness by different interfacial-related mechanisms, e.g. crack deflection and splitting.

### **1.3.1 CrAlN**

Conventional binary hard coatings such as TiN and CrN are often used to enhance the performance of cutting tools [1,4]. However, their oxidation resistance is limited to approximately 550 °C and 700 °C, respectively [13]. To improve the oxidation resistance of these films, Al is alloyed into TiN and CrN to form quasi-binary TiAlN and CrAlN, which are now widely used in commercial applications [2,61-63]. The incorporation of Al into TiN lattice forms a supersaturated solid solution, and improves the cutting performance of the coatings. This has been attributed to the increase in oxidation resistance of the Al containing coating as

well as to the age hardening mechanism, arising from a spinodal decomposition of cubic B1 structure TiAlN into Al- and Ti-enriched coherent cubic domains [2,64], as shown in Fig. 1.7. It is clear that there is a significant enhancement of hardness for TiAlN as compared with TiN. However, the same spinodal mechanism leading to age hardening, is also the first step in a process fostering a nucleation of hexagonal AlN, which is detrimental for cutting performance. The mechanical properties and performance of supersaturated  $Ti_{1-x}Al_xN$  solid solution improves with Al content. However, at  $x=0.7$ , a wurtzite structure becomes preferred to the cubic one even in the supersaturated solid solution state, which again results in deteriorated mechanical properties. Additionally, the TiAlN hard coatings exhibit relatively high friction coefficients.

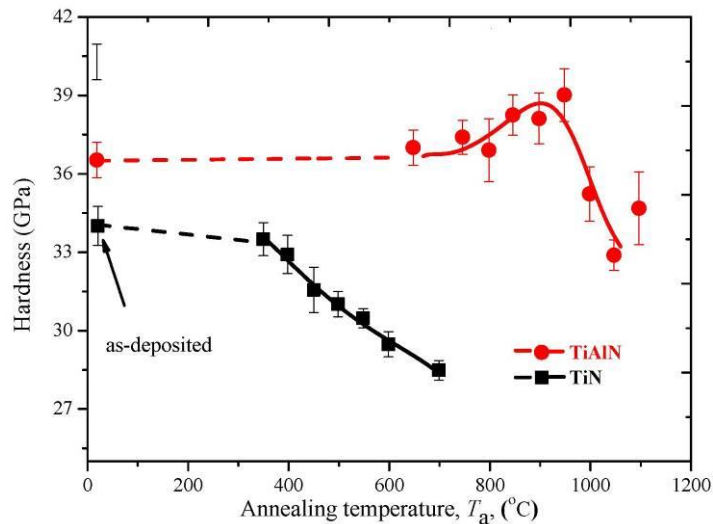


Figure 1.7: The hardness of Ti(Al)N as a function of annealing temperature,  $T_a$  [2].

Low friction and high temperature oxidation resistance are required in addition to excellent mechanical properties, especially in high speed and dry cutting applications. Here, CrAlN coatings excel over the TiAlN as they exhibit better tribological properties [65]. Recently, great attention has been paid to the Al-rich CrAlN coatings. Mayrhofer *et al.* [61,62,66] found that the annealed hexagonal CrAlN coatings exhibit beneficial nanoscale-sized domains with CrN precipitates encapsulated in an Al-rich matrix, which makes the coatings more stable at higher temperatures. When comparing CrAlN with TiAlN, the Cr-containing system shows slightly lower hardness for the same Al content. However, a slightly larger amount of Al can be solved

in the B1 phase without the formation of hexagonal AlN, and the stability of CrAlN coatings can be preserved up to higher temperatures, as both the chromium and aluminum could form protective oxides which suppressed oxygen diffusion [67]. The theoretically calculated mixing enthalpy of cubic  $\text{Cr}_{1-x}\text{Al}_x\text{N}$  shows, that it is more stable against decomposition than cubic  $\text{Ti}_{1-x}\text{Al}_x\text{N}$  [51,68]. The experimentally obtained maximum Al content in the cubic  $\text{Cr}_{1-x}\text{Al}_x\text{N}$  is around 0.75 [69]; The theoretically predicted maximum solubility of AlN in cubic  $\text{Cr}_{1-x}\text{Al}_x\text{N}$  varies from 0.48 to 0.95, depending on different structural configurations, external condition such as pressure, or used methods [69-73]. Fig. 1.8 shows the structural evolution of  $\text{Cr}_{1-x}\text{Al}_x\text{N}$  as a function of the AlN content.

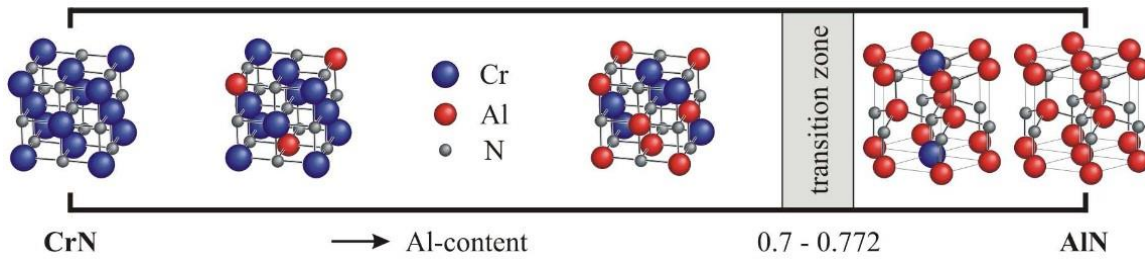


Figure 1.8: Structural development of  $\text{Cr}_{1-x}\text{Al}_x\text{N}$ . The grey area denotes the transition zone from cubic B1  $\text{Cr}_{1-x}\text{Al}_x\text{N}$  to AlN-based wurtzite B4  $\text{Cr}_{1-x}\text{Al}_x\text{N}$  [69-71].

### 1.3.2 Alloying CrN with transitional metal

In order to further tune the structural, mechanical, and tribological properties, i.e., incorporation of other elements into the CrN-based coatings, alloying has proven to be an effective concept. Recently, various  $\text{Cr}_{1-x}\text{X}_x\text{N}$  ( $\text{X}=\text{Al}, \text{Ti}, \text{Ta}, \text{Zr}, \text{Mo}, \text{W}$  and  $\text{V}$ ) ternary coatings have received lots of attention both experimentally [61,65,74-81] as well as theoretically [38,51,69,82], due to their excellent properties. One of the most successful examples is the addition of Al to improve mechanical properties as well as oxidation resistance of CrN, as discussed in the previous Section. It has been reported that additions of V, Mo or W into CrN improve its tribological properties and toughness [74,75,81], while the thermal stability and magnetic properties of CrN can be adjusted by alloying it with TiN [79,82], hence forming a  $\text{Cr}_{1-x}\text{Ti}_x\text{N}$  solid solution. CrTiN is of interest for its corrosion protection in e.g. fuel cell application. The most intriguing aspect

---

of CrTiN is related to its surprising magnetic behavior [82].  $\text{Cr}_x\text{Ti}_{1-x}\text{N}$  shows ferromagnetic ordering at the Curie temperature with a value of 140K and 305K at about  $x=0.50$  and disappears abruptly at  $x>0.50$ .  $\text{Cr}_{1-x}\text{Ta}_x\text{N}$  has enhanced simultaneously mechanical and oxidation properties with respect to CrN [83]. No experimental data are presently available for  $\text{Cr}_{1-x}\text{TM}_x\text{N}$  (TM=Sc, Y and Hf), and only a few studies on CrNbN exist in the literature (e.g., [84]).

Alloying molybdenum (Mo) or tungsten (W) into CrN coatings has been confirmed to be effective for improving tribological properties and toughness [74,75,81]. The ability of Mo and W to form Magn  $\delta$ -phase oxides can be used to prepare materials with solid lubricant potential, which significantly reduce the coefficient of friction for example. Recently, Quintela *et al.* [85] pointed out that even very small additions of only  $\sim 1$  at.% of Mo or W to CrN, lead to a spontaneous phase segregation into Mo- and W-rich regions. Contrary, Kwang *et al.* [86] stated that cubic Cr-Mo-N coatings with Mo content less than 30.4 at.% are a substitutional solid solution of (Cr, Mo)N. Other reports state that deposited cubic Cr-Mo-N and Cr-W-N coatings undergo decomposition into cubic B1-CrN and  $\gamma$ -Mo<sub>2</sub>N or  $\gamma$ -W<sub>2</sub>N [74].

However, before clarifying this exciting controversy, it is useful to review also other nitride systems. In general, the alloying solid solutions are always strongly related with their constituents. It is convenient for treating  $\text{Cr}_{1-x}\text{TM}_x\text{N}$  systems to view them as quasi-binary systems of the binary CrN and TMN compounds. In addition to CrN, other binary systems discussed in the present thesis are AlN; ScN and YN (group IIIB); TiN, ZrN, and HfN (group IVB); VN, NbN, and TaN (group VB); and MoN and WN (group VIB). Out of these binary nitride systems, the cubic B1 structure is a metastable configuration for AlN, NbN, and TaN, while MoN and WN are unstable in this cubic structure, as indicated by the negative elastic constant  $C_{44}$  [87,88]. As stated before, the stable phases in Mo-N and W-N systems are  $\gamma$ -Mo<sub>2</sub>N or  $\gamma$ -W<sub>2</sub>N. Consequently, it is not precise to use the conventional chemical formula  $\text{Cr}_{1-x}\text{TM}_x\text{N}$  for the cubic Cr-Mo-N and Cr-W-N solid solutions, and instead a more informative chemical formula  $\text{Cr}_{1-x}\text{TM}_x\text{N}_{1-0.5x}$  should be applied to describe these system. This will be discussed in detail in Chapter 7.

The controversy is mainly due to the similarity of crystallographic structures of cubic B1-CrN and  $\gamma$ -TM<sub>2</sub>N, which makes their XRD peaks very close and finally difficult to distinguish whether the coating is a mixture of B1-CrN+ $\gamma$ -TM<sub>2</sub>N or a cubic (Cr, TM)N solid solution, with TM being Mo or W [74]. Although the binary nitrides cubic B1-MoN and B1-WN are mechanically unstable, they are used as the boundary systems for cubic B1-(Cr, TM)N with nitrogen contents of constantly 50 at.%, as always reported [76,78,86]. By adjusting the N<sub>2</sub> gas partial pressure during the sputtering deposition process, the atomic ratio N/metal can be even above 1 for cubic (Cr, Mo)N or (Cr, W)N thin films [76,89]. While employing a pair distribution function analysis of nearest neighbor distances between atoms, Shen *et al.* [90], stated that the excessive nitrogen atoms in overstoichiometric WN<sub>x</sub> thin films were present in the grain boundaries of  $\gamma$ -W<sub>2</sub>N, not at the vacant octahedral sites. Details on these issues are presented in Chapter. 7.

### 1.3.3 Quaternary Cr-Al-TM-N

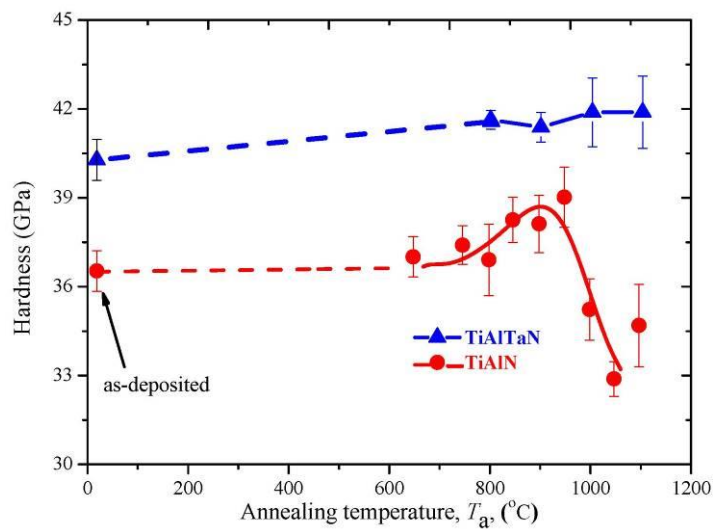


Figure 1.9: The hardness of TiAl(TM)N as a function of annealing temperature,  $T_a$  [36].

The influence of alloying transition metal elements in the coating has been extensively studied for the TiAlN system [32,34-36,44,45,91], and the alloying of TiAlN with additional elements is regarded as a promising approach to improve, e.g., wear properties, oxidation resistance, and hardness of TiAlN coatings. Figure 1.9 gives a vivid example of the alloying effect on hardness:

---

Ta alloying into TiAlN increases its hardness as well as the thermal stability.

To further improve the wear resistance, high temperature oxidation resistance and also the mechanical properties of the CrAlN coatings, alloying of additional group IIIB-VB transition metal (TM) elements (TM: Sc, Y; Ti, Zr, Hf; V, Nb, and Ta) into CrAlN coatings becomes an important concept in the industrial area as well as an interesting and exciting topic of basic research. The most important features of the new generation of hard protective coatings are their low friction, high oxidation resistance at high temperatures, and increased thermal stability. In 2005, using six high aluminum AlCr targets each containing 5 at. % of Ti, V, Y, Nb, Mo, and W respectively, Endrino *et al.* [92] investigated the alloying effect on the CrAlN coatings for the first time, and revealed a notable influence of the alloying elements on the mechanical and oxidation resistance behavior of the high aluminum chromium nitride coatings.

Investigations of yttrium have already shown the big potential to effectively enhance the thermal stability, to reduce friction of CrAlN at elevated temperatures, and to improve high temperature oxidation resistance [37,93-95]. The latter is attributed to Y retarding diffusional processes, such as recovery, precipitation of hcp-AlN and fcc-YN, grain growth, and decomposition induced N<sub>2</sub> release [93]. On the other hand, an excessive Y-incorporation was found to be detrimental to the oxidation resistance, as fast growing porous oxide scales were formed. Scheerer *et al.* [96] found that increasing the yttrium content of the (Cr,Al,Y)N leads to a more amorphous microstructure and a finer and denser morphology with a smoother surface, and finally resulted in advantages in the wear behavior as well as in the oxidation resistance. Hovsepian *et al.* [97,98] found that CrAlYN/CrN nanoscale multilayer coatings reduced the friction coefficient from the room temperature to high temperatures, which demonstrated the promising high temperature tribological behavior of the system.

The addition of vanadium to CrAlN coating offers lubricious effects at elevated temperatures due to the formation and melting of the Magnés phase oxide V<sub>2</sub>O<sub>5</sub> forming a low-friction layer on the surface, similar to CrVN as discussed earlier. Franz *et al.* [99-101] found that alloying V into the CrAlN coatings triggered a separation into face-centered cubic and hexagonal

---

wurtzite-type phases, and the hexagonal phase fraction was observed to increase with the V concentration in the coating. The single-phase fcc-CrAlVN coating appeared to be more oxidation resistant leading to an increase in friction when compared with the dual-phase coatings. Endrino *et al.* [92] found that CrAlWN coatings showed lower oxidation stability than CrAlN, which is a consequence of the W affinity to oxidation. Similar to alloying W into CrAlN coatings, Yoon *et al.* [102] showed that alloying Mo into CrAlN leads to a lower oxidation temperature than that of CrAlN coatings due to the lower oxidation temperature of MoN.

Recently, Rojas *et al.* [103] found that alloying Zr into CrAlN coating resulted in the oxidation progressing to a greater extent. Kim *et al.* [118] stated that the hardness of the CrAlZrN films varied as a function of the N<sub>2</sub> partial pressure with the maximum value being approximately 45 GPa. Li *et al.* [104] deposited low Zr (ZrN: ~10%) and high Zr (ZrN: ~50%) quaternary CrAlZrN coatings with increasing Al content by DC reactive magnetron sputtering and found that all those coatings exhibited an fcc B1 structure. The highest hardness and strongest adhesion values were achieved in coatings with lower Zr and Al content. Endrino *et al.* [92] found that the CrAlNbN (CrN: 32%, AlN: 63%, NbN: 7%) coating with the (200) texture performed significantly better than the CrAlN coating with the (111) texture. No experimental or theoretical studies have been reported so far for the alloying of Sc, Hf, or Ta into CrAlN coatings.

## **1.4 Computational Materials Science**

The most recent successful method in materials science is to employ *ab initio* calculations to treat interactions at the electronic level, and hence to provide a deeper understanding for experimental findings [105,106]. Additionally, the calculations shall guide the experiment by predicting chemistry-related trends, and hence assist and boost the design of novel materials [34,91,107,108].

### **1.4.1 Recent theoretical work**

An extensive *ab initio* work on transition metal nitrides in general, and on CrN-related

---

materials in particular, providing insight and theoretical guidance for experiments has been performed in the past years. The theoretical work related with CrN-based coating systems can be classified into two main groups. The first class, coming from the physics community, is driven by the development of methodologies to deal with disorder at elevated temperatures, including the magnetic and the chemical disorder [109,110]. The second group originates from materials science. It uses readily available modeling techniques and employs them to explore specific systems [33,51,68,108,111,112].

The early works ignored the magnetic nature of CrN and simply treated it as non-magnetic material (i.e. fulfilling the condition of the macroscopic magnetic moment to be 0) [14]; however, this has been shown to lead to a significant overestimation of its bulk modulus and an underestimation of the lattice parameters. Therefore, the most recent works considered explicitly the non-zero local magnetic moments [113,114]. Nevertheless, the paramagnetic phase is challenging for description within the periodic crystalline model conveniently adopted by first principles calculations. Several methods mainly based on the disordered local moments (DLM) model [115] have been proposed over the years, including coherent potential approximation (CPA) [116], SQS method [19,20], the magnetic sampling method (MSM) [113], and molecular dynamics (MD). The details of these methodologies are discussed in Chapter 2. In the present thesis, we adopt a supercell-based approach with spins up and down being distributed on the Cr atoms according to SQS scheme, which provides a mathematically rigorous recipe for generating supercells with as random as possible arrangement of atoms (or spins in this particular case). The same scheme is also used to deal with the chemical disorder in the solid solution systems.

Regarding theoretical investigations, CrN has received great attention mainly due to its electronic and magnetic properties, while only a few papers have been devoted to its phase stability. Recent works of Alling *et al.* [113], Shulumba *et al.* [109,110], and Zhou *et al.* (Ref. [117], Chapter 3) discuss the thermodynamics of paramagnetic CrN, including the magneto-structural transition and estimation of the Néel temperature (see also Chapter 3). Mozafari *et al.* [28] extended the finite-temperature treatment also to point defect stability in

---

CrN. In the case of CrAlN, the theoretical work mainly focuses on the maximum solubility of AlN in the cubic B1  $\text{Cr}_{1-x}\text{Al}_x\text{N}$  and the relative phase stability. Mayrhofer *et al.* [69] used relatively small and ordered supercells to study the maximum solubility of Al in the cubic CrAlN, showing also the large impact of the ordering of metal atoms. This prediction has been amended by Holec *et al.* [73] showing that hydrostatic pressure leads to a significant enhancement of the Al solubility in cubic phase. The electronic structure of CrAlN has been studied in detail by Alling *et al.* [51,68,111]. Bulk and Young's modulus of CrAlN have been predicted by Mayrhofer *et al.* [69] showing that there is only a very moderate compositional dependence. Zhou *et al.* (Ref. [112], Chapter 5) performed explicit calculations of single crystal elastic constants as functions of the composition.

Reports on other CrTMN systems is very limited. A recent review on the ferromagnetic CrTiN by Alling *et al.* [82], summarizes a thorough theoretical investigation of the magnetism in CrTiN substitutionally disordered solid solutions. Zhou *et al.* (Ref. [108], Chapter 6) discussed the alloying effect of transition metals on structure, stability and ductility of CrN.

There exists only a very limited number of studies treating the quaternary systems, e.g., CrAlYN, and CrAlTiN. Based on first-principles calculations and experimental results, Rovere *et al.* [37] found that the Y incorporation shifted the critical Al content to lower values and the substitution of Cr by Y increased the phase stability due to the depletion of non-bonding (anti-bonding) states, while the substitution of Al by Y decreased the phase stability mainly due to lattice strain. Based on Density Functional Theory calculations and using energy dispersive X-ray spectroscopy, transmission electron microscopy and differential scanning calorimetry measurements, Lind *et al.* [91] further predicted and experimentally demonstrated that CrAlTiN alloys decompose spinodally into CrTiN-rich and CrAlN-rich nanometer sized regions. The spinodal decomposition resulted in age hardening, and the presence of Cr within the AlN phase delayed the formation of the detrimental wurtzite phase, leading to a substantial improvement of thermal stability as compared with TiAlN or CrAlN.

---

## **1.4.2 The aim of present thesis**

The aim of the present work is to use state-of-the-art computational materials science techniques to offer a deeper understanding of the materials behavior and related properties, and provide predictions to guide and assist experiments. The outline of the present work can be divided into two parts. The first part provides deeper knowledge on the materials behavior, including the phase stability of CrN, and the effect of defects on the electronic structures, phase stability, structural, and mechanical properties of CrN-based coatings (Chapters 3, 4, and 7). In the second part, the available modeling techniques are used to predict a comprehensive overview of chemical trends of CrN-based solid solutions, and hence to provide tools for knowledge-based computer-assisted design of novel coating materials. This includes calculation of phase stability, structural and mechanical properties of ternary and quaternary systems (Chapters 5, 6, and 8).

---

## References

- [1] P. H. Mayrhofer, C. Mitterer, L. Hultman, and H. Clemens, *Prog. Mater. Sci.* **51**, 1032 (2006).
- [2] P. H. Mayrhofer, A. Hörling, L. Karlsson, J. Sjö lén, T. Larsson, C. Mitterer, and L. Hultman, *Appl. Phys. Lett.* **83**, 2049 (2003).
- [3] P. H. Mayrhofer, C. Mitterer, and H. Clemens, *Adv. Eng. Mater.* **7**, 1071 (2005).
- [4] P. H. Mayrhofer, R. Rachbauer, D. Holec, F. Rovere, and J. M. Schneider, in *Comprehensive Materials Processing* (2014), pp. 355.
- [5] J. H äglund, G. Grimvall, T. Jarlborg, and A. F. Guillermet, *Phys. Rev. B* **43**, 14400 (1991).
- [6] J. H äglund, A. Fernndez Guillermet, G. Grimvall, and M. Körling, *Phys. Rev. B* **48**, 11685 (1993).
- [7] H. Holleck, *Surf. Coat. Technol.* **43-44**, 245 (1990).
- [8] C. Mitterer, P. H. Mayrhofer, and J. Musil, *User Modeling and User-Adapted Interaction* **71**, 279 (2003).
- [9] T. Cselle and A. Barimani, *Surf. Coat. Technol.* **76**, 712 (1995).
- [10] L. Hultman, *Vacuum* **57**, 1 (2000).
- [11] G. Berg, C. Friedrich, E. Broszeit, and C. Berger, *Surf. Coat. Technol.* **86-87**, 184 (1996).
- [12] B. Navinšek, P. Panjan, and I. Milošev, *Surf. Coat. Technol.* **97**, 182 (1997).
- [13] P. H. Mayrhofer, H. Willmann, and C. Mitterer, *Surf. Coat. Technol.* **146-147**, 222 (2001).
- [14] F. Rivadulla *et al.*, *Nat. Mater.* **8**, 947 (2009).
- [15] S. Wang *et al.*, *Phys. Rev. B* **86**, 064111 (2012).
- [16] X. Y. Zhang, J. S. Chawla, R. P. Deng, and D. Gall, *Phys. Rev. B* **84**, 073101 (2011).
- [17] L. M. Corliss, N. Elliott, and J. M. Hastings, *Phys. Rev.* **117**, 929 (1960).
- [18] F. Körmann, A. Dick, B. Grabowski, T. Hickel, and J. Neugebauer, *Phys. Rev. B* **85**, 125104 (2012).
- [19] S. H. Wei, L. G. Ferreira, J. E. Bernard, and A. Zunger, *Phys. Rev. B* **42**, 9622 (1990).
- [20] A. Zunger, S. H. Wei, L. G. Ferreira, and J. E. Bernard, *Phys. Rev. Lett.* **65**, 353 (1990).
- [21] A. S. Botana, F. Tran, V. Pardo, D. Baldomir, and P. Blaha, *Phys. Rev. B* **85**, 235118

---

(2012).

- [22] A. Filippetti, W. E. Pickett, and B. M. Klein, *Phys. Rev. B* **59**, 7043 (1999).
- [23] A. Filippetti and N. A. Hill, *Phys. Rev. Lett.* **85**, 5166 (2000).
- [24] A. Herwadkar and W. R. L. Lambrecht, *Phys. Rev. B* **79**, 035125 (2009).
- [25] X. Y. Zhang and D. Gall, *Phys. Rev. B* **82**, 045116 (2010).
- [26] A. S. Botana, V. Pardo, D. Baldomir, and P. Blaha, *Phys. Rev. B* **87**, 075114 (2013).
- [27] D. Gall, C. S. Shin, R. T. Haasch, I. Petrov, and J. E. Greene, *J. Appl. Phys.* **91**, 5882 (2002).
- [28] E. Mozafari, B. Alling, P. Steneteg, and I. A. Abrikosov, *Phys. Rev. B* **91**, 094101 (2015).
- [29] S. Vepřek, *J. Vac. Sci. Technol., A* **17**, 2401 (1999).
- [30] P. H. Mayrhofer, C. Mitterer, and J. Musil, *Surf. Coat. Technol.* **174-175**, 725 (2003).
- [31] J. Paulitsch, C. Maringer, and P. H. Mayrhofer, *Tribol. Lett.* **46**, 87 (2012).
- [32] L. Chen, D. Holec, Y. Du, and P. H. Mayrhofer, *Thin Solid Films* **519**, 5503 (2011).
- [33] D. Holec, R. Rachbauer, L. Chen, L. Wang, D. Luef, and P. H. Mayrhofer, *Surf. Coat. Technol.* **206**, 1698 (2011).
- [34] D. Holec, L. Zhou, R. Rachbauer, and P. H. Mayrhofer, *J. Appl. Phys.* **113** 365301 (2013).
- [35] P. H. Mayrhofer, R. Rachbauer, and D. Holec, *Scripta Mater.* **63**, 807 (2010).
- [36] R. Rachbauer, D. Holec, and P. H. Mayrhofer, *Surf. Coat. Technol.* **211**, 98 (2012).
- [37] F. Rovere, D. Music, J. M. Schneider, and P. H. Mayrhofer, *Acta Mater.* **58**, 2708 (2010).
- [38] F. Rovere, D. Music, S. Ershov, M. T. Baben, H. G. Fuss, P. H. Mayrhofer, and J. M. Schneider, *J. Phys. D: Appl. Phys.* **43** 035302 (2010).
- [39] H. Bolvardi *et al.*, *J. Appl. Phys.* **117** 025302 (2015).
- [40] M. Hans, M. To Baben, D. Music, J. Ebenhöch, D. Primetzhofer, D. Kurapov, M. Arndt, H. Rudigier, and J. M. Schneider, *J. Appl. Phys.* **116**, 093515 (2014).
- [41] L. Shang, D. Music, M. T. Baben, and J. M. Schneider, *J. Phys. D: Appl. Phys.* **47** 065308 (2014).
- [42] K. Kutschej, N. Fateh, P. H. Mayrhofer, M. Kathrein, P. Polcik, and C. Mitterer, *Surf. Coat. Technol.* **200**, 113 (2005).

- 
- [43] R. Rachbauer, D. Holec, M. Lattemann, L. Hultman, and P. H. Mayrhofer, *Int. J. Mater. Res* **102**, 735 (2011).
- [44] R. Rachbauer, A. Blutmager, D. Holec, and P. H. Mayrhofer, *Surf. Coat. Technol.* **206**, 2667 (2012).
- [45] R. Rachbauer, D. Holec, and P. H. Mayrhofer, *Appl. Phys. Lett.* **97** 151901 (2010).
- [46] D. G. Sangiovanni, L. Hultman, and V. Chirita, *Acta Mater.* **59**, 2121 (2011).
- [47] D. G. Sangiovanni, V. Chirita, and L. Hultman, *Thin Solid Films* **520**, 4080 (2012).
- [48] D. G. Sangiovanni, V. Chirita, and L. Hultman, *Phys. Rev. B* **81**, 104107 (2010).
- [49] H. Kindlund *et al.*, *APL Materials* **1**, 042104 (2013).
- [50] C. Höglund, B. Alling, J. Birch, M. Beckers, P. O. Å. Persson, C. Baetz, Z. Czigány, J. Jensen, and L. Hultman, *Phys. Rev. B* **81** 224101 (2010).
- [51] B. Alling, A. Karimi, and I. A. Abrikosov, *Surf. Coat. Technol.* **203**, 883 (2008).
- [52] P. E. Hovsepian, D. B. Lewis, and W. D. Münz, *Surf. Coat. Technol.* **133-134**, 166 (2000).
- [53] V. Chawla, D. Holec, and P. H. Mayrhofer, *Thin Solid Films* **565**, 94 (2014).
- [54] V. Chawla, D. Holec, and P. H. Mayrhofer, *J. Phys. D: Appl. Phys.* **46** 045305 (2013).
- [55] V. Chawla, D. Holec, and P. H. Mayrhofer, *Comput. Mater. Sci.* **55**, 211 (2012).
- [56] M. Schlögl, J. Paulitsch, and P. H. Mayrhofer, *Surf. Coat. Technol.* **240**, 250 (2014).
- [57] M. Schlögl, J. Paulitsch, J. Keckes, and P. H. Mayrhofer, *Thin Solid Films* **531**, 113 (2013).
- [58] M. Schlögl, B. Mayer, J. Paulitsch, and P. H. Mayrhofer, *Thin Solid Films* **545**, 375 (2013).
- [59] M. Schlögl, C. Kirchlechner, J. Paulitsch, J. Keckes, and P. H. Mayrhofer, *Scripta Mater.* **68**, 917 (2013).
- [60] I. Povstugar, P.-P. Choi, D. Tytko, J.-P. Ahn, and D. Raabe, *Acta Mater.* **61**, 7534 (2013).
- [61] P. H. Mayrhofer, H. Willmann, and A. E. Reiter, *Surf. Coat. Technol.* **202**, 4935 (2008).
- [62] H. Willmann, P. H. Mayrhofer, P. O. Å. Persson, A. E. Reiter, L. Hultman, and C. Mitterer, *Scripta Mater.* **54**, 1847 (2006).
- [63] L. Chen, J. Paulitsch, Y. Du, and P. H. Mayrhofer, *Surf. Coat. Technol.* **206**, 2954 (2012).

- 
- [64] P. H. Mayrhofer, L. Hultman, J. M. Schneiden, P. Staron, and H. Clemens, *Int. J. Mater. Res* **98**, 1054 (2007).
- [65] M. Uchida, N. Nihira, A. Mitsuo, K. Toyoda, K. Kubota, and T. Aizawa, *Surf. Coat. Technol.* **177-178**, 627 (2004).
- [66] H. Willmann, P. H. Mayrhofer, L. Hultman, and C. Mitterer, *J. Mater. Res.* **23**, 2880 (2008).
- [67] M. Kawate, A. K. Hashimoto, and T. Suzuki, *Surf. Coat. Technol.* **165**, 163 (2003).
- [68] B. Alling, T. Marten, I. A. Abrikosov, and A. Karimi, *J. Appl. Phys.* **102** 044314 (2007).
- [69] P. H. Mayrhofer, D. Music, T. Reeswinkel, H. G. Fuß, and J. M. Schneider, *Acta Mater.* **56**, 2469 (2008).
- [70] Y. Makino, *ISIJ International* **38**, 925 (1998).
- [71] P. Spencer, *Zeitschrift fuer Metallkunde/Materials Research and Advanced Techniques* **92**, 1145 (2001).
- [72] R. F. Zhang and S. Veprek, *Acta Mater.* **55**, 4615 (2007).
- [73] D. Holec, F. Rovere, P. H. Mayrhofer, and P. B. Barna, *Scripta Mater.* **62**, 349 (2010).
- [74] B. Gu, J. P. Tu, X. H. Zheng, Y. Z. Yang, and S. M. Peng, *Surf. Coat. Technol.* **202**, 2189 (2008).
- [75] P. Hones, R. Consiglio, N. Randall, and F. Leacutevy, *Surf. Coat. Technol.* **125**, 179 (2000).
- [76] P. Hones, M. Diserens, R. Sanjin és, and F. L évy, *J. Vac. Sci. Technol., B* **18**, 2851 (2000).
- [77] P. Hones, R. Sanjin és, and F. L évy, *Thin Solid Films* **332**, 240 (1998).
- [78] P. Hones, R. Sanjin és, F. L évy, and O. Shojaei, *J. Vac. Sci. Technol., A* **17**, 1024 (1999).
- [79] X. Jin, L. Gao, and J. Sun, *Acta Mater.* **54**, 4035 (2006).
- [80] G. Kim, B. Kim, S. Lee, and J. Hahn, *Surf. Coat. Technol.* **200**, 1669 (2005).
- [81] B. S. Yau, C. W. Chu, D. Lin, W. Lee, J. G. Duh, and C. H. Lin, *Thin Solid Films* **516**, 1877 (2008).
- [82] B. Alling, *Phys. Rev. B* **82** 054408 (2010).
- [83] Y.-I. Chen, K.-Y. Lin, and C.-C. Chou, *Thin Solid Films* **544**, 606 (2013).

- 
- [84] J. N. Tan and J. H. Hsieh, *Surf. Coat. Technol.* **167**, 154 (2003).
- [85] C. X. Quintela, B. Rodríguez-González, and F. Rivadulla, *Appl. Phys. Lett.* **104** 022103 (2014).
- [86] K. Ho Kim, E. Young Choi, S. Gyun Hong, B. Gyu Park, J. Hong Yoon, and J. Hae Yong, *Surf. Coat. Technol.* **201**, 4068 (2006).
- [87] M. B. Kanoun, S. Goumri-Said, and M. Jaouen, *Phys. Rev. B* **76**, 134109 (2007).
- [88] G. L. W. Hart and B. M. Klein, *Phys. Rev. B* **61**, 3151 (2000).
- [89] P. Hones, N. Martin, M. Regula, and F. Lévy, *J. Phys. D: Appl. Phys.* **36**, 1023 (2003).
- [90] Y. G. Shen and Y. W. Mai, *Mater. Sci. Eng., A* **288**, 47 (2000).
- [91] H. Lind, R. Forsén, B. Alling, N. Ghafoor, F. Tasndi, M. P. Johansson, I. A. Abrikosov, and M. Odén, *Appl. Phys. Lett.* **99** 091903 (2011).
- [92] J. L. Endrino and V. Derflinger, *Surf. Coat. Technol.* **200**, 988 (2005).
- [93] T. Dudziak, P. K. Datta, P. H. Mayrhofer, and F. Rovere, *Oxid. Met.* **75**, 359 (2011).
- [94] F. Rovere and P. H. Mayrhofer, *J. Vac. Sci. Technol., A* **25**, 1336 (2007).
- [95] F. Rovere, P. H. Mayrhofer, A. Reinholdt, J. Mayer, and J. M. Schneider, *Surf. Coat. Technol.* **202**, 5870 (2008).
- [96] H. Scheerer and C. Berger, *Plasma. Process. Polym.* **6**, S157 (2009).
- [97] P. E. Hovsepian, A. P. Ehiasarian, R. Braun, J. Walker, and H. Du, *Surf. Coat. Technol.* **204**, 2702 (2010).
- [98] P. E. Hovsepian, A. P. Ehiasarian, and U. Ratayski, *Surf. Coat. Technol.* **203**, 1237 (2009).
- [99] R. Franz, J. Neidhardt, R. Kaindl, B. Sartory, R. Tessadri, M. Lechthaler, P. Polcik, and C. Mitterer, *Surf. Coat. Technol.* **203**, 1101 (2009).
- [100] R. Franz *et al.*, *J. Vac. Sci. Technol. A* **26**, 302 (2008).
- [101] R. Franz, J. Neidhardt, B. Sartory, R. Kaindl, R. Tessadri, P. Polcik, V. H. Derflinger, and C. Mitterer, *Tribol. Lett.* **23**, 101 (2006).
- [102] C. S. Yoon, K. H. Kim, S. H. Kwon, and I. W. Park, *J. Korean Phys. Soc.* **54**, 1237 (2009).
- [103] T. C. Rojas, S. El Mrabet, S. Domínguez-Meister, M. Brizuela, A. García-Luis, and J. C. Sánchez-López, *Surf. Coat. Technol.* **211**, 104-110 (2011).

- 
- [104] W. Z. Li, M. Evaristo, and A. Cavaleiro, *Surf. Coat. Technol.*, 239–245 (2013).
- [105] M. Friák *et al.*, *Steel. Res. Int* **82**, 86 (2011).
- [106] M. Friák *et al.*, *EPJ Plus* **126**, 1 (2011).
- [107] M. To Baben, D. Music, J. Emmerlich, and J. M. Schneider, *Scripta Mater.* **65**, 735 (2011).
- [108] L. Zhou, D. Holec, and P. H. Mayrhofer, *J. Phys. D: Appl. Phys.* **46** 365301 (2013).
- [109] P. Steneteg, B. Alling, and I. A. Abrikosov, *Phys. Rev. B* **85** 144404 (2012).
- [110] N. Shulumba, B. Alling, O. Hellman, E. Mozafari, P. Steneteg, M. Odén, and I. A. Abrikosov, *Phys. Rev. B* **89** 174108 (2014).
- [111] B. Alling, L. Hultberg, L. Hultman, and I. A. Abrikosov, *Appl. Phys. Lett.* **102** 031910 (2013).
- [112] L. Zhou, D. Holec, and P. H. Mayrhofer, *J. Appl. Phys.* **113** 043511 (2013).
- [113] B. Alling, T. Marten, and I. A. Abrikosov, *Phys. Rev. B* **82**, 184430 (2010).
- [114] B. Alling, T. Marten, and I. A. Abrikosov, *Nat. Mater.* **9**, 283 (2010).
- [115] B. L. Gyorffy, A. J. Pindor, J. Staunton, G. M. Stocks, and H. Winter, *Journal of Physics F: Metal Physics* **15**, 1337 (1985).
- [116] P. Soven, *Phys. Rev.* **156**, 809 (1967).
- [117] L. Zhou, F. Körmann, D. Holec, M. Bartosik, B. Grabowski, J. Neugebauer, and P. H. Mayrhofer, *Phys. Rev. B* **90** 184102 (2014).
- [118] Y. Kim, H. Lee, Y. Kim, K. Shin, W. Jung, and J. Han, *Surf. Coat. Technol.* **201**, 5547-5551 (2007).

---

# Chapter 2

## Computational methods

---

This chapter aims to present theoretical foundations and related methods used throughout this thesis. Firstly, the basic overview of the Density Functional Theory is introduced, along with the way of treating systems exhibiting strong correlation effects. Next, methods related to modeling of disordered systems, lattice vibrational effects and mechanical properties are given. Finally, a short introduction to software packages used in this thesis is given at the end of this chapter.

### 2.1 Density Functional Theory

#### 2.1.1 Formulation of the many-body problem

The many-body problem is a general name for a vast category of physical problems pertaining to the properties of microscopic systems made of a large number of interacting particles. The key point to understand material's behavior at the atomic scale is to solve the quantum-mechanical Schrödinger equation [1] in the form

$$H\Psi(\mathbf{r}_i, \mathbf{R}_I) = E\Psi(\mathbf{r}_i, \mathbf{R}_I) \quad (2.1)$$

where  $H$  is the Hamiltonian operator, including all relevant interactions between the electrons and atomic nuclei, and taking the following form

$$\begin{aligned} H &= T_e(\mathbf{r}_i) + T_N(\mathbf{R}_I) + V_{Ne}(\mathbf{r}_i, \mathbf{R}_I) + V_e(\mathbf{r}_i) + V_N(\mathbf{R}_I) \\ &= -\sum_i \frac{\hbar^2}{2m_e} \nabla_{\mathbf{r}_i}^2 - \sum_I \frac{\hbar^2}{2M_I} \nabla_{\mathbf{R}_I}^2 - \sum_{i,I} \frac{Z_I e^2}{|\mathbf{r}_i - \mathbf{R}_I|} \\ &\quad + \frac{1}{2} \sum_{i \neq j} \frac{e^2}{|\mathbf{r}_i - \mathbf{r}_j|} + \frac{1}{2} \sum_{I \neq J} \frac{Z_I Z_J e^2}{|\mathbf{R}_I - \mathbf{R}_J|} \end{aligned} \quad (2.2)$$

---

In the above equation,  $m_e$  and  $M_I$  are the mass of electrons and ions, respectively,  $\mathbf{r}_i$  and  $\mathbf{R}_I$  denotes the coordinates for each of electrons and ions, respectively.  $Z_I$  denotes the atomic number of an ion  $I$ . Finally,  $E$  is the total energy of the system under consideration. The simplest Hamiltonian operator  $H$  contains five types of energy contributions: the kinetic energies of electrons and nuclei,  $T$ , the electrostatic interactions between electrons and nuclei,  $V_{Ne}$ , the Coulombic interactions of electrons,  $V_e$ , and finally the interactions of nuclei,  $V_N$ . To solve this equation is computationally very expensive, and in practice it is possible only for small systems. Therefore, several approximations have to be made for the effective solution of Eq. 2.1.

### *The Born-Oppenheimer approximation*

In Eq. 2.2, the mass ratio of nuclei and electrons is in the order of  $10^3$ - $10^4$ , which implies that nuclei move significantly slower than electrons and consequently the treatment for the dynamics of nuclei and electrons can be decoupled as both take place of different time scales (electron excitations are typically  $\sim 10^{-16}$  s, while representative vibrational frequencies  $\sim$  THz range correspond to  $\sim 10^{-12}$  -  $10^{-13}$  s); When dealing with the movement of electrons, nuclei can be viewed as *frozen* and present a constant external potential with zero kinetic energy; On the other hand, the fast moving electrons create a negative uniformly distributed charge potential for the nuclei. From the electrons' point of view, the interaction between the nuclei reduces to a constant, and since an additive constant to the potential does not affect the solution of the Schrödinger equation, we can set it to 0. This procedure is known as the Born-Oppenheimer or adiabatic approximation [2]. Finally, under this approximation, the many-body Hamiltonian is simplified to

$$H = T_e(\mathbf{r}_i) + V_{ext}(\mathbf{r}_i, \mathbf{R}_I) + V(\mathbf{r}_i) \quad (2.3)$$

The Born-Oppenheimer approximation is a very useful simplification. However, once the interaction between electrons and nuclei is not negligible, for example when studying the

---

electron-phonon interactions, the errors from this approximation have to be considered.

Although the many-body Hamiltonian is simplified to Eq. 2.3, it is still impossible to solve the corresponding Schrödinger equation for real materials systems due to the Coulombic interactions of electrons. Therefore, further simplifications need to be done. One famous and successful method is the Hartree-Fock approximation [3,4]. Hartree neglected the Pauli exclusion principle, and proposed an ansatz for the form of the electron wave function using independent electrons, and replacing the electrostatic electron-electron interaction with an effective Hartree potential from all other electrons. Consequently, the total wave function describing the set of electrons is a sum of *single-electron* wave functions

$$\Psi(\mathbf{r}) = \sum_i \phi_i(\mathbf{r}_i) \quad (2.4)$$

In this case, the expectation value of the Hamiltonian operator for the system has the form

$$E = \langle \Psi | H | \Psi \rangle = \sum_i \langle \phi_i(\mathbf{r}_i) | H | \phi_i(\mathbf{r}_i) \rangle = \sum_i E_i \quad (2.5)$$

However, the energies derived from the Hartree method are not accurate enough due to the neglected electron–electron exchange interactions (Pauli exclusion principle). Later in 1930, Fock described an improvement for the Hartree method by adopting the Slater determinant, which makes the electron wave function to fulfill the Pauli exclusion principle and takes the form as follow

$$\Psi(\mathbf{r}) = \sum_i \phi_i(\mathbf{r}_i) \frac{1}{\sqrt{N!}} \det\{\phi_1(\mathbf{r}_1) \phi_1(\mathbf{r}_1) \dots \phi_i(\mathbf{r}_i)\} \quad (2.6)$$

Finally, the problem for a set of electrons is formulated as to minimize the total energy by looking for a series of *single-electron* wave functions. This is the central idea of the Hartree-Fock method and plays an important role in quantum chemistry.

In the Hartree-Fock method, however, the independent electron assumption and the introduction of an effective potential from the averaged potential exclude the correlation effects. This can be illustrated by a fact that two electrons cannot stay very close to each other due to the existence of the Coulomb repulsion. Another drawback of the Hartree-Fock method is that the

---

solution for single-electron wave functions is a daunting task, due to the degree of freedom of single-electron wave function forms, which becomes more obvious for larger system.

### 2.1.2 Theorems of Hohenberg and Kohn

Density functional theory (DFT) is based on a ground breaking work of Hohenberg and Kohn published in 1964 [5], and has been proven to be an exact theory for many-body systems; nowadays it is widely used for solid state calculations. The basic idea behind the DFT is that instead of the extremely sophisticated wave function  $\Psi(\mathbf{r})$ , it considers the electron density  $\rho(\mathbf{r})$ . This is a function of only 3 variables, which makes the quantum mechanical calculations for the large system possible due to the significant reduction of computational resources. Two important theorems serve as the basis for the theory as follows.

- i. The external potential  $V_{ext}(\mathbf{r}_i)$  of any quantum mechanical system is determined by the ground state density  $\rho(\mathbf{r})$  alone, up to an additive constant.
- ii. There exists a universal functional  $E[\rho]$  of the electronic density  $\rho(\mathbf{r})$ , which is independent of the external potential  $V_{ext}(\mathbf{r}_i)$ . The global minimum value of this energy functional  $E[\rho]$  is corresponding to the exact ground state electron density  $\rho(\mathbf{r})$  of the investigated system, and also is the exact ground state energy of the system. In other words, the energy functional  $E[\rho(\mathbf{r})]$  determines the exact ground state energy and density.

The first theorem gives a one-to-one relationship, so once the electron density of the system is determined, the corresponding external potential is also fully given, and subsequently all the properties of the system. The second theorem guarantees that once we find a density that makes energy functional  $E[\rho]$  reach its global minimum point, this charge density determines the ground state and the exact ground state energy.

---

### 2.1.3 Kohn-Sham equations

While the above theorems clearly sketch the power of the density functional approach to solve a many-body problem, the key point how to find the energy functional  $E[\rho]$  and the corresponding electronic density  $\rho(\mathbf{r})$  is still mysterious. After the publication of the Hohenberg-Kohn theorems, a scheme for practical addressing this issue was published in another paper by Kohn and Sham and it is known as the Kohn-Sham theorem [6]. The essence of the Kohn-Sham theorem is that the ground state density of an interacting system of interest can be determined by calculating the ground-state density of an auxiliary non-interacting system in an effective external potential. This statement makes a great improvement to the earlier density functional approaches, and has become a foundation for the modern methods of density functional theory. Instead of solving a  $3N$ -D Schrödinger equation for the many-body electron wave function, the Kohn-Sham theorem states that it is sufficient to solve  $N$  simple 3-D one-electron Schrödinger equation for a system with  $N$  independent electrons without interactions, which take the following form:

$$\left( -\frac{\hbar^2}{2m_e} \nabla^2 + V_{KS}(\mathbf{r}) \right) \phi_i(\mathbf{r}) = \varepsilon_i \phi_i(\mathbf{r}) \quad (2.7)$$

where the effective potential  $V_{KS}$  reads

$$V_{KS}(\mathbf{r}) = V_{ext} + \frac{e^2}{4\pi\epsilon_0} \int \frac{\rho(\mathbf{r}')}{|\mathbf{r}' - \mathbf{r}|} d^3\mathbf{r}' + \frac{\delta E_{xc}[\rho]}{\delta\rho(\mathbf{r})} . \quad (2.8)$$

In the above equation,  $V_{ext}$  denotes the external potential acting on the interacting system of electrons (e.g., the potential background from ions). The second term denotes the Hartree term, and it is given by the electron density rather than by individual electrons.  $E_{xc}[\rho]$  is the exchange-correlation energy functional, and contains the kinetic energy difference between the exact and non-interacting systems as well as the Coulomb interaction of electrons with the exchange-correlation hole. The exchange-correlation hole is the direct consequence of

---

exchange-correlation effects and can be interpreted that in contrast with the classical description of the un correlated electrons, the electrons have to obey Fermi statistics due to Pauli exclusion principle and other non-classical Coulomb interactions and always keep apart to give way to express the exchange and correlation contributions, which finally results in a hole surrounding each electron with keeping other electrons from approaching it. In Eq. 2.7, the exchange-correlation energy,  $E_{xc}[\rho]$ , electron density,  $\rho(\mathbf{r})$ , and the exchange-correlation potential,  $V_{xc} = \frac{\delta E_{xc}[\rho]}{\delta \rho(\mathbf{r})}$  are unknown variables. They are, however, not independent, and hence their solution requires a self-consistent scheme through an iterative procedure.

### 2.1.4 Exchange-correlation potential

As mentioned above, the exact form of the exchange-correlation functional in Kohn-Sham equation is not known. The key issue of the DFT is how to accurately express the exchange-correlation functional and various approximations have been proposed to proceed with the solution according to the Kohn-Sham procedure.

#### *Local density approximation (LDA)*

One of the most widely used approximation for the exchange-correlation energy functionals is the Local Density Approximation (LDA), which was proposed by Kohn and Sham in their original paper [6] in 1965. The XC energy functional in the local density approximation takes the following form

$$E_{xc}^{LDA}[\rho] = \int d\mathbf{r} \rho(\mathbf{r}) \varepsilon_{xc}(\rho(\mathbf{r})) \quad (2.9)$$

where  $\varepsilon_{xc}(\rho(\mathbf{r}))$  is the exchange-correlation energy per particle of a single electron in a uniform electron gas of density  $\rho(\mathbf{r})$ . The quantity  $\varepsilon_{xc}(\rho(\mathbf{r}))$  consists of two parts: exchange and correlation contributions

$$\varepsilon_{xc}(\rho(\mathbf{r})) = \varepsilon_x(\rho(\mathbf{r})) + \varepsilon_c(\rho(\mathbf{r})) \quad (2.10)$$

---

In this equation,  $\varepsilon_x(\rho(\mathbf{r}))$  denotes the exchange energy, and can be explicitly expressed using the Slater determinant as described above for the Hartree-Fock method. The correlation part,  $\varepsilon_c(\rho(\mathbf{r}))$ , includes the energy unconsidered in the exchange part, can be parametrized from quantum Monte-Carlo calculations of the homogeneous electron gas. Equation (2.11) works well very when the density,  $\rho(\mathbf{r})$ , varies slowly over the space, however this is often not the case for real systems. Consequently, this approximation fails once the charge density changes sharply, and shows poor performance for systems with highly localized charge distribution.

#### *Generalized gradient approximation (GGA)*

Another approach to approximate the exchange-correlation functional a Generalized Gradient Approximation (GGA) [7-9], which represents a series of functionals that consider also gradients of the charge density,  $\rho(\mathbf{r})$ . The GGA has been developed to correct for the shortcomings of the LDA, and takes a form

$$\begin{aligned} E_{xc}^{GGA}[\rho] &= \int d\mathbf{r} \rho(\mathbf{r}) \varepsilon_{xc}(\rho(\mathbf{r}), \nabla\rho(\mathbf{r})) \\ &= \int d\mathbf{r} \rho(\mathbf{r}) \varepsilon_{xc}(\rho(\mathbf{r})) F_{xc}(\rho(\mathbf{r}), \nabla\rho(\mathbf{r})) \end{aligned} \quad (2.12)$$

The quantity  $\varepsilon_{xc}(\rho(\mathbf{r}))$  in the second form of Eq. 2.11 has the same form as in Eq. 2.8.  $F_{xc}$  is an enhancement factor for the exchange-correlation effects, and can be parametrized to meet specific criteria.

#### *Beyond Density Functional Theory: DFT+U*

Although GGA presents (at least conceptual) improvement over LDA, there are still situations where both LDA and GGA fail. The reason is that in both LDA and GGA, the exchange-correlation energy,  $\varepsilon_x(\rho(\mathbf{r}))$  as mentioned above, is fitted to a homogenous electron gas, and hence always tends to delocalize the electrons over the crystal with an averaged Coulombic potential. However, in strong correlated materials, the electrons are highly localized and cannot be well described by the standard DFT methods due to the large Coulombic

---

repulsion. There are several ways to tackle this problem. One common and effective way is to add a Hubbard-like localized term [10], +U, to the LDA or GGA density functional, which has become known as LDA+U or GGA+U [11,12]. In general, the delocalized *s* and *p* electrons are sufficiently described by the standard DFT methods, and the Hubbard term is only applied on the partially filled *d* or *f* orbitals. It considers the generalized Hubbard model with an effective Hamiltonian to treat the strong correlated effects. Within the DFT+U scheme, the total energy functional of a system is written as a sum of the standard DFT part and a correction term which depends on the orbital occupation numbers of a given shell, and takes the following form

$$\begin{aligned}
E_{DFT+U}[\rho] &= E_{DFT}[\rho] + E_{Hub}[\{n_{mm'}^{l\sigma}\}] - E_{dc}[\{n^{l\sigma}\}] \\
&= E_{DFT}[\rho] + \frac{U-J}{2} \sum_{\sigma} \left[ \left( \sum_i n_{i,i}^{\sigma} \right) - \left( \sum_i \sum_j n_{i,j}^{\sigma} n_{j,i}^{\sigma} \right) \right]
\end{aligned} \tag{2.13}$$

where  $E_{DFT}$  represents the total energy functional from standard DFT methods and  $E_{Hub}$  denotes the Hubbard Hamiltonian to model the correlated states.  $E_{dc}$  is a double-counting term subtracted to avoid the double counting for the electron-electron interaction contribution of the shells according to the standard DFT methods. The Hubbard parameter U denotes the Coulomb energy cost to place two electrons at the same site. Stoner parameter J is a measure of the strength of the exchange correlation. Only the absolute difference U-J is important and its value is optimized to reach agreement with experimentally measured values, such as magnetic moments, band gap, lattice constants or total energies. In reality, it is often difficult (impossible) to achieve the good agreement for all the experimental results using a single optimized value for U-J.

### 2.1.5 Projector Augmented Wave method

The key step for the solution of a single particle Kohn-Sham equations is to expand the independent particle wave functions in a chosen basis set. One of the most computationally efficient basis sets is the one employing plane waves. According to the Bloch's theorem [13] and the fast Fourier transformation, the independent particle wave function for a system with a

---

periodic potential (crystal structure) has the form:

$$\begin{aligned}
\phi_i(\mathbf{r}) &= e^{i\mathbf{k}\cdot\mathbf{r}} u_{i,\mathbf{k}}(\mathbf{r}) \\
&= e^{i\mathbf{k}\cdot\mathbf{r}} \sum_i c_{i,\mathbf{k}} \phi_i^{basis}(\mathbf{r}) \\
&= \sum_i c_{i,\mathbf{k},\mathbf{G}} e^{i(\mathbf{k}+\mathbf{G})\cdot\mathbf{r}}
\end{aligned} \tag{2.14}$$

where  $\mathbf{G}$  is the reciprocal lattice vectors and  $\mathbf{k}$  denotes the wave vectors in the first Brillouin zone (BZ). For numerical reasons, this is sampled with reciprocal space grid points for the BZ integration.  $c_{i,\mathbf{k},\mathbf{G}}$  are the expansion coefficients that need to be determined.

In principle, the number of plane waves in the above equation is infinite, while in practice (limitations of the computational implementation), only a limited number of plane waves is included. The border is conventionally set by a criterion for maximum kinetic energy of plane

waves, the energy cut-off  $E_{cut} = \frac{\hbar^2}{2m_e} \mathbf{G}_{cut}^2$ . Another limitation is that the expansion of the wave

function requires a huge number of plane waves in the core region where it displays rapid oscillations (due to diverging potential). To address this problem, an alternative method known as the pseudopotential is used to smooth out the wave function in the region near nuclei, and hence to replace the huge number of plane waves needed. In this method, only the valence electrons are dealt with explicitly, and are described by a pseudo-wave functions with fewer nodes, while the collective effects of nuclei and core electrons are replaced by an effective, not diverging potential, which finally significantly reduces huge number of plane waves to be included, and makes the plane wave basis sets practical to be used.

In 1994, Blöchl made an extension for the pseudopotential method which is known as projector augmented wave method (PAW) [14], later further expanded by Kresse [15]. The PAW scheme combines ideas from both, the pseudopotential and the all-electron methods. By applying the frozen core approximation to the wave function of the core region, it achieves the accuracy corresponding to that of the all-electron methods, and obtains true valence wave functions with true nodes near nuclei, which makes accurate calculations of the magnetic and optical

---

properties possible, while it retains the efficiency and transferability as presented in pseudopotential method.

## **2.2 Treatment of disordered alloys**

The above chapter has detailed the fundamental theory used in the present work. The crucial question now is how to construct a physical model for the atomic structure of disordered system that can be used as an input for the first-principles calculations to study the relevant material properties. The main goal of this thesis is to study cubic B1 CrN-based coating systems which exhibit both chemical and magnetic disorder. The former class of disorder, chemical, refers to the random distribution of different atomic species in the lattice. In majority of cases within this thesis this means random solid solution on metal sublattice, however, we have in a similar manner treated also vacancies on the N sublattice simply by creating a solid solution of N atoms and vacancies with the desired composition. The latter class of disorder, magnetic, is related to the paramagnetic state of CrN, and origins from the magnetic spin polarization of Cr atoms. The here adopted method using collinear magnetism treats Cr atoms with spin up and spin down as two distinct entities, and the paramagnetic state is modeled as a solid solution of these two building units. There are three main approaches to model disordered solid solutions using first principles calculations.

### *Virtual crystal approximation (VCA)*

In virtual crystal approximation (VCA) [16] one creates a virtual atom with an effective potential corresponding to the average potential of all the alloy components to interpolate between the behavior of the actual atoms in the parent system. This approach offers the technically simplest way to deal with the random alloys and shows a great computational efficiency, which allows the calculations for the solid solutions to be carried out at the same cost for the small ordered structures. However, its drawbacks include that the potential is not self-averaging, and by its principle the method neglects local distortion around atoms. Moreover, the approach is suitable only for solid solutions of species with close (neighboring) atomic numbers. Consequently, the method is not state-of-the-art any more as in many cases the

---

accuracy of the predictions is poor, and it fails to reproduce some finer details of the random alloys.

#### *Coherent potential approximation (CPA)*

In contrast to VCA, coherent potential approximation (CPA) uses an effective medium self-consistently derived from the condition of stationary scattering based on one-electron Green's functions. The technique was originally employed by Soven [17] and Taylor [18] to study single-particle properties of elementary excitations in disordered binary alloys, and later was reformulated by Györfy in terms of multiple-scattering Korringa-Kohn-Rostoker (KKR) theory [19]. The inherent property of CPA is that it restores the crystal symmetry of the underlying lattice, which is computationally beneficial and may be a welcome feature in some applications. This is in contrast to the real nature of disordered alloys, in which the underlying lattice symmetry is lost due to the lack of perfect periodicity. A serious limitation of CPA comes from its single-site nature, which makes it unable to handle non-local fluctuations and limits the approach when applied to systems for which relaxation effects or local environment effects become important, such as the evaluation of the forces and force constants.

#### *The supercell approach*

With respect to the effective medium approaches (VCA and CPA), the *structural* theories take the atomic configurations into account. In the simplest case of a binary alloy with  $N$  sites, there are up to  $2^N$  possible atomic configurations. Many physical properties of alloys are highly correlated with the atomic configurations, so a natural way to evaluate a certain property of a disordered alloy would be to make the average over the ensemble of all these configurations. However, in practice it is very difficult to take all the configurations into account, and a compromise needs to be done.

One possible approach is the cluster expansion (CE) method generalized by Sanchez *et al.* [20] and has been used extensively in combination with first-principles calculations of physical properties of random alloys. Within the formalism of the CE method for a binary alloy, a desired physical property, for example the total energy  $E$ , is expressed as the average over the

---

ensemble of all the atomic configurations

$$E = \sum_n V_\alpha^n \Phi_\alpha^n \quad (2.15)$$

Here,  $V_\alpha^n$  is the effective cluster interaction (ECI) and  $\Phi_\alpha^n$  is the correlation function of  $n$ th order cluster  $\alpha$ . It can be expressed in terms of orthogonal basis functions generating the whole configurational space of alloy and a proper scalar product, as

$$\Phi_\alpha^n = \frac{1}{2^n} \sum_{i \in \alpha} \sigma_{\alpha_1} \sigma_{\alpha_2} \dots \sigma_{\alpha_n} \quad (2.16)$$

where  $\sigma_{\alpha_i}$  is a spin-like variable which takes a value +1 or -1 depending on whether the lattice point  $i$  of the cluster  $\alpha$  is occupied by an atom A or B. The sum runs over all the possible clusters  $\alpha$  with sizes up to  $2^n$  atoms. The size  $n$  of the cluster in the above equation can, in principle, be up to the size of a whole macroscopic system with the magnitude of  $10^{23}$ , implying that the expansion in Eq. 2.15 needs to be truncated due to practical reasons. Another drawback of CE method is that the ECIs are not known *a priori*, although there is no any technical difficulty in getting the correlation functions for a series of configurations with different sizes. One way to tackle this problem is simply to let the correlation functions  $\Phi_\alpha^n = 0$  in Eq. 2.15 for as many atomic clusters as possible, starting from the short ranged pair clusters with the strongest interactions. This procedure can be achieved by a smart design of the supercell with an optimized arrangement of atoms in the corresponding configurations, which finally yields the correlation functions close or equal to an ideal solid solution. This is the central idea of Special Quasi-random Structure (SQS) scheme, and was originally employed by Wei *et al.* [21,22].

A key parameter to evaluate the quality of an SQS is a set of its corresponding correlation functions. The possible procedure to find an SQS similar to the ideal solid solution is to minimize a squared norm of the difference of the correlation functions between the designed SQS and the ideal solid solution, which takes the form as follows

$$\sum_{\alpha} |\Phi_{\alpha} - \Phi_{\alpha}^{ideal}| \quad (2.17)$$

where  $\Phi_{\alpha}^{ideal}$  is the correlation function of cluster  $\alpha$  for the ideal solid solution and can be directly evaluated according to its composition. In the present work, the optimization takes into account pair clusters up to the seventh nearest neighbor (NN) distance. The pair interactions are considered to the strongest interaction, hence the higher order clusters, such as triples or quadruples are not considered for the minimization of the correlation function. A commonly used way to describe the correlation functions is Warren-Cowley short range order (SRO) parameters [23] and can be expressed as

$$\chi_j = 1 - \frac{P_{AB}^j}{x_B} \quad (2.18)$$

Where  $x_A$  are the concentrations of atoms A in the binary  $A_xB_{1-x}$  alloy.  $P_{AB}^j$  denotes the conditional probability of finding an B atom at a distance of  $d_j$  from a A atom. According to the value of SRO parameters, one can define the tendency for clustering or ordering as follows:

- i.  $\chi_j > 0$  for clustering.
- ii.  $\chi_j < 0$  for ordering.
- iii.  $\chi_j = 0$  for ideal random alloy.

Consequently, constructing an SQS close to a random alloy means to minimize the value of the expression:  $\sum_j^m \lambda_j |\chi_j|$ . Here,  $\lambda_j$  is the weight factor for  $j$ th shell.  $m$  is the maximum shell number for which SROs are optimized, and its value is typically between 5 and 7, depending on the underlying crystal lattice and supercell size. Due to the applied periodic boundary conditions, SROs evaluated for too large shell numbers do not contain any additional information. In the case of multicomponent  $A_iB_kC_m \dots$  ( $\sum i = 1$ ), a generalized expression firstly proposed De Fontaine *et al.* [24] shows the form

---


$$\chi_j^{B,C} = \frac{P_{BC}^j - x_C}{\delta_{BC} - x_C} \quad (2.19)$$

where  $\delta_{BC}$  equals zero if  $B \neq C$ . In the binary case, Eq. 2.19 obviously reduces to Eq. 2.18. One should note that each  $\chi_j$  in Eq. 2.19 just considers two atomic species and there are the number of independent SRO parameters of an  $n$ -component alloying solid solution is up to  $n/(n-1)/2$ . Details on the description of multicomponent short-range order can be found in Ref. [25]. In the present work, all the SQSs are constructed according to Eqs. 2.18 and 2.19. In practice, the size of SQS supercells is typically less than 100 atoms, implying that it is very difficult to capture all features of ideal solid solutions, in particular with dilute compositions. For some material system, the interaction is long-range and extends beyond the period of the supercell, in which case it becomes very difficult to converge the desired physical property with the supercell size. Recently, Seko *et al.* [26] has illustrated that the designed linear extrapolation is necessary for the prediction of the properties. More details about how to construct the SQS and the related issues can be found in Ref. [27].

## 2.3 Phonons

A phonon is a collective excitation associated with a vibration of atoms in a rigid crystal structure and determines a wide range of physical properties, such as structural stability, electrical conductivity, or phase transition temperature. For example, imaginary frequencies, i.e.  $\omega^2(\mathbf{k}, j) < 0$ , indicate a system is unstable; the lattice vibrational energy is an important contribution to the free energy hence impacting phase transformations. Consequently, it is very necessary to perform the phonon calculations to get a deep understanding of the material properties. Here, a brief introduction of the underlying theories is given, followed by a description of the related methods.

### 2.3.1 Lattice dynamics

Although the concept of a phonon was first introduced by Debye in 1912 [28], it took until 1954

---

when a classical quantum mechanics foundation of lattice dynamics was given by Born and Huang in their book [29]. Following the development of DFT, a relationship between electronic structure and lattice dynamics was established, which makes it possible to routinely perform phonon calculations. As mentioned before in Sec. 2.1.1, the dynamics of electrons and ions are decoupled within the Born-Oppenheimer approximation, and the Hamiltonian,  $H$ , for the lattice dynamic of ionic system reads

$$H = - \sum_I \frac{\hbar^2}{2M_I} \nabla_{\mathbf{R}_I}^2 + V(\mathbf{R}) \quad (2.20)$$

where  $\mathbf{R}$  denotes the set of all the nuclear coordinates  $\mathbf{R}_I$ , and  $V(\mathbf{R})$  is sum of the electronic ground state energy and electrostatic energy of the ions and can be parameterized in terms of ionic deviations. Making a Taylor expansion with respect to the equilibrium ionic configuration, the potential energy  $V(\mathbf{R})$  in Eq. 2.20 takes a form

$$V(\mathbf{R}) = V_0 + \sum_I \Phi_I \mathbf{R}_I + \frac{1}{2} \sum_{I,J} \Phi_{I,J} \mathbf{R}_I \mathbf{R}_J + \frac{1}{3!} \sum_{I,J,K} \Phi_{I,J,K} \mathbf{R}_I \mathbf{R}_J \mathbf{R}_K + \dots \quad (2.21)$$

where the first term  $V_0$  is a constant and denotes the electronic ground state energy. For the derivation of the lattice dynamics,  $V_0$  can be reduced to zero.  $\Phi_I$  in the second term denotes the force acting on an atom  $I$ , and naturally becomes zero at its equilibrium position.  $\Phi_{I,J}$  in the third term is a Hessian matrix of the energy potential, is and known as the interatomic force constant. It becomes the key part for a derivation of the phonon dispersion and takes the form

$$\Phi_{I,J} = \frac{\partial^2 V}{\partial \mathbf{R}_I \partial \mathbf{R}_J} \quad (2.22)$$

The third and higher order derivatives of the potential energy  $V(\mathbf{R})$  denote the anharmonic contribution to the potential energy. Within a so-called harmonic approximation, only the second derivatives of the potential energy  $V(\mathbf{R})$  are considered, while the higher terms are

---

omitted. A Fourier transformation of  $\Phi_{I,J}$  at a wavevector  $\mathbf{q}$  yields a dynamical matrix  $D_{I,J}(\mathbf{q})$

$$D_{I,J}(\mathbf{q}) = \frac{1}{\sqrt{M_I M_J}} N^{-1} \sum_{I',J'} \Phi_{I',J'} e^{i\mathbf{q} \cdot (\mathbf{R}_{I'} - \mathbf{R}_{J'})} \quad (2.23)$$

$$D(\mathbf{q})\mathbf{w}(\mathbf{q}s) = [\omega(\mathbf{q}s)]^2 \mathbf{w}(\mathbf{q}s) \quad (2.24)$$

where  $\mathbf{w}$  is an eigenvector and  $s$  denotes a band index. Through a diagonalization the dynamical matrix and solving Eq. 2.24, phonon frequencies,  $\omega$ , are obtained as square roots of the eigenvalues of the dynamical matrix. In practice, there are two popular approaches to the phonon calculations. The first one is a calculation of the linear response to a distortion in nuclear geometry of the charge density within density functional perturbation theory (DFPT). The second approach is known as the finite displacement method. In contrast to the finite displacement method, one of the major advantages of DFPT is that it is able to calculate the dynamical matrix at an arbitrary  $\mathbf{q}$ -vector exactly without introducing supercells. In addition to phonons, the DFPT method can also be used to obtain other physical quantities, such as Born effective charges or dielectric constants. The real problem of the DFPT method comes from its computational costs, which scale as  $O(n^4)$ . For a unit cell with several atoms, the computational demands for DFPT are close to that of the finite displacement method.

The phonon calculations in the present work were performed for the disordered alloys modeled with a series of SQSs with sizes up to  $\sim 100$  atoms and very low symmetry, which would have made it unreasonably consuming for the DFPT method. Therefore, the finite displacement method was employed to evaluate the force constant matrix,  $\Phi_{I,J}$ , in the present thesis.

### 2.3.2 Finite displacement method

The finite displacement method [30] is a fairly straightforward technique to calculate the force constant matrix by explicitly displacing the atoms of the system. As stated in the previous Section, the key to evaluate phonon contributions is to obtain the force constants matrix or its Fourier transformation, the dynamical matrix. In this method, the first step is to construct a

---

supercell from the unit cell. Its size should be large enough to avoid the artificial interaction caused by the periodic images. In order to fulfill  $\Phi_{i,j} \rightarrow 0$ , and also to avoid the effects from the periodic images, the size of supercell should be infinite, which is impossible in practice, and therefore a certain compromise has to be made. The second step is to apply a series of displacements on the atoms (which number can be reduced by considering the crystal symmetry), and to evaluate the forces induced by the displacements according to the Hellmann–Feynman theorem:

$$F_{\mathbf{R}} = -\frac{\partial V}{\partial \mathbf{R}} = -\langle \Psi | \nabla_{\mathbf{R}} H | \Psi \rangle . \quad (2.25)$$

In order to minimize the anharmonic effects, the magnitude of displacement should be tested, and the force is averaged from displacements in negative and positive directions. Once the forces are calculated, the dynamical matrix can be directly evaluated based on Eqs. 2.22 and 2.23. Finally, the phonon frequencies is evaluated using Eq. 2.24. Here one should notice, that the finite displacement method cannot account for the effects of vibration-induced dipole-dipole interaction on the phonon frequencies in polar materials, which induces a frequency splitting between the longitudinal optical (LO) and the transverse optical (TO) phonon modes, and is known as the LO-TO splitting [31]. The way to include this effect is to add a non-analytical term correction to the force constant matrix proposed by Wang *et al* [32], which can be evaluated from Born effective charge and dielectric tensors calculated using the DFPT.

### 2.3.3 Quasiharmonic approximation

In this section, a short introduction of quasiharmonic approximation is given. As mentioned in previous sections, harmonic approximation considers only the second derivative of potential energy without an explicit dependence on volume. However, phonons show a softening tendency at elevated temperatures, which increases the phonon entropy and stabilizes an expanded lattice. Quasiharmonic approximation assumes that phonons are volume-dependent by using the harmonic model of lattice dynamics at every volume. In this way, a part of

---

temperature effect can be included into the free energy through Helmholtz free energy at a constant volume, which takes the form

$$F(V,T) = E_0(V) + F_{vib}(V,T) + F_{el}(V,T) \quad (2.26)$$

where  $E_0(V)$  is the static total energy at 0 K at volume  $V$ .  $F_{vib}(V,T)$  denotes the harmonic lattice vibrational contributions to the free energy at a constant volume  $V$ , and based on the phonon density of states,  $g(\omega)$ , from the harmonic approximation, it can be expressed as

$$F_{vib}(V,T) = k_B T \int_0^\infty \ln \left[ 2 \sinh \frac{\hbar \omega}{2k_B T} \right] g(\omega) d\omega \quad (2.27)$$

$F_{el}(V,T)$  is the thermal electronic contribution, and can be calculated within the Sommerfeld approximation as

$$F_{el}(V,T) = -\frac{(\pi k_B T)^2}{6} N(\varepsilon_F, V) \quad (2.28)$$

where  $N(\varepsilon_F, V)$  is the electronic density of states at the Fermi level. Finally, within the quasiharmonic approximation, the Gibbs free energy,  $G$ , at a constant pressure,  $p$ , is defined as

$$G(p,T) = \min_V [F(V,T) + pV] \quad (2.29)$$

Here,  $\min_V$  denotes a minimization of the functions in the brackets with respect to the volume.

$F(V,T)$  is the Helmholtz free energy at a constant volume,  $V$ , as expressed by Eq. 2.26, including the static total energy, phonon contributions, and thermal electronic contributions. Eq. 2.29 includes a collective effect of the volume on the various energy terms, which each show different volume dependencies.

## 2.4 Prediction of mechanical properties

One of the aims of the alloying design directly related to industrial applications, is to find alloy candidates with superior mechanical properties,. The single crystal elastic constants obtained from first-principles calculations provide a parameter-free way for the prediction of mechanical properties at atomic level. The elastic response of the most general triclinic system (space group  $P1$ ) is determined by 21 independent elastic constants. In the present case of materials with a cubic B1 symmetry (NaCl prototype, space group  $Fm\bar{3}m$ ), the linear elastic response is fully specified by three independent components  $C_{11}$ ,  $C_{12}$ , and  $C_{44}$ , which can be represented with  $6 \times 6$  matrix as follows

$$C_{ij} = \begin{pmatrix} C_{11} & C_{12} & C_{12} & 0 & 0 & 0 \\ C_{12} & C_{11} & C_{12} & 0 & 0 & 0 \\ C_{12} & C_{12} & C_{11} & 0 & 0 & 0 \\ 0 & 0 & 0 & C_{44} & 0 & 0 \\ 0 & 0 & 0 & 0 & C_{44} & 0 \\ 0 & 0 & 0 & 0 & 0 & C_{44} \end{pmatrix}. \quad (2.30)$$

The problem is that the disordered alloys modeled using SQSs with space group  $P1$ , which results in 21 independent elastic constants. Tasnádi *et al.* [33] pointed out following a symmetry based projection technique that the full 21 independent elastic constants can be reduced to 3 cubic elastic constants, using a simple averaging as follows

$$\overline{C_{11}} = \frac{C_{11} + C_{22} + C_{33}}{3} \quad (2.31)$$

$$\overline{C_{12}} = \frac{C_{12} + C_{13} + C_{23}}{3} \quad (2.32)$$

$$\overline{C_{44}} = \frac{C_{44} + C_{55} + C_{66}}{3} \quad (2.33)$$

Another alternative to reduce the number of independent elastic constants for the SQSs is to try to construct the SQS by capturing the cubic elastic symmetry, which is in some sense at cost of the randomness even though the SQSs are smartly designed [34]. In general, there are two

---

routes to compute the elastic constants from first-principles calculations. The first one is the stress-strain method and the other one is the energy-strain method. The following part will give a short description for these two methods.

Bulk materials can be deformed in various ways: stretching, shearing, bending, twisting, *etc.* Each kind of deformation contributes exclusively to the elastic energy of a distorted material if the deformation is small within the elastic range. The deformation can be represented by a strain tensor,  $\boldsymbol{\varepsilon}$ , which is expressed as the symmetric part of the gradient of displacement:

$$\varepsilon_{ij} = \frac{1}{2}(\partial_i \varepsilon_j + \partial_j \varepsilon_i) . \quad (2.34)$$

The corresponding stress tensor,  $\boldsymbol{\sigma}_{ij}$ , takes the form

$$\sigma_{ij} = \frac{\partial U_0(\boldsymbol{\varepsilon})}{\partial \varepsilon_{ij}} . \quad (2.35)$$

Here,  $U_0$  is strain energy and can be expanded in a Taylor series as

$$\begin{aligned} U_0(\boldsymbol{\varepsilon}) &= U_0(0) + \sum_{i,j} \left( \frac{\partial U}{\partial \varepsilon_{ij}} \right)_{\mathbf{v}_0} \varepsilon_{ij} + \frac{1}{2} \sum_{i,j,k,l} \left( \frac{\partial^2 U}{\partial \varepsilon_{ij} \partial \varepsilon_{kl}} \right)_{\mathbf{v}_0} \varepsilon_{ij} \varepsilon_{kl} + \dots \\ &= A + \sum_{i=1}^3 \sum_{j=1}^3 B_{ij} \varepsilon_{ij} + \frac{1}{2} \sum_{i=1}^3 \sum_{j=1}^3 \sum_{k=1}^3 \sum_{l=1}^3 C_{ijkl} \cdot \varepsilon_{ij} \varepsilon_{kl} + \dots \end{aligned} \quad (2.36)$$

where the higher order derivatives are not included due to the assumption of linear elasticity. If all strains are zero, the strain energy and stresses are zero, i.e.,  $A=0$ . Since the Taylor expansion in Eq. 2.36 is done around equilibrium configuration, i.e. around minimum energy, the first derivatives of the strain energy with respect to strain must be 0, implying  $B_{ij}=0$ . Finally, the strain energy is represented fully in terms of the elastic constants,  $C_{ijkl}$ . Combining Eqs. 2.35 and 2.36, one obtains the Hooke's law

$$\sigma_{ij} = \sum_{k=1}^3 \sum_{l=1}^3 C_{ijkl} \cdot \varepsilon_{kl} \quad (i, j = 1, 2, 3) , \quad (2.37)$$

and the strain energy can be expressed as

$$U_0(\boldsymbol{\varepsilon}) = \frac{1}{2} \sum_{i=1}^3 \sum_{j=1}^3 \sum_{k=1}^3 \sum_{l=1}^3 C_{ijkl} \cdot \varepsilon_{ij} \varepsilon_{kl} \quad . \quad (2.38)$$

Here,  $C_{ijkl}$  are the components of the fourth rank stiffness tensor, which has up to 81 components. By imposing several symmetry requirements, that is

$$C_{ijkl} = C_{jikl} = C_{ijlk} \quad (2.39)$$

and also the relationship

$$C_{ijkl} = \frac{\partial^2 U_0(\boldsymbol{\varepsilon})}{\partial \varepsilon_{ij} \partial \varepsilon_{kl}} = \frac{\partial^2 U_0(\boldsymbol{\varepsilon})}{\partial \varepsilon_{kl} \partial \varepsilon_{ij}} = C_{klij} \quad , \quad (2.40)$$

the number of 81 independent components is reduced to 21 independent components as stated above. Finally, using the Voigt notation: 11  $\rightarrow$  1, 22  $\rightarrow$  2, 33  $\rightarrow$  3, 23  $\rightarrow$  4, 13  $\rightarrow$  5, and 12  $\rightarrow$  6, Eqs 2.37 and 2.38 can be expressed as

$$\sigma_i = \sum_{j=1}^6 C_{ij} \cdot \varepsilon_j \quad (i = 1, 2, \dots, 6) \quad (2.41)$$

$$U_0(\boldsymbol{\varepsilon}) = \frac{1}{2} \sum_{i=1}^6 \sum_{j=1}^6 C_{ij} \cdot \varepsilon_i \varepsilon_j \quad (2.42)$$

Then the route based on Eq. 2.41 (Hooke's law) to compute the elastic constants is known as the stress-strain approach. Employing Eq. 2.42 expressing a variation of the strain energy  $U$  with the applied strain, corresponds to the energy-strain approach. Comparing Eqs. 2.41 and 2.42, one finds that the energy-strain approach is much more computation-time consuming than the stress-strain method as more deformation modes need to be applied. In a recent work by Caro *et al.* [35] showed that stress-strain method converges much faster than the energy-strain approach with respect to the number of plane waves and  $\mathbf{k}$  points. Caro *et al.* [35] stated that the stress-strain method is more robust than the energy-strain approach for the elastic constants calculations. In the present work, the stress-strain method is mainly used to evaluate the full 21 independent elastic constants for each SQS and then averaging the relative elastic constants according to Eqs. 2.31 - 2.33.

---

## 2.5 Introduction to VASP and phonopy

The Vienna Ab-initio Simulation Package (VASP), which was developed by Kresse *et al.* [15] in Computational Materials Physics group, Faculty of Physics, Universität Wien, Austria, is a program for performing *ab initio* quantum mechanical molecular dynamics (MD) using either pseudopotentials, or the projector augmented wave (PAW) method potentials, and a plane wave basis set. The majority of work in the present thesis was done using this software.

Phonopy is an open source package written in Python for phonon calculations within the harmonic and quasi-harmonic approximations, and has been developed by Togo *et al.* [36] at Elements Strategy Initiative for Structural Materials, Kyoto University, Japan. It requires the force calculations from a DFT force calculator as input (e.g., from VASP as used in the present work), in order to evaluate the eigenvalues of force constants matrix and its dynamical matrix. The method implemented in Phonopy is the finite displacement method. The majority of the results presented in chapter 3 were obtained using this program together with VASP.

---

# References

- [1] E. Schrödinger, Phys. Rev. **28**, 1049 (1926).
- [2] M. Born and R. Oppenheimer, Annalen der Physik **84**, 457 (1927).
- [3] V. Fock, Phys. Rev **35**, 210 (1930).
- [4] D. R. Hartree, Proc. Cambridge Phil. Soc. **24**, 89 (1928).
- [5] P. Hohenberg and W. Kohn, Phys. Rev. **136**, B864 (1964).
- [6] W. Kohn and L. J. Sham, Phys. Rev. **140**, A1133 (1965).
- [7] J. P. Perdew, K. Burke, and M. Ernzerhof, Phys. Rev. Lett. **77**, 3865 (1996).
- [8] A. D. Becke, Phys. Rev. A **38**, 3098 (1988).
- [9] J. P. Perdew and Y. Wang, Phys. Rev. B **45**, 13244 (1992).
- [10] J. Hubbard, in *Proceedings of the Royal Society of London A: Mathematical, Physical and Engineering Sciences* (The Royal Society, 1964), pp. 401.
- [11] V. I. Anisimov, F. Aryasetiawan, and A. I. Lichtenstein, J. Phys.: Condens. Matter **9**, 767 (1997).
- [12] V. I. Anisimov, J. Zaanen, and O. K. Andersen, Phys. Rev. B **44**, 943 (1991).
- [13] B. F., Z. Physik A **52**, 555 (1928).
- [14] P. E. Blöchl, Phys. Rev. B **50**, 17953 (1994).
- [15] G. Kresse and D. Joubert, Phys. Rev. B **59**, 1758 (1999).
- [16] L. Bellaïche and D. Vanderbilt, Phys. Rev. B **61**, 7877 (2000).
- [17] P. Soven, Phys. Rev. **156**, 809 (1967).
- [18] D. W. Taylor, Phys. Rev. **156**, 1017 (1967).
- [19] B. Gyorffy, Phys. Rev. B **5**, 2382 (1972).
- [20] J. M. Sanchez, F. Ducastelle, and D. Gratias, Phys. A **128**, 334 (1984).
- [21] S. H. Wei, L. G. Ferreira, J. E. Bernard, and A. Zunger, Phys. Rev. B **42**, 9622 (1990).
- [22] A. Zunger, S. H. Wei, L. G. Ferreira, and J. E. Bernard, Phys. Rev. Lett. **65**, 353 (1990).
- [23] J. Cowley, J. Appl. Phys. **21**, 24 (1950).
- [24] D. de Fontaine, J. Appl. Crystallogr. **4**, 15 (1971).
- [25] A. V. Ceguerra, R. C. Powles, M. P. Moody, and S. P. Ringer, Phys. Rev. B **82**, 132201

---

(2010).

[26] A. Seko and I. Tanaka, Phys. Rev. B **91**, 024106 (2015).

[27] D. Holec, L. Zhou, R. Rachbauer, and P. H. Mayrhofer, in *Density Functional Theory: Principles, Applications and Analysis* (2013), pp. 259.

[28] P. P. Debye, Ann. Phys. **39** (1912).

[29] M. Born, K. Huang, and M. Lax, AJP **23**, 474 (1955).

[30] K. Parlinski, Z. Li, and Y. Kawazoe, Phys. Rev. Lett. **78**, 4063 (1997).

[31] S. Baroni, S. de Gironcoli, A. Dal Corso, and P. Giannozzi, Rev. Mod. Phys. **73**, 515 (2001).

[32] Y. Wang, J. Wang, W. Wang, Z. Mei, S. Shang, L. Chen, and Z. Liu, J. Phys.: Condens. Matter **22**, 202201 (2010).

[33] F. Tasnáli, M. Odín, and I. A. Abrikosov, Phys. Rev. B **85**, 144112 (2012).

[34] D. Holec, F. Tasnáli, P. Wagner, M. Friák, J. Neugebauer, P. H. Mayrhofer, and J. Keckes, Phys. Rev. B **90**, 184106 (2014).

[35] M. A. Caro, S. Schulz, and E. P. O'Reilly, J. Phys.: Condens. Matter **25**, 025803 (2013).

[36] A. Togo, F. Oba, and I. Tanaka, Phys. Rev. B **78**, 134106 (2008).

---

# Chapter 3

## Structural stability and thermodynamics of CrN magnetic phases

---

### 3.1 Motivation

As stated in the introduction part, there are many experimental reports on CrN due to its wide applicability in the industrial area [1-12] and in the case of theoretical calculations, CrN received great attention mainly due to its electronic and magnetic properties [13-20], while only a few papers have been devoted to its phase stability [16,21]. Most theoretical studies assumed CrN in the non-magnetic rather than in the paramagnetic (PM) state [11,22-26], while experiments clearly reveal non-vanishing local magnetic moments even above the Néel temperature [27]. The reason for this serious approximation is largely related to the challenges in describing the dynamic magnetic disorder in the paramagnetic state. Recently, Alling *et al.* [16] employed the special quasi-random structures (SQS) approach [28] to simulate the magnetic disorder in PM B1-CrN and concluded that the magnetic disorder together with strong correlation effects in the PM B1-CrN phase largely influence the Gibbs energy. Including the magnetic entropy, a phase transition between the high-temperature PM B1-CrN phase and the low-temperature antiferromagnetic (AFM) ground state with a distorted orthorhombic (Ortho) structure was predicted at 498 K [16]. In their treatment, however, the vibrational contribution to the free energy was not taken into account, despite the known significant influence on thermodynamic properties [29]. Very recently, the same group accomplished to include vibrational contributions via disordered-local-moment molecular-dynamics-simulations in conjunction with the temperature-dependent effective potential (DLM-MD-TDEP) method [30]. The underlying DFT calculations were based on the local density approximation (LDA) with an on-site Coulomb interaction term,  $U$ . An improved phase transition temperature of 381

---

K has been found, which is, however, still  $\sim 100$  K higher than the experimental observations. Despite the recent progress, many questions are still unanswered. A decisive issue is for instance the impact of the underlying exchange-correlation (xc)-functional on the thermodynamic stability, which is so far not known. Recently, we have developed an alternative method to compute the vibrational Gibbs energy contributions based on a spin-space averaging (SSA) method [31]. Our method does not require computationally demanding molecular dynamics simulations and can be therefore efficiently employed to scan the influence of different xc-functionals as will be performed in the present work.

When discussing phase stability, it is important to distinguish energetic (meta)stability, mechanical and dynamical stability. The first one is related to the Gibbs free energy,  $G$ , which predicts the phase with the lowest  $G$  to be the most stable one, all other phases being metastable or even instable. Regarding mechanical stability the Born-Huang criteria [32] for elastic constants have to be fulfilled. The dynamical stability considers the complete vibrational spectrum of a material; a material is (dynamically) stable when no imaginary phonon frequencies exist. In other words, the Born-Huang mechanical stability criteria *provide a necessary* condition for the dynamical stability, but not a *sufficient* one. For instance, by explicitly computing phonon dispersions, imaginary frequencies can occur at the Brillouin zone boundary (indicating dynamical instability), even if the Born-Huang criteria are fulfilled [33]. It is therefore necessary to perform explicit phonon calculations to evaluate the dynamical stability. Such an evaluation of the dynamical stability is computationally much more expensive as calculating the full tensor of elastic constants (in particular for systems with large numbers of atoms in their unit cells). Consequently, explicit phonon computations have been so far mostly neglected and we therefore present here a complete study of CrN phase stabilities.

The nonmagnetic (NM) B1-CrN phase has been reported to be energetically unfavorable with respect to other spin arrangements with non-zero local magnetic moments [16]. It is however not clear whether NM B1-CrN is dynamically unstable with respect to mechanical distortions, i.e. whether the elastic constants fulfill criteria for mechanical stability [32] and/or if there are any imaginary frequencies in its phonon dispersion. Another question of interest is whether the

---

NM B1-CrN can be stabilized, e.g. by high pressure, and thus represents a potential metastable state. The literature data based on density functional theory (DFT) suggest its mechanical stability [22,23,25,26], but an explicit evaluation via the full phonon spectrum analysis will be presented for the first time in the present paper.

As mentioned above, another important and so far unresolved issue is the impact of strong electron correlation effects on the stability of CrN phases. For example, it has been argued that LDA+U is more suitable than the generalized gradient approximation (GGA) [16], but a comprehensive study employing GGA+U, which might turn out to be even more appropriate, is so far missing. Additionally, the impact of the previously proposed value for the on-site Coulomb interaction parameter  $U$  on the vibrational free energy has not been discussed so far as well [30].

The aims of this chapter can be hence summarized as follows: (1) To comprehensively investigate the energetic, mechanical and dynamical stability of CrN including non-magnetic, anti-ferromagnetic, ferromagnetic and paramagnetic configurations, (2) to elucidate the impact of the chosen xc-functional approximation and  $U$ -parameter, and (3) to compute the thermodynamic stability of the different variants. Firstly, elastic constants are calculated and used to evaluate the mechanical stability based on the Born-Huang mechanical stability criteria. As discussed above, these stability criteria might be not sufficient. Therefore, in a second step, phonon calculations are performed to prove the dynamical stability. Eventually, Gibbs free energies based on the SSA formalism [31] including vibrational and magnetic contributions are computed to predict the phase transition in CrN employing GGA, GGA+U and LDA+U approaches, and the thus obtained transition temperatures are compared with available experimental results. Furthermore, thermodynamic properties such as lattice thermal expansion coefficient and specific heat capacity of the high-temperature PM B1-CrN are presented and, where applicable, compared to experimental data. In particular, we compare our DFT computed linear thermal expansion coefficient with a set of newly determined experimental data obtained by the wafer curvature method and from a single-phase face-centered cubic B1-CrN thin film.

## 3.2 Methods

### 3.2.1 Static DFT calculations

As discussed above, unlike other early transition metal nitrides, CrN requires extra efforts due to the non-zero local magnetic moments of the Cr atoms. In this work the SQS approach [16,28,34] is used to model the PM state by employing  $2 \times 2 \times 2$  cubic supercells with 32 Cr and 32 N atoms and randomly distributing the spin-up and spin-down moments on the Cr-atoms. In order to provide a complete picture of phase stabilities, we consider in the present work also B1-CrN with ferromagnetic (FM) and AFM ordering consisting of alternating single (001) planes of Cr atoms with spin up and spin down in addition to the NM B1, PM B1 and AFM Ortho structures of CrN (cf. the crystal structures in Fig.3.1).

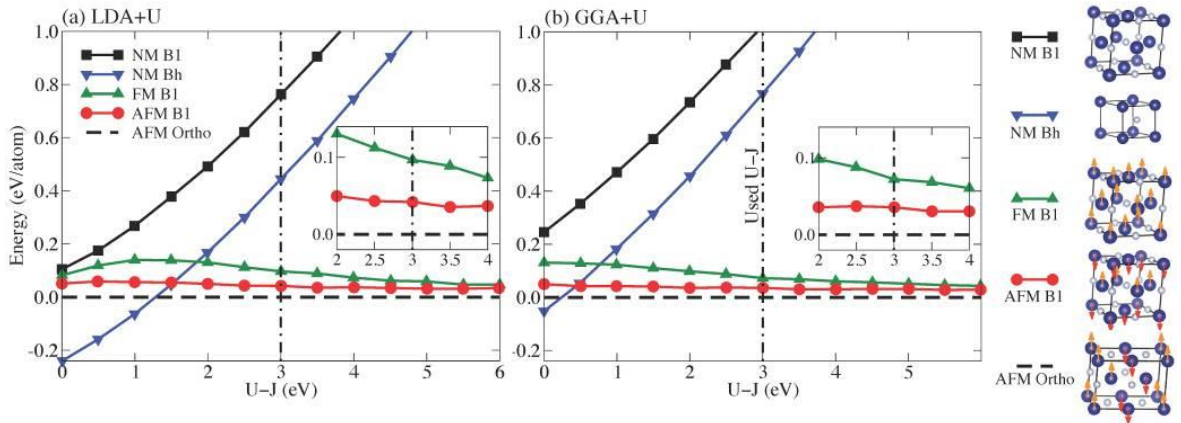


Figure 3.1:  $T=0$  K total energy of the stoichiometric compound CrN in different structural and magnetic configurations as a function of the U-J term in the (a) LDA+U and (b) GGA+U schemes. The energy of the AFM Ortho-CrN phase is used as reference. The vertical dash-dotted line indicates the U-J used in the present work. The crystal structures to the right show the various investigated atomic and magnetic arrangements with the blue (white) balls indicating Cr (N) atoms. The insets show the total energies of FM B1-CrN and AFM B1-CrN with respect to AFM Ortho-CrN phase.

All first-principles calculations are based on DFT as implemented in the Vienna *Ab initio* Simulation Package (VASP) [35,36]. The ion-electron interactions are described by the

---

projector augmented wave method (PAW) [37] with a plane wave energy cutoff of 500 eV. The semi-core  $p$  states are treated as valence for Cr ( $3p^6 3d^5 4s^1$ ) while there are 5 valence electrons for N ( $2s^2 2p^3$ ). In order to take into account the strong on-site Coulomb interaction ( $U$ ) caused by the localized  $3d$  electrons of Cr, the local density approximation (LDA) and the generalized gradient approximation (GGA) plus a Hubbard  $U$ -term method is adopted within the framework of the Dudarev formulation [38,39]. Here, only the difference  $U-J$ , with  $J$  being the screened exchange energy, determines the material properties. Alling *et al.* [16] tested  $U-J$  in the range from 0 to 6 eV in their previous LDA+ $U$  study, and found  $U-J = 3$  eV to yield an optimal description of the structural and electronic properties of AFM and PM-CrN. Apart from structural and electronic properties, the inclusion of the  $U$ -parameter is also decisive for the correct description of the magnetism in CrN. This is exemplified in Fig.3.1, where we show that a too small value of the  $U-J$  parameter might even yield a wrong magnetic ground state for CrN. The total energy was evaluated for a number of structures as function of  $U-J$  ranging from 0 to 6 eV. For the sake of clarity, only a few structures are listed. It becomes obvious that both, standard LDA and GGA-PBE [40] predict the NM Bh-CrN phase (TaN prototype, space group  $C2mm$ ) to be the ground state of CrN, which disagrees with experimental observations of AFM Ortho-CrN [1]. The energy difference between AFM Ortho-CrN and AFM B1-CrN becomes smaller as the  $U-J$  value increases. Our results suggest that the value of  $U-J$  should be larger than 1.5 eV (LDA) or 0.25 eV (GGA) in order to obtain AFM Ortho-CrN as the ground state. An accurate determination of the  $U$ -parameter is difficult from both, experiment as well as theory, as in detail discussed by Alling *et al.* in [16]. In order to allow a thoroughly comparison with the previous results we adopted the value of  $U-J=3$  eV also for the present DFT+ $U$  calculations. To demonstrate the impact of the on-site Coulomb interaction on the vibrational properties we furthermore applied the conventional GGA-PBE (without the  $U$ -term) for the computation of elastic constants and phonon properties. Eventually, the impact on the phase transition temperature for choosing an even larger value for  $U-J$ , i.e.  $U-J=4$  eV, is discussed in terms of total and magnetic energy contributions.

The energy convergence criterion for electronic self-consistency was set to 0.1 meV/atom. The

---

Monkhorst-Pack scheme [41] was used to construct  $k$ -meshes of  $3 \times 3 \times 3$  (128-atom supercells),  $3 \times 4 \times 5$  (96-atom supercells),  $5 \times 5 \times 5$  (64-atom supercells),  $12 \times 12 \times 12$  (8-atom cells), and  $21 \times 21 \times 21$  (2-atom cells). The elastic constants were calculated using the stress-strain approach discussed in detail in our previous work [34].

### 3.2.2 Phonon calculations

The phonon calculations for NM, FM and AFM B1-CrN were performed employing  $2 \times 2 \times 2$  supercells consisting of 64 atoms constructed from a conventional face-centered cubic cell with 8 atoms. For AFM Ortho-CrN,  $2 \times 3 \times 2$  supercells with 96 atoms were created from its unit cell with 8 atoms. Super cell size convergence tests were performed for NM and FM B1-CrN using up to  $4 \times 4 \times 4$  supercells (based on primitive cells with 2 atoms) containing 128 atoms. The 64-atoms SQS adopted to simulate the paramagnetic state in B1-CrN was also used for the corresponding phonon calculations. Note that the computation of vibrational properties for paramagnetic materials is a tremendous task due to the delicate coupling of magnetic and atomic degrees of freedom [42]. We use here our recently developed statistical spin space averaging (SSA) procedure [31], which allows the computation of forces in paramagnetic materials. Within the SSA approach, the SSA force on an atom  $j$  is given as the gradient on the SSA free energy surface  $F^{\text{SSA}}$  as [31]:

$$F_j^{\text{SSA}} = -\frac{\partial F^{\text{SSA}}}{\partial R_j} = \sum_m p_m F_j^{\text{HF}} \{(R_j), \sigma_m\}, \quad (3.1)$$

where  $F_j^{\text{HF}} \{(R_j), \sigma_m\}$  are the Hellmann-Feynman forces for an individual magnetic configuration  $\sigma_m$  and  $p_m = \exp[-\frac{E^{B0} \{(R_j), \sigma_m\}}{k_B T}]$  denotes the Boltzmann weights. As discussed in Ref. [31], the summation over different magnetic configurations,  $\sigma_m$ , in the above equation can be expressed by a sum over lattice symmetry operations. In the present work we employ such a summation over lattice-symmetry equivalent forces. After applying the symmetry operations, these forces correspond to locally inequivalent magnetic configurations

---

and allow one to perform the SSA procedure based on a single magnetic SQS structure. In the PM regime it is typically sufficient to restrict the sum in Eq. 3.1 to completely disordered configurations, since they dominate the partition sum (i.e. the weights  $p_m$ ). Usually about 50-100 magnetic configurations yield converged forces [31]. Note that the treatment of magnetic partially disordered configurations requires advanced sampling techniques, which are beyond the scope of the present manuscript and will be discussed elsewhere [43]. In the present work the magnetic disordered configurations  $m$  are constructed by all 3N Cartesian (positive and negative) displacements for the given SQS super-cell, resulting in 384 magnetic configurations.

For the purpose of comparison, we additionally employed the *conventional* method for computing PM phonons [44], i.e. we allow atomic relaxations in the PM state which results in virtual displacements at T=0 K. The consequences of this approach and the necessity to employ the SSA averaging technique will be discussed later. Also the impact of choosing a different SQS will be discussed. The finite-displacement method implemented in the phonopy [45] combined with VASP was used to calculate the real-space force constants and corresponding phonon properties. The residual forces (background forces) in the unperturbed super cell were subtracted from the force sets of the displaced structures. The summation over lattice symmetry equivalent forces according to the SSA scheme [31] has been carried out by phonopy software [46]. In order to benchmark the direct-force constant method, the NM B1-CrN, FM B1-CrN, AFM B1-CrN and AFM Ortho-CrN real-space force constants were additionally calculated within the density functional perturbation theory framework [47] as implemented in the VASP code. The phonon frequencies were subsequently calculated using the phonopy code. The phonon densities of states (DOS) from both methods (direct force constant and perturbation theory) coincide without any noticeable differences (0.5 meV/atom and 2 meV/atom difference in the free energy evaluated using both methods at 0K and 1000K, respectively). Anharmonic phonon-phonon interactions which can become important close to the melting point [48] are not relevant for the present study. We will show this explicitly in Sec. C by comparing our calculations with the molecular dynamics simulations performed in Ref. [30], which implicitly

include anharmonicity.

When LDA+U or GGA+U is used to treat the strong correlation effects, a small band gap opens for AFM Ortho-CrN and PM B1-CrN. Consequently, the dipole–dipole interactions including properties of the Born effective charge tensor and dielectric tensor, which result in a longitudinal-transversal optical phonon branches (LO-TO) splitting [47], should be taken into account during the phonon calculations. For that purpose the dipole-dipole interactions were calculated from the linear response method within the density functional perturbation theory framework as implemented in VASP at the  $\Gamma$ -point of reciprocal space. The contribution of non-analytical term corrections to the dynamical matrix developed by Wang *et al.* was considered by the following formula [49]:

$$\Phi_{\alpha\beta}^{jk}(M, P) = \phi_{\alpha\beta}^{jk}(M, P) + \frac{1}{N} \frac{4\pi e^2}{V} \frac{[qZ^*(j)]_{\alpha}[qZ^*(k)]_{\beta}}{q\varepsilon_{\infty}q}, \quad (3.2)$$

where  $\phi_{\alpha\beta}^{jk}$  is the contribution from short-range interactions based on super-cell,  $N$  is the number of primitive unit cells in the super cell,  $V$  is the volume of the primitive unit cell,  $q$  is the wave vector,  $\alpha$  and  $\beta$  are the Cartesian axes,  $Z^*(j)$  is the Born effective charge tensor of the  $j^{\text{th}}$  atom in the primitive unit cell, and  $\varepsilon_{\infty}$  is the high frequency static dielectric tensor, i.e., the contribution to the dielectric permittivity tensor from the electronic polarization. In principle the Born effective charge matrix  $Z^*$  should fulfill the symmetries of the underlying crystal, i.e. for the given case  $Z_{\alpha\beta}(i) = 0$  for  $\alpha \neq \beta$  (off-diagonal elements), and  $Z_{\alpha\alpha}(\text{Cr}) = -Z_{\alpha\alpha}(\text{N}) \equiv Z$  (due to charge neutrality [50]). However, due to the broken (magnetic) symmetries of the given magnetic random structure, the Born effective charge matrix elements,  $Z_{\gamma\delta}^{\bar{\sigma}}(j)$ , for each individual magnetic configuration,  $\bar{\sigma}$ , do not oblige these conditions. In the spirit of the SSA we therefore average over the crystal symmetry equivalent matrix elements, i.e.,  $Z_{\alpha\beta}^{\text{sym}}(i) = \sum_{\gamma\delta, j} S_{\alpha\gamma}^{\beta\delta} Z_{\gamma\delta}^{\bar{\sigma}}(j)$ , where  $S_{\alpha\gamma}^{\beta\delta}$  denote the crystal lattice symmetry operations (translation and rotational operations). This summation is equivalent to the summation over different

---

magnetic snapshots (see Eqs. 5 and 6 in [31]). It is similar for the dielectric tensor, i.e.,  $\epsilon_{\alpha\beta}^{\text{sym}} = \sum_{\gamma\delta} S_{\alpha\gamma}^{\beta\delta} \epsilon_{\gamma\delta}^{\sigma}$ , where  $\epsilon \equiv \epsilon_{\alpha\alpha}^{\text{sym}}$  and  $\epsilon_{\alpha\beta}^{\text{sym}} = 0$  for  $\alpha \neq \beta$ . The derived values for  $\epsilon = 15.4/17.3$  and  $Z = 4.1/4.2$  (GGA+U/LDA+U) are in fair agreement with the experimental values of  $22 \pm 2$  and  $4.4 \pm 0.9$  [17], which have been employed in the previous work by Shulumba *et al.* [30].

### 3.2.3 Thermodynamic properties

Once the phonon DOS is obtained, the vibrational energy and its effect on thermal properties can be directly evaluated. In combination with first-principles calculations, the Helmholtz free energy,  $F(V, T)$ , is the most convenient choice for a thermodynamic potential, since it is a natural function of  $V$  and  $T$ :

$$F(V, T) = E_0(V) + F^{\text{el}}(V, T) + F^{\text{vib}}(V, T) + F^{\text{mag}}(V, T), \quad (3.3)$$

where  $E_0(V)$  is the internal energy at 0 K obtained from the equation of state [51],  $F^{\text{el}}(V, T)$  and  $F^{\text{vib}}(V, T)$  are the thermal electronic and lattice contributions to the free energy, respectively. Further details on the *ab initio* calculations of  $F^{\text{el}}(V, T)$  and  $F^{\text{vib}}(V, T)$  are discussed in Ref. [52] and references therein.  $F^{\text{mag}}(V, T)$  is the magnetic free energy which is in the present work considered within the mean-field approximation as [53]:

$$F^{\text{mag}} \approx -k_B T \ln(M(T, V) + 1), \quad (3.4)$$

where  $M(T, V)$  is the magnitude of the local magnetic moment (in units of  $\mu_B$ ) and  $k_B$  is the Boltzmann constant. In this work we used the averaged magnitude of the local magnetic moment,  $M(T=0 \text{ K}, V=V_0)$ , at 0 K at the ground state volume,  $V_0$ , to predict the magnetic entropy. The local magnetic moments derived from the magnetically disordered configurations naturally include the *implicit* temperature-dependent effect of magnetic disorder. Furthermore, our test calculations revealed that the inclusion of the volume dependence has no significant impact on our main results and conclusions, and will be therefore not considered in the following. The

---

inclusion of *explicit* temperature-dependent effects on the local magnetic moments in complex alloys is still in its infancy. Progress on pure elements such as Fe and Ni by means of band structure models [54], dynamical mean field theory [55], and extended Heisenberg models in combination with constrained spin-DFT and CPA [56] provide in this respect promising future routes. The average magnetic moments based on GGA, GGA+U, and LDA+U schemes, which are in the following used in Eq. 3.4, are  $2.48 \mu_B$ ,  $2.90 \mu_B$ , and  $2.83 \mu_B$ , respectively, which agrees well with previous theoretical values [16,21]. Consistent with the SSA treatment of phonons in the paramagnetic state, above mean-field expression does not include magnetic short-range order contributions or non-collinear magnetic structures. It characterizes therefore the scenario of uncorrelated magnetic spin moments. It has been shown earlier [57], that for completely uncorrelated magnetic systems, non-collinear and collinear pictures provide the same thermodynamic descriptions. We therefore adopt the same approach as recently employed in Ref. [30], i.e. Eq. 3.4 above. Nevertheless, short-range order as well as non-collinear structures are likely relevant for the energetics close to the Néel temperature as suggested by recent magnetic cluster expansion techniques [58-60]. Its incorporation would be very valuable but requires techniques beyond the present scope of the paper, such as the magnetic cluster expansion or Quantum Monte Carlo methods (see, e.g., Ref. [53] for a recent overview of the different techniques), and will be therefore left for a future contribution.

### 3.2.4 Experimental details

Since no experimental study has been devoted so far to the lattice thermal expansion coefficient,  $\alpha$ , this property has been measured within the present work. A single-phase face-centered cubic CrN thin film was deposited on Si (100) substrates ( $7 \times 21 \text{ mm}^2$ ) using reactive magnetron sputtering. The deposition was carried out at a deposition temperature of 743 K in an Ar and N<sub>2</sub> gas atmosphere of a total pressure of 0.4 Pa and a constant Ar/N<sub>2</sub> flow ratio of 2/3. A target power of 250 W and a Cr target (purity 99.9 %) were used. During the deposition, a bias potential of  $-70 \text{ V}$  was applied to the substrates to ensure dense film morphology. The film thickness was measured using cross-sectional scanning electron microscopy. The biaxial stress

in CrN was recorded as a function of temperature using the wafer- curvature method [61]. The wafer-curvature system was operating with an array of parallel laser beams and a position sensitive charge-coupled device detector. The sample was heated by a ceramic heating plate with a constant heating rate of 5 K/min from room temperature to 518 K under vacuum conditions of  $\leq 10^{-4}$  mbar. The maximum temperature was chosen to be clearly below the deposition temperature to avoid thermally activated processes in the film (e.g. recovery of deposition-induced defects) and the substrate and thus to guarantee pure thermoelastic behavior. The film stress was deduced from the sample curvature  $1/R$  according to:

$$\sigma = \frac{Mh^2}{6Rt_f} \quad (3.5)$$

with  $M \sim 180$  GPa being the biaxial modulus of the substrate,  $h = 380 \mu\text{m}$  the substrate and  $t_f = 1.50 \mu\text{m}$  the film thicknesses. Due to the mismatch in the coefficients of thermal expansion of CrN and Si, the temperature change results in the formation of thermal stresses in the film. When the elastic moduli are taken as constants in the given temperature range, the linear thermal expansion coefficient,  $\alpha$ , of CrN thin film is related to that of substrate (Si) as:

$$\alpha(T) = \alpha_{\text{si}(001)}(T) + \frac{1 - \nu_{\text{CrN}}}{E_{\text{CrN}}} \cdot \frac{d\sigma}{dT} \quad (3.6)$$

with  $E_{\text{CrN}}=330$  GPa,  $\nu_{\text{CrN}}=0.22$  [62,63] and the thermal expansion coefficient of substrate (Si) is expressed as [64]:

$$\alpha_{\text{si}(001)}(T) = (3.725[1 - \exp(-5.88 \times 10^{-3} [T - 124] + 5.548 \times 10^{-4} T)] \times 10^{-6} (T \text{ in K}). \quad (3.7)$$

### 3.3 Results and Discussion

#### 3.3.1 Elastic constants and mechanical stability

The elastic constants of the different studied structures as calculated by the GGA, GGA+U, and LDA+U schemes are listed in Table 3.1.

Table 3.1:  $T=0$  K elastic constants in GPa of CrN within the framework of GGA, GGA+U, and LDA+U methods including a comparison with experimental values. It can be seen that most of the elastic constants derived from GGA and GGA+U are smaller than those obtained from the LDA+U scheme. This is consistent with the fact that GGA frequently overestimates lattice parameters leading to an underestimation of binding energies, elastic properties, and phonon frequencies for most materials [65]. In contrast, LDA (or LDA+U) tends to overestimate binding as expressed by smaller lattice parameters, and higher elastic constants and phonon frequencies when compared with experimental or GGA and GGA+U values. A comparison with the limited available experimental data reveals good agreement for the  $C_{11}$  component (in particular for GGA+U), while  $C_{12}$  and  $C_{44}$  seem to be overestimated by all the LDA+U, GGA and GGA+U theoretical predictions. However, it might be that the substantially too low experimental  $C_{ij}$  constants are a consequence of the fact that the measurements have been performed on a polycrystalline sample at room temperature, i.e., the measured elastic constants may be influenced by soft grain boundaries [63].

Structure		$C_{11}$	$C_{22}$	$C_{33}$	$C_{12}$	$C_{13}$	$C_{23}$	$C_{44}$	$C_{55}$	$C_{66}$
	GGA	580			210			8		
NM B1	GGA+U	477			266			-120		
	LDA+U	641			260			-59		
	GGA	348			117			74		
FM B1	GGA+U	508			108			156		
	LDA+U	589			128			162		
	GGA	535	535	567	126	86	86	150	94	94
AFM B1	GGA+U	555	555	389	98	66	66	166	129	129
	LDA+U	696	696	722	113	76	76	174	124	124

---

	GGA	516			115			116		
	GGA+U	538			88			143		
PM B1	LDA+U	649			99			145		
	Exp. [62,63]	540			27			88		
	GGA	439	529	495	195	110	114	221	125	103
AFM Ortho	GGA+U	444	524	497	169	84	92	223	151	137
	LDA+U	503	580	626	228	87	102	275	155	137

---

The mechanical stability of any crystal requires the strain energy to be positive, which implies that the whole set of elastic constants,  $C_{ij}$ , must satisfy the Born-Huang stability criterion [32]. Using this requirement Table 3.1 shows that CrN is mechanically stable within the GGA scheme for all magnetic and structural configurations studied here in consistency with previous results [22,23,26]. In contrast, we observe that  $C_{44}$  derived from the LDA+U and GGA+U schemes suggest NM B1-CrN to be mechanically unstable ( $C_{44} < 0$ ). This result underlines the importance of strong correlation effects, which were not considered in previous elastic constant calculations using standard LDA or GGA approaches. Finally, we observe AFM B1-CrN to show a small tetragonal distortion, which is reflected in the number of nonequivalent elastic constants:  $C_{11}$ ,  $C_{12}$ ,  $C_{13}$ ,  $C_{33}$ ,  $C_{44}$  and  $C_{66}$  in agreement with previous results [22].

### 3.3.2 Dynamical stability

As discussed above, a necessary condition for a structure to be dynamically stable is that it is stable against all possible small perturbations of its atomic structure, i.e., that all phonon frequencies must be real. The GGA, GGA+U, and LDA+U phonon spectra of NM B1-CrN are presented in Fig.3.2 (a).

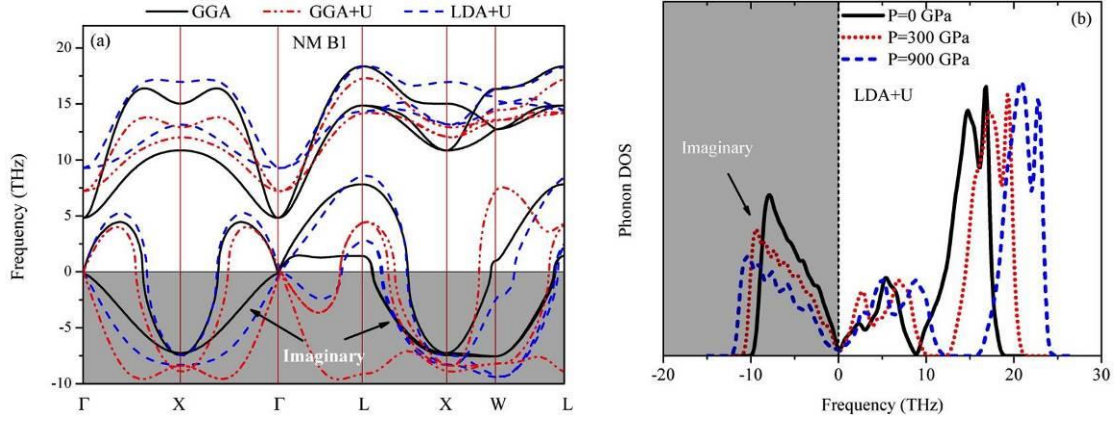
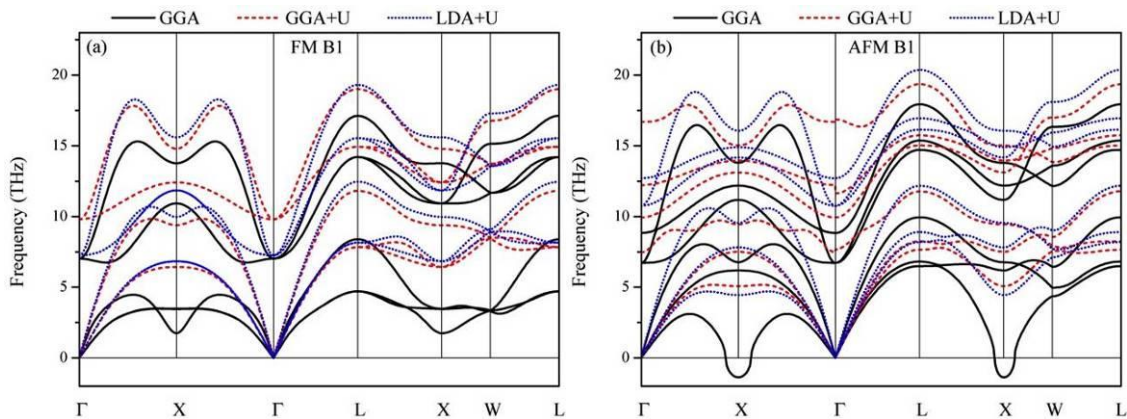


Figure 3.2: (a) Phonon spectra of NM B1-CrN calculated using GGA, GGA+U, and LDA+U, and (b) phonon DOS as a function of pressure for NM B1-CrN from the LDA+U scheme. The gray shaded region highlights imaginary frequencies.

Imaginary acoustic branches at the  $X$  and  $W$ -points of the Brillouin zone suggest an internal instability of NM B1-CrN. These phonon anomalies are due to the high electron DOS at the Fermi level of NM B1-CrN [13], which causes the existence of soft phonon modes at these points. We evaluated the phonon density of states (DOS) of NM B1-CrN for several pressures up to 900 GPa to check whether applying external pressure can eliminate these imaginary phonons. For the sake of clarity, only the representative LDA+U results are presented in Fig.3.2 (b), yielding the following tendency: NM B1-CrN is dynamically unstable even under high pressures, indicating the NM B1-CrN cannot be stabilized by high pressure.

In order to check the phase stability of CrN for various magnetic states, the phonon spectra of CrN from GGA, GGA+U, and LDA+U with ordered magnetic states are presented in Fig.3.3.



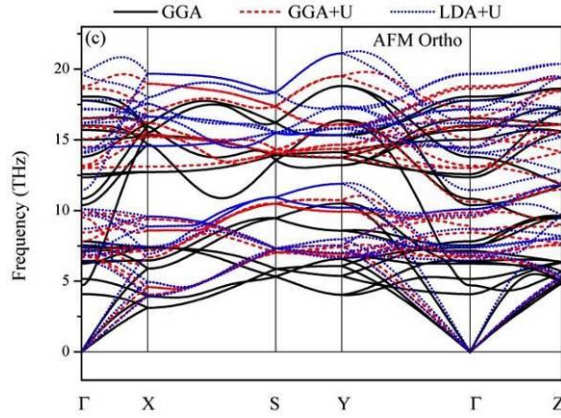


Figure 3.3: Phonon spectra of (a) FM B1-CrN, (b) AFM B1-CrN and (c) AFM Ortho-CrN calculated using the GGA, GGA+U and LDA+U schemes.

The comparison of the phonon spectra of FM B1-CrN, AFM B1-CrN and AFM Ortho-CrN from GGA, and GGA+U or LDA+U reveals that the phonon spectra are significantly shifted to higher frequencies for the latter approximations. The GGA and GGA+U based phonon frequencies are always lower than those derived from the LDA+U scheme, a trend already reflected by the softer elastic constants when GGA or GGA+U is used. For FM and AFM B1-CrN, when no U-correction is used, a softening tendency for the phonon branch around the X-point is observed, and for AFM B1-CrN phonon frequencies even decrease to negative values. The dynamical instability, not observed via the elastic constants calculations, indicates once more the necessity of explicit phonon calculations for the stability analysis. This phonon anomaly observed for the GGA calculations originates from the high electron DOS at the Fermi level. When the on-site Coulomb repulsion U in the DFT+U scheme is switched on, the electron density of states at Fermi level significantly decreases for the FM B1-CrN although no gap opens [15]. Here, one should note that despite the fact that the DFT+U approximation does not result in a gap opening at the Fermi level for NM- and FM B1-CrN, as shown in Refs. [13,15], it significantly increases the stability of FM and AFM B1-CrN as measured by phonon frequencies around X-point. No imaginary frequencies in the phonon dispersion curves are observed independent of whether the GGA+U or LDA+U scheme is used, implying that FM B1-CrN, AFM B1-CrN and AFM Ortho-CrN are all dynamically stable, and represent hence potential (meta)stable phases.

In contrast to the ordered magnetic states of FM B1-CrN, AFM B1-CrN and AFM Ortho-CrN, the magnetic state in PM B1-CrN is disordered. As a first step we allow for atomic relaxations at 0 K. Since at finite temperatures the magnetic fluctuations are usually faster compared to the atomic motion, these displacements can be considered as artificial. In order to test the effect of such artificial static displacements, the atomic positions are fixed to the ideal B1 sites and cell shape remains cubic (we refer to this structure as “unrelaxed” hereafter). The phonon DOS corresponding to unrelaxed and fully relaxed SQS are presented in Fig.3.4 (a).

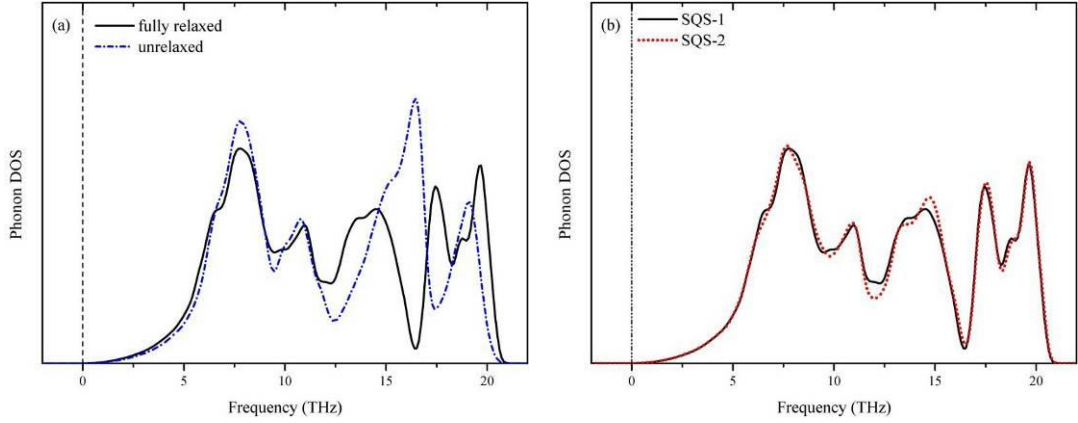


Figure 3.4: Phonon DOS’s from the LDA+U scheme (a) for fully relaxed and unrelaxed SQS, (b) for two SQSs with different SRO parameters.

Clearly, the phonon DOS of the unrelaxed SQS exhibits some different features than that of the fully relaxed one, which means that the artificial static displacements have some impact on the phonon calculations. A closer inspection of the phonon dispersion of the unrelaxed structure reveals some imaginary phonon modes at the  $\Gamma$  point. In order to elucidate if these imaginary frequencies are physical, we employ in the following the recently developed SSA method, Eq. 3.1, to compute the phonon frequencies in the paramagnetic regime.

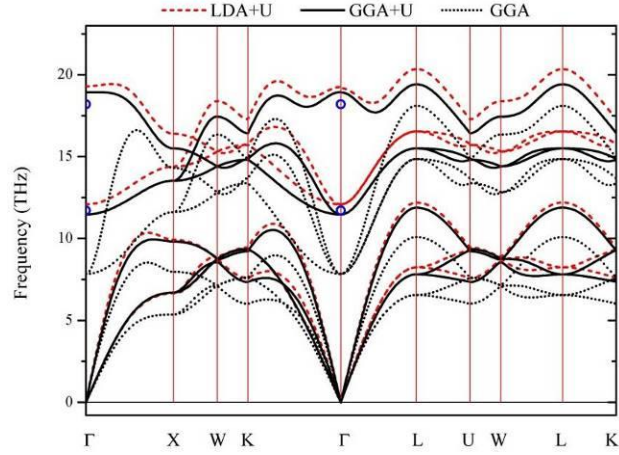


FIG.3.5. Phonon spectra of PM B1-CrN simulated with a 64-atom SQS from the GGA, GGA+U and LDA+U schemes in combination with SSA approach, together with experiments at the  $\Gamma$  point from Raman and infrared measurements (open circles [17] ).

In fact, no imaginary phonon frequencies are obtained (see the red dashed line in Fig.3.5) revealing the applicability of the method and the fact that the imaginary phonon modes along the acoustic dispersions are indeed caused by the artificial  $T=0$  K relaxations. In order to further analyze the impact of artificial  $T=0$  K relaxations on the specific SQS structure, we have performed similar calculations for a second SQS with a different spin arrangement. Figure 3.4b shows that the phonon DOS's for the two SQS almost fully coincide, suggesting that a particular spin arrangement and consequently a specific spin-induced relaxation of atoms at  $T=0$  K in the SQS of PM B1-CrN does not significantly affect the phonon DOS and hence thermodynamic properties. Since the SSA computed phonon DOS does not show any imaginary frequencies and does not require any (unphysical)  $T=0$  K relaxations, we will proceed with the SSA obtained phonon DOS and thermodynamic properties for the following thermodynamic analysis. As discussed above, super cell convergence tests for NM and AFM variants have revealed that a  $2 \times 2 \times 2$  super-cell is sufficient for an accurate description within the considered temperature range. This is in agreement with the findings of Shulumba *et al.* [30], who reported convergence with respect to the super cell size for PM B1-CrN for a super cell with 64 atoms ( $2 \times 2 \times 2$ ), which we will employ in the following.

Figure 3.5 presents the phonon spectra of PM B1-CrN derived from GGA, GGA+U and

LDA+U schemes employing the SSA method, and in comparison with available experimental data (open circles [17]) at the  $\Gamma$  point. It demonstrates that the transverse branches derived from DFT+U are significantly shifted to higher values and the LO-TO splitting happens at the  $\Gamma$  point, when comparing to the result from GGA scheme. The obtained dispersion from DFT+U is in excellent agreement with experimental data (blue circles), especially the results derived from the GGA+U scheme are very close to experimental data. The accurately predicted transverse and longitudinal optical phonon frequencies at the  $\Gamma$  point further validate the reliability of the SSA scheme. The phonon spectra derived from GGA, GGA+U, and LDA+U in combination with the SSA scheme confirm that PM B1-CrN is dynamically stable.

### 3.3.3 Thermodynamic stability and thermodynamic properties of CrN

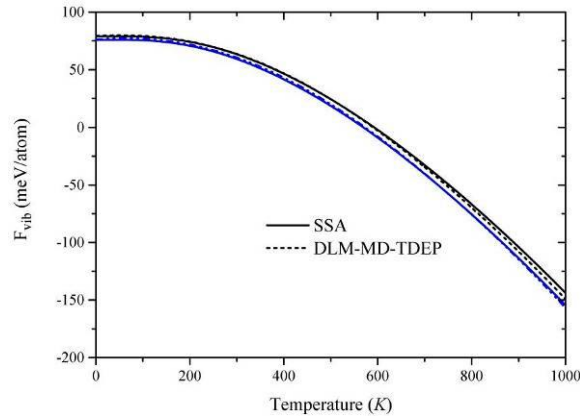


Figure 3.6: Comparison of the vibrational free energies for AFM Ortho-CrN (blue lines) and PM B1-CrN (black lines) under the framework of LDA+U. The solid lines denote the results from SSA approach in the present work and dotted lines denote DLM-MD-TDEP method [30].

The Gibbs free energy has been evaluated according to the treatment described in Sec. C employing in particular the SSA method for the PM phases. Due to the opening of a small gap in AFM Ortho-CrN and PM B1-CrN as obtained from GGA+U and LDA+U [18], the thermal electronic contribution  $F^{\text{el}}(V, T)$  to the Helmholtz free energy can be ignored for AFM Ortho-CrN and PM B1-CrN.

Firstly, we compare the SSA results for the Gibbs energies to previous results from the

---

DLM-MD-TDEP method [30] to verify the reliability of our method and also to check the influence of anharmonic effects on the vibrational free energy. The comparison between the present work and the results from DLM-MD-TDEP method [30] is presented in Fig.3.6.

As the latter method is based on MD simulations, anharmonic contributions are implicitly included. This allows us to evaluate the importance of anharmonic effects for the considered temperature regime. Figure 3.6 demonstrates that the vibrational free energies of PM B1-CrN from both methods (SSA and DLM-MD-TDEP) fully coincide with each other and that there is no noticeable difference even at high temperatures. The largest deviation of about 5 meV/atom is observed for AFM Ortho-CrN at 1000 K. Keeping in mind that the phase transition under consideration occurs at room temperature, we obtain an excellent agreement with the previous work in the relevant temperature regime revealing that anharmonic contributions are not decisive for the considered transition.

Next we concentrate on the impact of the xc-functional. The differences of harmonic vibrational free energies as a function of temperature between AFM Ortho-CrN and PM B1-CrN in the GGA, GGA+U and LDA+U schemes are presented in Fig.3.7 (a). For all considered scenarios, the vibrational contribution to the free energy favors the PM B1-CrN phase. This contribution becomes smaller when the strong correlation effects are taken into account by using Hubbard Coulomb term U.

We now include the magnetic entropy, Eq. 3.4, into our free energy computations. The results including both, vibrational as well as the magnetic entropy terms evaluated using GGA, GGA+U and LDA+U schemes, are presented in Fig.3.7b as a function of temperature for AFM Ortho-CrN and PM B1-CrN phases. The critical temperature for the structural transition between AFM Ortho and PM B1 CrN is  $T_s=428$  K for GGA,  $T_s=300$  K for GGA+U, and  $T_s=370$  K for the LDA+U scheme. The excellent agreement of the latter with the previous theoretical results [30] reveals once more the reliability of our SSA approach. A particularly important conclusion is that the GGA+U value turns out to be significantly closer to the experimental value compared to the previous LDA+U estimations. This improvement of

GGA+U compared to the LDA+U data is remarkable and of similar magnitude and importance as the inclusion of vibrational contributions [22,36].

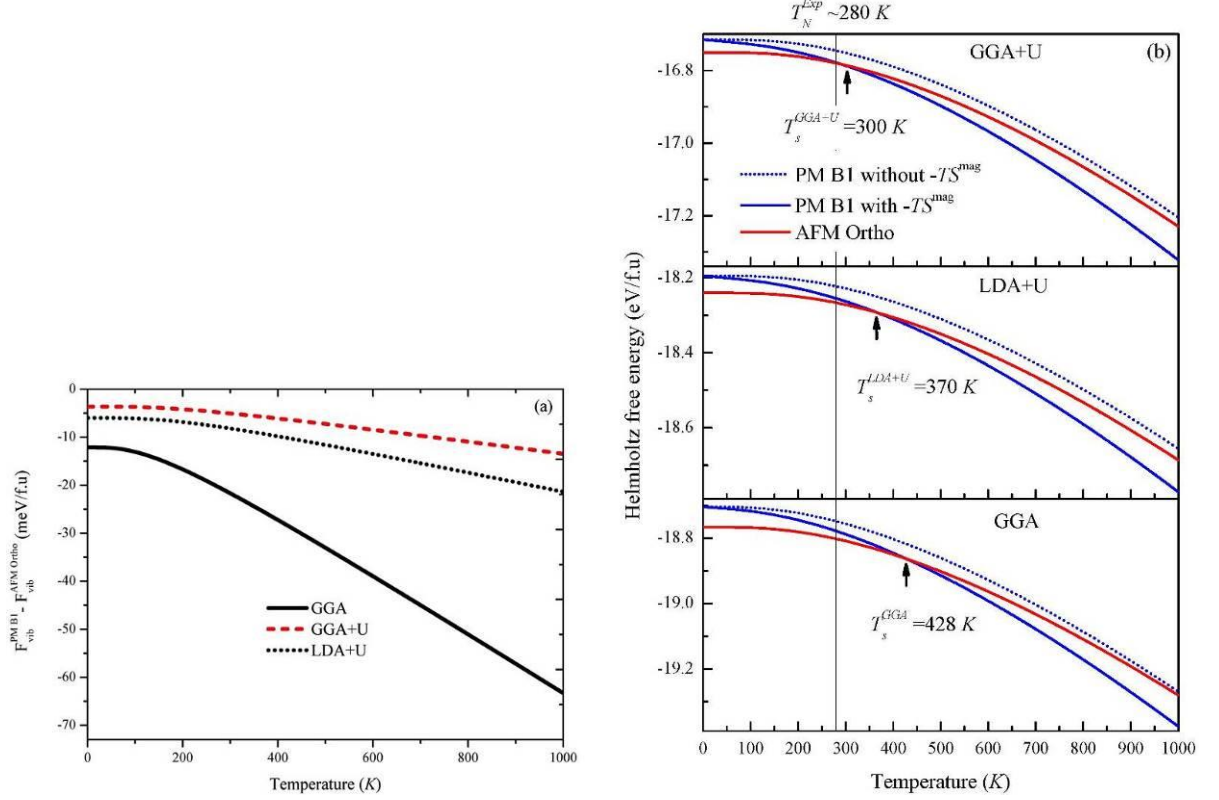


Figure 3.7 (a) The differences of vibrational free energy between AFM Ortho-CrN and PM B1-CrN in the GGA, GGA+U and LDA+U schemes, and (b) calculated phase transition temperature from Helmholtz free energies of AFM Ortho-CrN and PM B1-CrN by taking lattice vibrational and magnetic contributions into account under the framework of GGA, GGA+U and LDA+U schemes. The dotted lines denote the Helmholtz free energies of PM B1-CrN without magnetic contributions.

The inclusion of vibrational free energy contributions is considerable and shifts the transition temperature, e.g. for GGA, by almost 500 K [16]. The inclusion of magnetic entropy turns out to be similarly important. To elucidate the impact of magnetic contributions, we included in Fig.3.7 (b) also the Gibbs free energy curves *without* the magnetic entropy term  $S^{\text{mag}}$  in Eq. 3.4 (dotted lines). Consequently, AFM Ortho-CrN becomes energetically preferred over the PM B1-CrN phase in the whole investigated temperature range. In agreement with previous works

---

[16,30] we can therefore conclude that both, magnetic and vibrational contributions are equally important to accurately predict the transition temperature. The remaining difference between predicted and experimental values for the phase transition temperature may be related to the approximate treatment of magnetism (neglected non-collinear magnetic configurations, magnetic entropy extracted from mean-field approximation) or to the inherent DFT approximation, i.e. the treatment of the xc-functional.

In order to shed some light on the impact of U-J parameter for the phase transition, we briefly discuss the expected impact of choosing an even larger U-J parameter. In Fig.3.8 the impact of the U-parameter on the phase transition temperature is presented. Here, the transition temperature is evaluated based on the total and magnetic energy contributions. The just discussed vibrational contributions for the already performed calculations, which is the most computationally demanding part, are indicated by the arrows, i.e. at U-J=0 and U-J=3 eV. As can be seen from Fig.3.8, the impact of larger U-values becomes less significant. This can be traced back to compensating total energy and magnetic entropy contributions. Changing the U-parameter, e.g., from 3 eV to 4 eV slightly shifts the theoretical value by ~44 K, i.e. even closer to the experimental one. In Fig.3.7a it is shown that an increase of the U-parameter (from 0 to 3 eV) reduces the vibrational contribution to the phase transition temperature, which is also indicated by the arrows in Fig.3.8. This suggests that the vibrational contribution for U-J=4 eV, which is not explicitly evaluated here due to the heavy additional computational costs (discussed above), will likely further decrease the phase transition temperature, although presumably to much less extend. Eventually, only a *full* U-J=4 eV calculation taking into account *all* contributions consistently (including vibrations) would be necessary to confirm this assumption.

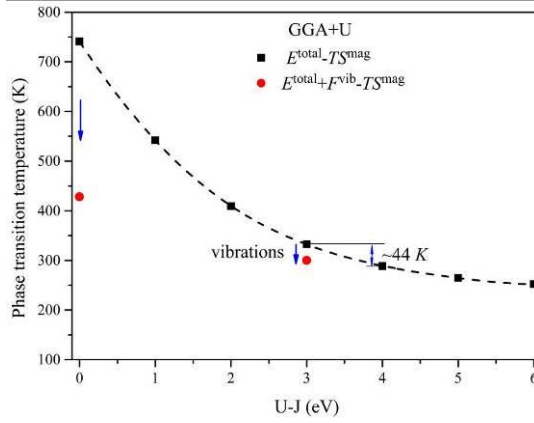


Figure 3.8: Impact on phase transition temperature within GGA+U for different U parameters.

The phase transition from AFM Ortho-CrN to PM B1-CrN induced by temperature can be alternatively triggered by pressure. In order to investigate the pressure effect on the phase transition, the Gibbs energy is computed via the Legendre transformation as

$$G(p,T) = F(V(p),T) + pV(p,T) \quad (3.8)$$

where  $F$  is the Helmholtz free energy, Eq. 3.3, evaluated within the framework of the quasi-harmonic approach at several volumes including the magnetic entropy contributions from Eq. 3.4 for PM B1-CrN.  $p$  is the pressure and  $V(p,T)$  is the volume as a function of pressure and temperature. Using the Gibbs energies of AFM Ortho-CrN and PM B1-CrN based on the GGA+U and LDA+U schemes, the  $p$ - $T$  phase diagram was derived (Fig. 3.9).

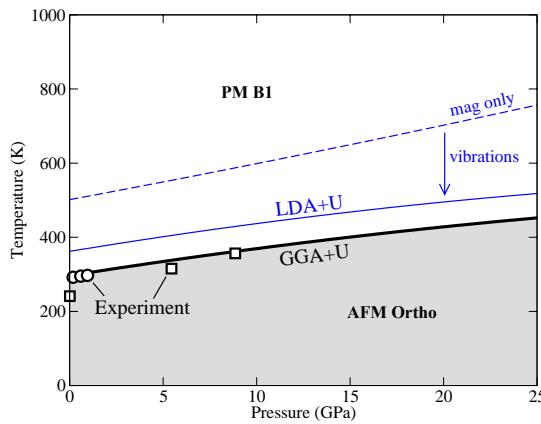


Figure 3.9: Calculated pressure-temperature phase diagram of CrN based on the GGA+U (black line) and LDA+U (blue lines) schemes compared to experiment (open circles [7] and

squares [10]). The solid lines represent the phase diagram based on the relevant spectrum of excitations: total energy, vibrational and magnetic entropy contributions. For LDA+U, the dashed line shows the phase diagram if only the total energy and magnetic excitations are included to emphasize the impact of vibrational entropy.

The transition temperature increases with pressure in agreement with experimental and theoretical results reported in literature. The transition temperature at  $p=0$  GPa obtained from experiment [1,7,10] varies from 200 K to 287 K, showing an uncertainty of up to 87 K. Within this error-bar, our theoretical predictions based on the GGA+U method are in excellent agreement with the experimental work and yielding a significant improvement as compared with the previously reported theoretical results. It should be noted that the transition temperatures at  $p=0$  GPa are approximately 10 K lower than the results in Fig.3.7. This is due to the fact that the free energy in Eq. 3.3 is evaluated within the quasi-harmonic approximation, while the results presented in Fig.3.7 are obtained from the harmonic approach. This implies that the quasi-harmonic contribution (i.e., caused by thermal expansion) is not as important as for example the strong correlation effect or the magnetic entropy contribution, within the considered temperature-pressure regime.

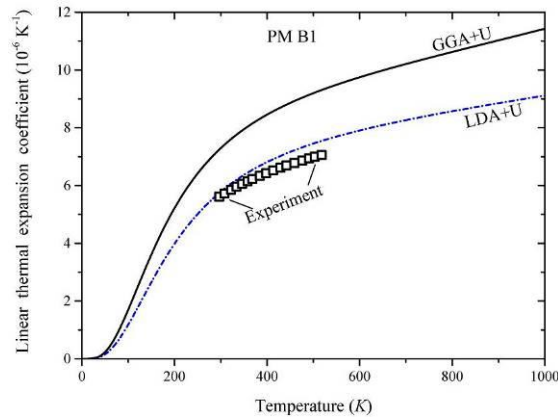


Figure 3.10: Linear thermal expansion coefficient,  $\alpha(T)$ , of PM B1-CrN computed within the GGA+U (black solid line) and LDA+U (blue dashed line) schemes compared to experimental data (open squares) as obtained in the present work.

On the other hand, thermal expansion is a key thermodynamic property of PM B1-CrN when it

is applied as a high temperature coating material. If compared to experiment, the derivative of the linear thermal expansion coefficient,  $\alpha(T)$ , provides an even more sensitive measurement of the accuracy achievable by the theoretical predictions. The calculated  $\alpha(T)$  of PM B1-CrN is compared to our experimental data in Fig.3.10. The results are in good agreement around room temperature, and the discrepancy increases with raising temperature. It was recently demonstrated that  $\alpha(T)$  of CrN strongly depends on the grains size [66]. Depending on the thin film microstructure,  $\alpha(T)$  varies in the range of  $6.7 \times 10^{-6}/\text{K}$  and  $9.8 \times 10^{-6}/\text{K}$ , which for this material somewhat complicates a distinct comparison with our predictions. Considering these complications, the overall agreement with experiment is very reasonable.

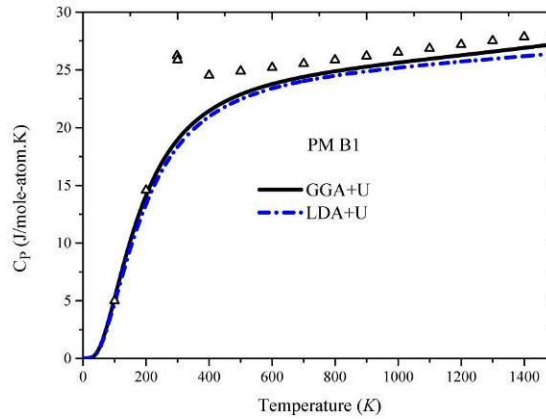


Figure 3.11: Heat capacities of PM B1-CrN in the GGA+U (black solid line) and LDA+U (blue dashed line) schemes compared to experimental values (open triangles [67]).

Finally, in Fig.3.11 we plot the specific heat capacity,  $C_p(T)$ , at constant (ambient) pressure as a function of temperature predicted from our GGA+U and LDA+U calculations, together with available experimental data from literature [67]. The GGA+U values are slightly closer to the experimental data. This is consistent with the findings for the phase transition temperature discussed above; however, the differences between LDA+U and GGA+U are only minor. The literature data exhibit a peak near the phase transition temperature ( $\sim 280$  K), due to the Néel transition, which has not been accounted for in the present study. This peak originates from the magnetic phase transition and can be resolved only when the magnetic contribution is exactly evaluated by, for example the Heisenberg model for spin interactions [68]. Nevertheless, our predictions are reasonably accurate from 0K to about 200K and also above 600K.

---

### 3.4 Conclusions

In this chapter, the phase stability of different structural and magnetic configurations of stoichiometric CrN is studied systematically by first-principles calculations based on the GGA, GGA+U, and LDA+U schemes. In combination with our recently developed SSA procedure, the phonon contributions in paramagnetic materials are computed. A comparison of the three exchange-correlation approximations demonstrates, that strong correlation effects have a significant impact on the mechanical and phase stability of CrN. The elastic constants and phonon spectra show that the non-magnetic B1-CrN phase is dynamically unstable even under high pressures, due to the high electron density of states at Fermi level. The (meta)stability of the ferromagnetic and antiferromagnetic B1-CrN phase is significantly improved when strong correlation effects are considered using the DFT+U approach.

Including the vibrational, electronic and magnetic free energy contributions, the results of our LDA+U-SSA based approach agree well with previous LDA+U-MD simulations. By performing for the first time finite-temperature GGA+U simulations for CrN we show that the treatment of the xc-functional, i.e. GGA+U vs. LDA+U, is decisive to predict accurate phase transition temperatures in CrN. In particular we find that GGA+U significantly improves previous LDA+U predictions. The phase transition between AFM Ortho-CrN and the paramagnetic B1-CrN phase is predicted to be 293 K at ambient pressure being in excellent agreement with the experimental value of 200-287 K. The impact of the xc-functional is similar in magnitude to the impact of vibrational contributions to the phase stability. The linear thermal expansion coefficient,  $\alpha(T)$ , and the heat capacity,  $C_p$ , of PM B1-CrN as a function of temperature is obtained from experimental measurements and *ab initio* calculations. The comparison between the experimental results and predictions for these thermodynamic properties reveals good agreement and further confirms the reliability of our theoretical method.

---

# References

- [1] L. M. Corliss, N. Elliott, and J. M. Hastings, *Phys. Rev.* **117**, 929 (1960).
- [2] B. Navinšek and P. Panjan, *Surf. Coat. Technol.* **97**, 182 (1997).
- [3] A. Ney, R. Rajaram, S. S. P. Parkin, T. Kammermeier, and S. Dhar, *Appl. Phys. Lett.* **89**, 112504 (2006).
- [4] K. Inumaru, K. Koyama, N. Imo-Oka, and S. Yamanaka, *Phys. Rev. B* **75**, 054416 (2007).
- [5] P. H. Mayrhofer, F. Rovere, M. Moser, C. Strondl, and R. Tietema, *Scripta Mater.* **57**, 249 (2007).
- [6] C. X. Quintela, F. Rivadulla, and J. Rivas, *Appl. Phys. Lett.* **94**, 152103 (2009).
- [7] F. Rivadulla *et al.*, *Nat. Mater.* **8**, 947 (2009).
- [8] X. Y. Zhang, J. S. Chawla, B. M. Howe, and D. Gall, *Phys. Rev. B* **83**, 165205 (2011).
- [9] M. Chen, S. Wang, J. Zhang, D. He, and Y. Zhao, *J Chem. Eur. J* **18**, 15459 (2012).
- [10] S. Wang *et al.*, *Phys. Rev. B* **86**, 064111 (2012).
- [11] Z. Zhang, H. Li, R. Daniel, C. Mitterer, and G. Dehm, *Phys. Rev. B* **87**, 014104 (2013).
- [12] D. Gall, C. S. Shin, R. T. Haasch, I. Petrov, and J. E. Greene, *J. Appl. Phys.* **91**, 5882 (2002).
- [13] A. Filippetti, W. E. Pickett, and B. M. Klein, *Phys. Rev. B* **59**, 7043 (1999).
- [14] A. Filippetti and N. A. Hill, *Phys. Rev. Lett.* **85**, 5166 (2000).
- [15] A. Herwadkar and W. R. L. Lambrecht, *Phys. Rev. B* **79**, 035125 (2009).
- [16] B. Alling, T. Marten, and I. A. Abrikosov, *Phys. Rev. B* **82**, 184430 (2010).
- [17] X. Y. Zhang and D. Gall, *Phys. Rev. B* **82**, 045116 (2010).
- [18] A. S. Botana, F. Tran, V. Pardo, D. Baldomir, and P. Blaha, *Phys. Rev. B* **85**, 235118 (2012).
- [19] A. S. Botana, V. Pardo, D. Baldomir, and P. Blaha, *Phys. Rev. B* **87**, 075114 (2013).
- [20] A. Lindmaa, R. Liz árraga, E. Holmström, I. A. Abrikosov, and B. Alling, *Phys. Rev. B* **88**, 054414 (2013).
- [21] B. Alling, T. Marten, and I. A. Abrikosov, *Nat. Mater.* **9**, 283 (2010).
- [22] V. Antonov and I. Iordanova, in *AIP Conference Proceedings* 2010), pp. 1149.

- 
- [23] Y. Liang, X. Yuan, and W. Zhang, *Solid State Commun.* **150**, 2045 (2010).
- [24] H. Lin and Z. Zeng, *Chin. Phys. B* **20**, 077102 (2011).
- [25] M. G. Brik and C. G. Ma, *Comput. Mater. Sci.* **51**, 380 (2012).
- [26] Z. Y. Jiao, Y. J. Niu, S. H. Ma, and X. F. Huang, *Mod. Phys. Lett. B* **27**, 1350158 (2013).
- [27] C. G. Shull, W. A. Strauser, and E. O. Wollan, *Phys. Rev.* **83**, 333 (1951).
- [28] S. H. Wei, L. G. Ferreira, J. E. Bernard, and A. Zunger, *Phys. Rev. B* **42**, 9622 (1990).
- [29] A. Van de Walle and G. Ceder, *Rev. Mod. Phys.* **74**, 11 (2002).
- [30] N. Shulumba, B. Alling, O. Hellman, E. Mozafari, P. Steneteg, M. Odín, and I. A. Abrikosov, *Phys. Rev. B* **89**, 174108 (2014).
- [31] F. Körmann, A. Dick, B. Grabowski, T. Hickel, and J. Neugebauer, *Phys. Rev. B* **85**, 125104 (2012).
- [32] M. Born and K. Huang, *Dynamical theory of crystal lattices* (Clarendon Press Oxford, 1954).
- [33] D. M. Clatterbuck, C. R. Krenn, M. L. Cohen, and J. W. Morris, Jr., *Phys. Rev. Lett.* **91**, 135501 (2003).
- [34] L. Zhou, D. Holec, and P. H. Mayrhofer, *J. Appl. Phys.* **113**, 043511 (2013).
- [35] G. Kresse and J. Hafner, *Phys. Rev. B* **47**, 558 (1993).
- [36] G. Kresse and J. Furthmüller, *Phys. Rev. B* **54**, 11169 (1996).
- [37] G. Kresse and D. Joubert, *Phys. Rev. B* **59**, 1758 (1999).
- [38] V. I. Anisimov, J. Zaanen, and O. K. Andersen, *Phys. Rev. B* **44**, 943 (1991).
- [39] S. L. Dudarev, G. A. Botton, S. Y. Savrasov, C. J. Humphreys, and A. P. Sutton, *Phys. Rev. B* **57**, 1505 (1998).
- [40] J. P. Perdew, K. Burke, and M. Ernzerhof, *Phys. Rev. Lett.* **77**, 3865 (1996).
- [41] H. J. Monkhorst and J. D. Pack, *Phys. Rev. B* **13**, 5188 (1976).
- [42] F. Körmann, B. Grabowski, P. Söderlind, M. Palumbo, S. G. Fries, T. Hickel, and J. Neugebauer, *J. Phys.: Condens. Matter* **25**, 425401 (2013).
- [43] F. Körmann, B. Grabowski, Dutta, T. Hickel, Mauger, Fultz, and J. Neugebauer, *Phys. Rev. Lett.* **113**, 165503 (2014).

- 
- [44] K. Parlinski, Z. Q. Li, and Y. Kawazoe, *Phys. Rev. Lett.* **78**, 4063 (1997).
- [45] A. Togo, F. Oba, and I. Tanaka, *Phys. Rev. B* **78**, 134106 (2008).
- [46] Y. Ikeda, A. Seko, A. Togo, I. Tanaka, *Phys. Rev. B* **90**, 134106 (2014).
- [47] S. Baroni, S. de Gironcoli, A. Dal Corso, and P. Giannozzi, *Rev. Mod. Phys.* **73**, 515 (2001).
- [48] B. Grabowski, L. Ismer, T. Hickel, and J. Neugebauer, *Phys. Rev. B* **79**, 134106 (2009).
- [49] Y. Wang, J. J. Wang, W. Y. Wang, Z. G. Mei, S. L. Shang, L. Q. Chen, and Z. K. Liu, *J. Phys.: Condens. Matter* **22**, 202201 (2010).
- [50] P. Vogl, *Journal of Physics C: Solid State Physics* **11**, 251 (1978).
- [51] F. Birch, *Phys. Rev.* **71**, 809 (1947).
- [52] B. Grabowski, P. Söderlind, T. Hickel, and J. Neugebauer, *Phys. Rev. B* **84**, 214107 (2011).
- [53] F. Körmann, A. A. H. Breidi, S. L. Dudarev, N. Dupin, G. Ghosh, T. Hickel, P. Korzhavyi, J. A. Muñoz, and I. Ohnuma, *Phys. Status Solidi (b)* **251**, 53 (2014).
- [54] W. Nolting, W. Borgiel, V. Dose, and T. Fauster, *Phys. Rev. B* **40**, 5015 (1989).
- [55] A. I. Lichtenstein, M. I. Katsnelson, and G. Kotliar, *Phys. Rev. Lett.* **87**, 067205 (2001).
- [56] A. V. Ruban, S. Khmelevskiy, P. Mohn, and B. Johansson, *Phys. Rev. B* **75**, 054402 (2007).
- [57] B. L. Gyorffy, A. J. Pindor, J. Staunton, G. M. Stocks, and H. Winter, *J. Phys. F* **15**, 1337 (1985).
- [58] S. L. Dudarev, *Annu. Rev. Mater. Res.* **43**, 35 (2013).
- [59] M. Y. Lavrentiev, D. Nguyen-Manh, and S. L. Dudarev, *Phys. Rev. B* **81**, 184202 (2010).
- [60] M. Y. Lavrentiev, R. Soulaïrol, C.-C. Fu, D. Nguyen-Manh, and S. L. Dudarev, *Phys. Rev. B* **84**, 144203 (2011).
- [61] G. C. A. M. Janssen, M. M. Abdalla, F. van Keulen, B. R. Pujada, and B. van Venrooy, *Thin Solid Films* **517**, 1858 (2009).
- [62] J. Almer, U. Lienert, R. L. Peng, C. Schlauer, and M. Odén, *J. Appl. Phys.* **94**, 697 (2003).
- [63] K. J. Martinschitz, R. Daniel, C. Mitterer, and J. Keckes, *J. Appl. Crystallogr.* **42**, 416

---

(2009).

[64] M. O, *Semiconductors: Data Handbook* (2004).

[65] B. Grabowski, T. Hickel, and J. Neugebauer, *Phys. Rev. B* **76**, 024309 (2007).

[66] R. Daniel, D. Holec, M. Bartosik, J. Keckes, and C. Mitterer, *Acta Mater.* **59**, 6631 (2011).

[67] M. W. Chase, J. Davies, C. A. Downey, J. J.R., D. J. Frurip, R. A. McDonald, and A. N. Syverud, *NIST-JANAF Thermochemical Tables, Fourth Edition, J. Phys. Chem. Ref. Data, Monograph 9* 1998), pp. 1-1951.

[68] T. Hickel, B. Grabowski, F. Körmann, and J. Neugebauer, *J. Phys.: Condens. Matter* **24**, 053202 (2012).

---

# Chapter 4

## Impact of point defects on the electronic structure of paramagnetic CrN

---

### 4.1 Motivation

The electronic structure of perfect CrN has been addressed previously by *ab initio* calculation [1–5] as well as by experiments [6–8], and was discussed in Chapter 3. In this chapter, we report on *ab initio* calculations of stability changes induced by point defects in pm-CrN. The electronic structure and Electron Energy Loss Near Edge Structure (ELNES) spectra are discussed in conjunction with N vacancies, and the results are carefully compared with recent experimental reports [7, 8].

### 4.2 Computational details

The structural models for cubic pm-CrN including vacancies were generated according to the SQS method [9–11] by optimising the short-range order parameters up the 5th nearest neighbour distance for supercells containing 64 sites (32 Cr and 32 N). The paramagnetic state was modelled by assuming Cr spin up and Cr spin down as two inequivalent species within the SQS scheme. The supercells were structurally relaxed using the Density Functional Theory [12, 13] implemented in Vienna Ab initio Simulation Package [14, 15] employing projector augmented wave pseudopotentials [16] with the local (spin) density approximation (L(S)DA) [12] for the exchange and correlation effects. Plane-wave cut-off energy was set to 500 eV and the Monkhorst-Pack mesh had  $6 \times 6 \times 6$   $k$ -points. Additionally, the on-site Coulomb interaction term,  $+U = 3$  eV, was applied to Cr  $d$ -states to improve the electronic structure description [17–20]. It has been shown previously that this approach yields very good description of the

structural, elastic and electronic properties of CrN, including its semiconducting character and Néel temperature of the anti-ferromagnetic-to-paramagnetic transition [11] (see also Chapter 3).

The Electron Energy Loss Near Edge Structures (ELNES) were modelled using a Telnes program [21] which is a part of the Wien2k [22], an all-electron full-potential implementation of DFT. The optimised super-cells from VASP were taken as inputs for the structural description of paramagnetic CrN<sub>x</sub>. Spherical harmonics up to  $l_{\max} = 10$  and plane-waves up to a cut-off defined by  $R_{\text{MT}} * R_{\max} = 7$  together with the muffin-tin radii of  $R_{\text{MT}}(\text{Cr}) = 2.00$  Bohr and  $R_{\text{MT}}(\text{N}) = 1.72$  Bohr were used for expansion of the total wave function on an automatically generated grid with 45 k-points. The ELNES were calculated using a Slater's transition state in which 0.5e from the initial core state was put into the conduction band (final states) [23].

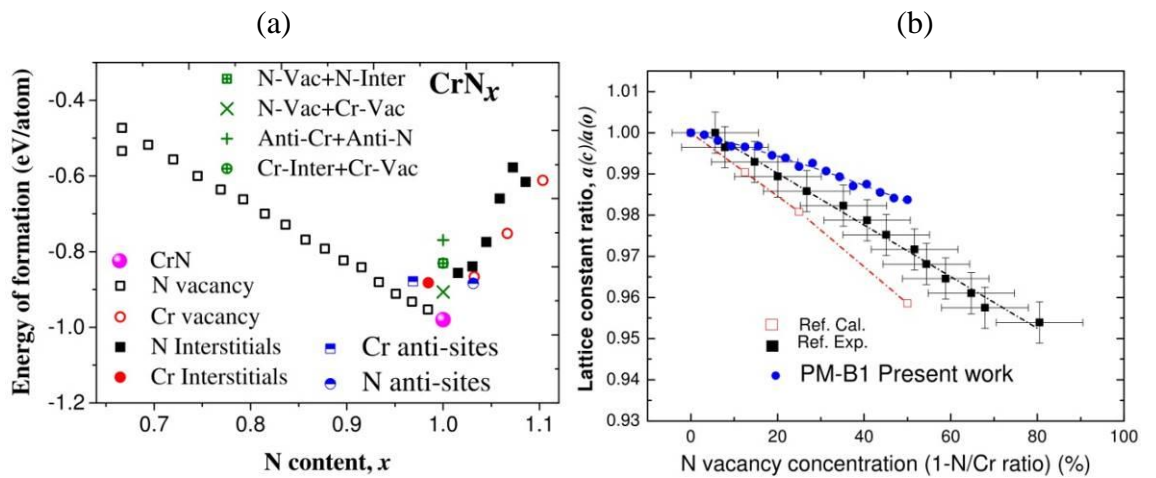
## 4.3 Results and discussion

### 4.3.1 Stability of point defects in CrN

Energy of formation,  $E_f$ , is a measure of the chemical stability of a compound. It is calculated as

$$E_f(\text{CrN}_x) = E_{\text{tot}}(\text{CrN}_x) - \frac{mE_{\text{tot}}(\text{Cr}^{bcc}) + 0.5nE_{\text{tot}}(\text{N}_2)}{m+n}$$

where  $E_f(X)$  is the total energy of  $X$  per atom in its stable configuration, and  $m$  and  $n$  are the numbers of Cr and N atoms, respectively, in the (defected) supercell representing CrN<sub>x</sub>.



---

Figure 4.1: (a) Energy of formation,  $E_f$ , as a function of N content in  $\text{CrN}_x$  with various point-defects described in the text. (b) Cubic lattice parameter,  $a$ , of N deficient  $\text{CrN}_x$  relative to the value  $a_0$  of perfect stoichiometric CrN. Experimental and non-magnetic calculated values are taken from Ref. [8].

Our calculations show that out of all the here investigated defects, the most stable configuration is the perfect (undefected) CrN (see Fig. 4.1a). Both N vacancies and Cr vacancies yield almost linear increase of the energy of formation as their concentration increases. The overall N content can be decreased by N vacancies as well as by an introduction of Cr interstitial or Cr anti-sites. However, our predictions suggest that the latter two types of defects possess significantly higher energy than structures with the same chemistry obtained using N vacancies. We therefore conclude that when CrN material is N-deficient, it happens most likely due to the formation of N vacancies, which is in agreement with experimental observations [8].

The situation is not straightforward for the N-rich side ( $x > 1$ ) of the diagram in Fig. 4.1a. For example, for  $x \approx 1.04$ ,  $E_f$  of structures with N interstitials is only 28 meV/at. higher than when the same composition is obtained by Cr vacancies. Interestingly enough, the overall lowest energy exhibits a configuration with N anti-sites, which is  $\approx 17$  meV/at. more favorable than the Cr vacancy configuration. Nevertheless, since these differences are in the range of thermal vibrations at room temperature  $k_b T \approx 25$  meV we predict that Cr vacancies in addition to N anti-sites are to be expected in experimental samples with N-rich compositions at room temperature.

Finally we note that for stoichiometric CrN our calculations clearly favour a perfect crystal to structures containing Frenkel defects (an interstitial–vacancy pair), vacancies or anti-sites.

The predicted cubic lattice parameter of the pm-CrN as a function of the N content is shown in Fig. 4.1b together with experimental and calculated data from Ref. [8]. Our predictions exhibit slightly slower decrease of the lattice parameter with decreasing N content as compared with the experimental data, while the previously published calculated lattice parameter shows more rapid decrease. We ascribe this difference to the fact that the calculations in Ref. [8] were

performed on rather small supercells (16 atoms as compared with 64 used in the present work) and neglecting the magnetic effects. The discrepancy between the here predicted and experimental slope can be rationalized by the fact that the vacancies are randomly distributed in our structural models while experimentally they were reported to be ordered [8].

### 4.3.2 N K-edge of CrN<sub>x</sub>

The calculated evolution of the N K-edge (N  $1s \rightarrow 2p$  transition) ELNES with increasing amount of N vacancies is shown in Fig. 4.2a. The spectra are averaged over all N sites in the supercell, and are normalized to the intensity of the first peak at about 2 eV. The spectra of the cubic phase exhibit also a second peak at about 12 eV, whose intensity gradually decreases with increasing amount of the nitrogen vacancies. This is qualitatively the same behavior as observed in experiments [8].

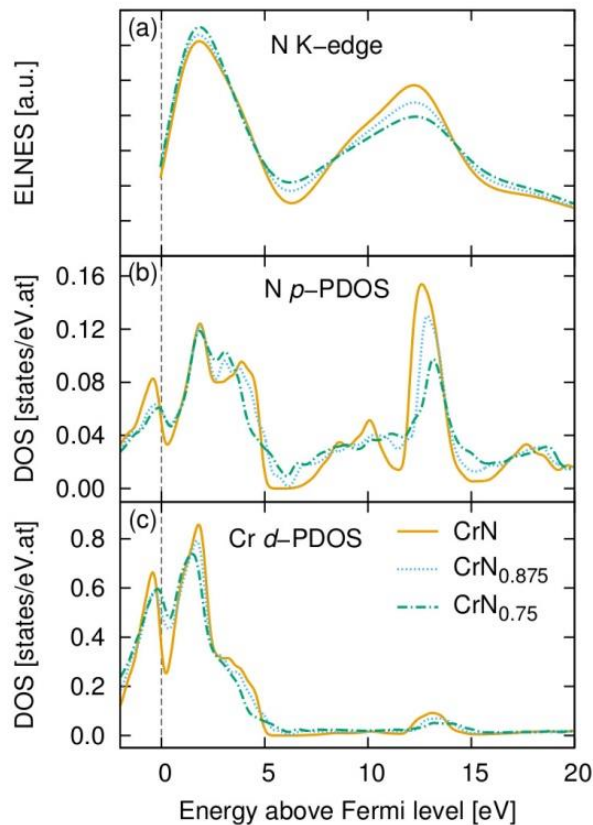


Figure 4.2: (a) N K-edge ELNES, (b) N  $p$ -PDOS, and (c) Cr  $d$ -PDOS for pm-CrN (solid line), pm-CrN<sub>0.875</sub> (dotted line), and pm-CrN<sub>0.75</sub> (dash-dotted line).

A comparison of the calculated N K-edge with the density of states projected on N  $p$ - and Cr  $d$ -states reveals two facts. Firstly, N K-edge corresponds well with the (strongly) broadened N  $p$ -PDOS (similarly to e.g., previous reports for  $\text{Ti}_{1-x}\text{Al}_x\text{N}$  [23]). This is, however, expected as the unoccupied N  $p$ -states are the final states of the N K-edge excitation. The small peak at around 10 eV above the Fermi level is responsible for the shoulder at the lower-energy side of the second N K-edge peak, hence causing its asymmetry. Secondly, the unoccupied N  $p$ -states are well hybridized with the Cr  $d$ -states, which is related to formation of bonding and anti-bonding  $sp^3d^2$  orbitals (the latter in the conduction band). Hence, when N vacancies are introduced, this hybridization becomes weaker which is reflected by broadening of the peak at around 10 eV above the Fermi level together with lowering the peak intensity of the second PDOS peak at  $\approx 13$  eV above Fermi level. Consequently, the amount of states in the region of the second N K-edge ELNES peak becomes smaller with increasing N vacancy content, causing the corresponding intensity drop.

The curves in Fig. 4.2 represent macroscopic trends since they were obtained by averaging the ELNES or PDOS curves over all N or Cr sites. However, the same trends as described above are present also in a single defected cell in which N and Cr atoms with different numbers of the second and the first nearest neighbors, respectively, exist due to the presence of vacancies.

(b)

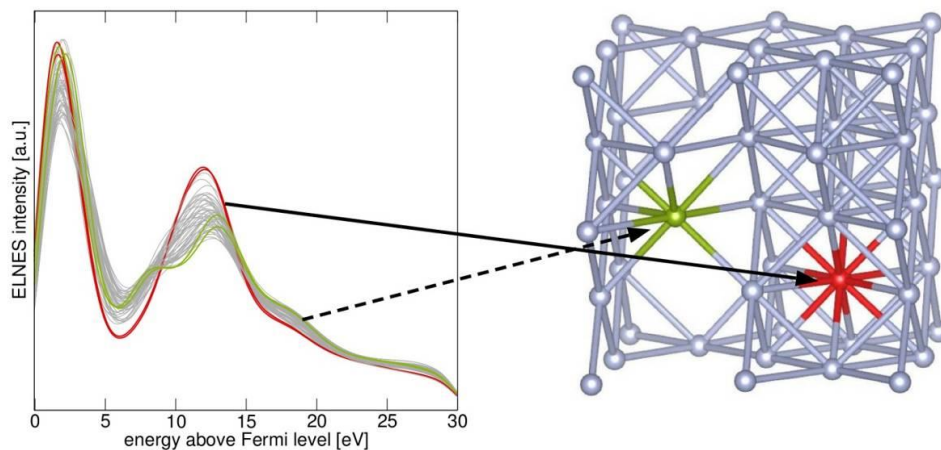


Figure 4.3: (a) Impact of the local environment on the calculated N K-edge ELNES. (b) N sublattice with vacancies. The colored sites in (b) correspond with the same colored curves in

---

the graph in (a), representing ideally stoichiometric (red, solid line arrow) and strongly N-deficient (green, dashed arrow) environments.

This is clearly demonstrated in Fig. 4.3 showing that when the excitation takes place on a N atom with a bulk-like environment, the N K-edge ELNES resembles that of perfect CrN, while N site with a high amount of N vacancies in its neighborhood results in splitting of the second peak (compare Figs. 4.3a and 3b).

The N K-edge onset could be estimated as a difference in the total energy of an unperturbed (initial state) and excited (final state with a full core hole) system [23]. This analysis yields values of 395.3, 400.9, and 401.1 eV for CrN, CrN<sub>0.875</sub>, and CrN<sub>0.75</sub>, respectively. Although the absolute values do not agree with the data from Ref. [8], the trend that the edge onset increases with the N vacancy concentration is well reproduced. The same procedure applied to CrN<sub>2</sub> yields a valued of 401.7 eV for the N K-edge onset. Again, the qualitative fact that N K-edge onset increases from CrN to CrN<sub>2</sub> agrees well with the observations reported in [7].

In Ref. [8] it is argued that the increased number of N vacancies leads to an increased metallic character of the compound. We have performed Bader's analysis [24] to quantify the charge transfer from Cr to N atoms. In perfect CrN, approximately 1.45 e/at. is transferred from Cr atoms (hence making them positively charged cations) to N atoms (thus becoming negatively charged anions). When performing the same analysis in a supercell with 25% of N sites being vacant, the average extra charge on remaining 75% N sites is  $\approx 1.43$  eV, i.e. it remains almost unchanged with respect to the N sites in CrN. For the cell to be neutral this means that each Cr site loses on average a smaller fraction of its charge ( $\approx 1.08$  eV), consequently leaving more charge "available" to participate in metallic bonding. The strong dependence of the charge transfer on the local environment is presented in Fig. 4.4. Although the data are somewhat scattered, a trend that the charge transferred from a Cr site is proportional to the number of N nearest neighbours is envisioned (see the dotted linear fit in Fig. 4.4). The larger scatter for the Cr sites next to vacancies suggests that also the longer range interactions are not negligible. We therefore conclude that it is directly the vacancy-altered charge transfer which yields reduced

ionic and profound metallic bonding character rather than changed lattice constant reduction as speculated in Ref. [8].

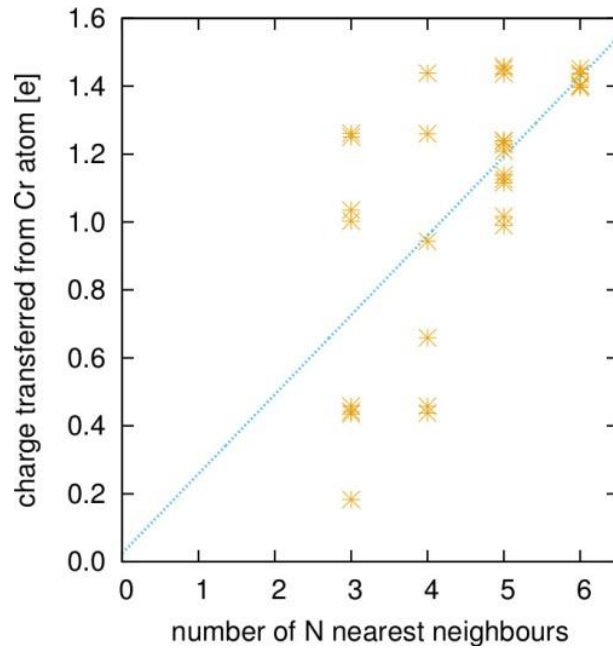


Figure 4.4: Bader’s analysis of the charge transferred from Cr sites in  $\text{CrN}_{0.75}$  supercell. The dotted line represents a linear fit to the data ( $R^2 = 0.44$ ).

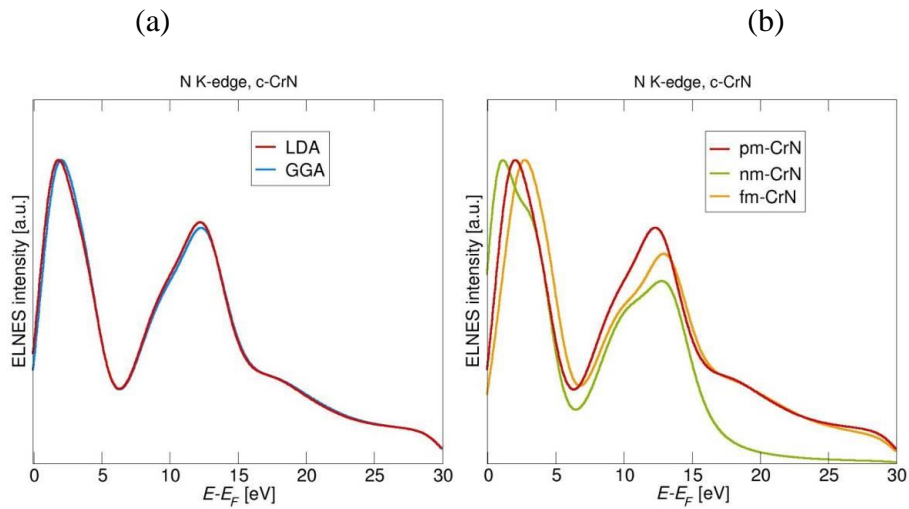


Fig. 4.5: (a) Comparison of the impact of exchange-correlation potential (LDA vs. GGA) on the predicted shape of the N K-edge. (b) Impact of the exact magnetic state on the N K-edge shape: “pm”, “nm” and “fm” refer to paramagnetic, non-magnetic and ferromagnetic, respectively.

To strengthen our conclusions, we have performed a number of additional calculations, see Fig.

---

4.5: The N K-edges are almost identical irrespective of whether L(S)DA or generalised gradient approximation (GGA) [25] is used for the exchange-correlation effects. On the other hand, to neglect the magnetic nature of CrN seems to be much more serious: each of the two main N K-edge peaks splits into two when CrN is treated non-magnetically. For the ferromagnetic arrangement of spins, the resulting edge shape is very close to the paramagnetic-state curve.

#### 4.4 Conclusions

In this chapter, the stability of point defects in  $\text{CrN}_x$  and the impact on electronic structure changes induced by N vacancies was studied. Our calculations of energy of formation and lattice parameters confirmed that the experimentally observed N understoichiometry is likely to be related to N vacancies rather than to any other point defect. Simulations of a N K-edge ELNES evolution with amount of N vacancies yields the same behaviour as observed previously by transmission electron microscopy: The edge shape has two peaks separated by  $\approx 10$  eV. With the increasing content of N vacancies the relative intensity of the second peak (with respect to the first peak) decreases, and a shoulder at its lower-energy side increases. We ascribe these changes to the decreased hybridization of N  $p$ - and Cr  $d$ -states, and a decreased ionicity as more N vacancies are present. Our results demonstrate the strong dependence of ELNES on the local environment of a site where the excitation takes place.

---

# References

- [1] J. F. Harrison, *J. Phys. Chem.* **100**, 3513 (1996)
- [2] B. Alling, A. Karimi, and I.A. Abrikosov, *Surf. Coat. Technol.* **203**, 883 (2008).
- [3] L. He and Z. Zhi, *Chin. Physics B* **20**, 077102 (2011).
- [4] A. S. Botana, F. Tran, V. Pardo, D. Baldomir, and P. Blaha, *Phys. Rev. B* **85**, 235118 (2012).
- [5] A. S. Botana, V. Pardo, D. Baldomir, and P. Blaha, *Phys. Rev. B* **87**, 075114 (2013).
- [6] X. Y. Zhang and D. Gall, *Phys. Rev. B* **82**, 045116 (2010).
- [7] Z. Zhang, R. Daniel, and C. Mitterer, *J. Appl. Phys.* **110**, 043524 (2011).
- [8] Z. Zhang, H. Li, R. Daniel, C. Mitterer, and G. Dehm, *Phys. Rev. B* **87**, 014104 (2013).
- [9] S.-H. Wei, L. Ferreira, J. Bernard, and A. Zunger, *Phys. Rev. B* **42**, 9622 (1990).
- [10] L. Zhou, D. Holec, and P. H. Mayrhofer, *J. Phys. D Appl. Phys.* **46**, 365301 (2013).
- [11] L. Zhou, F. Körmann, D. Holec, M. Bartosik, B. Grabowski, J. Neugebauer, and P. H. Mayrhofer, *Phys. Rev. B* **90**, 184102 (2014).
- [12] W. Kohn and L. J. Sham, *Phys. Rev.* **140**, A1133 (1965).
- [13] P. Hohenberg and W. Kohn, *Phys. Rev.* **136**, B864 (1964).
- [14] G. Kresse and J. Furthmüller, *Comput. Mater. Sci.* **6**, 15 (1996).
- [15] G. Kresse and J. Furthmüller, *Phys. Rev. B* **54**, 11169 (1996).
- [16] G. Kresse and D. Joubert, *Phys. Rev. B* **59**, 1758 (1999).
- [17] B. Alling, T. Marten, and I. A. Abrikosov, *Phys. Rev. B* **82**, 184430 (2010).
- [18] B. Alling, T. Marten, and I. A. Abrikosov, *Nat. Mater.* **9**, 283 (2010).
- [19] P. Steneteg, B. Alling, and I. A. Abrikosov, *Phys. Rev. B* **85**, 1 (2012).
- [20] N. Shulumba, B. Alling, O. Hellman, E. Mozafari, P. Steneteg, M. Odín, and I. A. Abrikosov, *Phys. Rev. B Condens. Matter* **89**, 174108 (2014).
- [21] K. Jorissen, J. Luitz, and C. Hébert, *A Program for the Calculation of Energy Loss Near Edge Structure. The New and Improved TELNES.2 Code* (2005).
- [22] P. Blaha, K. Schwarz, G. Madsen, D. Kvasnicka, and J. Luitz, “WIEN2k, An Augmented Plane Wave + Local Orbitals Program for Calculating Crystal Properties” (Karlheinz Schwarz,

---

Techn. Universit ä Wien, Austria, 2001).

[23] D. Holec, R. Rachbauer, D. Kiener, P. D. Cherns, P. M. F. J. Costa, C. McAleese, P. H. Mayrhofer, and C. J. Humphreys, *Phys. Rev. B* **83**, 165122 (2011).

[24] R. Bader, *Atoms in molecules* (Wiley Online Library, 1990).

[25] J. P. Perdew, K. Burke, and M. Ernzerhof, *Phys. Rev. Lett.* **77**, 3865 (1996).

---

# Chapter 5

## First-principles study of elastic properties of cubic $\text{Cr}_{1-x}\text{Al}_x\text{N}$ alloys

---

### 5.1 Motivation

Information on the elastic properties is important for understanding and predicting the mechanical and dynamical behavior, and for indications of material-related properties such as hardness, brittleness, ductility, fracture toughness, and bond characteristics necessary for a knowledge-based coatings design. There are lots of theoretical studies on the phase stability of cubic B1  $\text{Cr}_{1-x}\text{Al}_x\text{N}$ . However, a thorough study of its elastic properties is still missing. In this chapter, the compositional dependence of the elastic properties of paramagnetic cubic B1 (c-)  $\text{Cr}_{1-x}\text{Al}_x\text{N}$  ternary alloys are systematically studied using stress-strain and energy-strain methods within the framework of Density Functional Theory (DFT). The special quasi-random structures (SQS) [1] approach is applied to model both, the chemical as well as magnetic disorder representing the paramagnetic state of the  $(\text{Cr}_{0.5}^{\uparrow}\text{Cr}_{0.5}^{\downarrow})_{1-x}\text{Al}_x\text{N}$  system. We first obtained structural properties (lattice parameters, energies of formation) to compare our results with those from literature. Further, we calculated the single crystal elastic properties using two methods, the energy-strain and stress-strain method. Subsequently, we applied the self-consistent Hershey homogenization scheme [2] to obtain the isotropic polycrystalline estimates of the elastic response.

### 5.2 Methodology

Mixing of  $\text{Cr}^{\uparrow}$ ,  $\text{Cr}^{\downarrow}$  and Al atoms takes place on one sublattice following the SQS methodology, while the other sublattice is fully occupied with N atoms.  $3 \times 3 \times 2$  (36 atoms) and  $2 \times 2 \times 2$  (32

---

atoms) supercells are used for the cubic B1 and wurtzite B4 structures, respectively. The short range order parameters (SROs) are optimized for pairs at least up to fifth order. The thus generated structures together with the corresponding SROs are listed in Appendix A (Table A.1 to A.4). It is noticed that the SROs on the first coordination shell for almost all the SQSs are negative, which is likely to be caused by using considerably small supercells. Test calculations are performed to check for the influence of the size of the SQS on the elastic constants, and it is found that the SQS supercell with worse SROs also yield reasonably accurate ( $\delta C_{11} < 1\%$ ,  $\delta C_{12} < 1\%$ ,  $\delta C_{44} < 5\%$ ) elastic constants when the full elastic tensor is calculated, a result which has been reported also by Tasnádi *et al.* [3].

The density functional theory based calculations are performed using the Vienna Ab initio Simulation Package (VASP) [4,5]. The ion-electron interactions are described by the projector augmented wave method (PAW) [6] with an energy cutoff of 500 eV, and the generalized gradient approximation (GGA) for the exchange-correction effects, which is parameterized by Perdew–Burke–Ernzerhof (PBE) [7]. The  $k$ -point meshes are  $6 \times 6 \times 9$  and  $7 \times 7 \times 5$  for the cubic B1 and the wurtzite B4 structures, respectively. The energy convergence criterion for electronic self-consistency is 0.1 meV/atom.

In principle, there are two routes of computing single crystal elastic constants from first-principles calculations: the energy-strain approach and the stress-strain approach [8,9]. The energy-strain approach [9] is based on the computed total energies of properly selected strained states of the crystal. The second order elastic constants appear, via Hooke's law, in the second order Taylor expansion coefficient of the strain energy. Assuming the cubic symmetry of the cubic supercell, three independent elastic constants,  $C_{11}$ ,  $C_{12}$  and  $C_{44}$ , are to be determined. Two deformation modes with keeping the unit cell volume constant [10] are employed and the bulk modulus,  $B$ , is derived from the Birch-Murnaghan equation of state (EOS) [11]. More details about the derivation of the elastic constants of cubic B1 structure can be found in Ref. [10].

The stress-strain approach, on the other hand, utilizes the stress tensor calculated by VASP.

---

Hence the elastic constants can be directly derived from the generalized Hooke's law. A set of strains  $\varepsilon = (\varepsilon_1, \varepsilon_2, \varepsilon_3, \varepsilon_4, \varepsilon_5, \varepsilon_6)$  (where  $\varepsilon_1, \varepsilon_2$  and  $\varepsilon_3$  are the normal strains,  $\varepsilon_4, \varepsilon_5$  and  $\varepsilon_6$  are the shear strains in Voigt's notation<sup>39</sup>) is imposed on a crystal, by alternating the unit cell lattice vectors ( $\bar{R}$ ) from the original ( $R$ ) as follows:

$$\bar{R} = R \begin{pmatrix} 1 + \varepsilon_1 & \varepsilon_6 / 2 & \varepsilon_5 / 2 \\ \varepsilon_6 / 2 & 1 + \varepsilon_2 & \varepsilon_4 / 2 \\ \varepsilon_5 / 2 & \varepsilon_4 / 2 & 1 + \varepsilon_3 \end{pmatrix} \quad (5.1)$$

A 6x6 elastic constants matrix,  $C$ , with components of  $C_{ij}$  in Voigt's notation, relates the strain vector  $\varepsilon$  with the stress vector  $\sigma = (\sigma_1, \sigma_2, \sigma_3, \sigma_4, \sigma_5, \sigma_6)$  as  $\sigma = \varepsilon C$ . In the present work, the following six linearly independent sets of strains are applied:

$$\begin{pmatrix} x & 0 & 0 & 0 & 0 & 0 \\ 0 & x & 0 & 0 & 0 & 0 \\ 0 & 0 & x & 0 & 0 & 0 \\ 0 & 0 & 0 & x & 0 & 0 \\ 0 & 0 & 0 & 0 & x & 0 \\ 0 & 0 & 0 & 0 & 0 & x \end{pmatrix} \quad (5.2)$$

where each row is one set of strains  $\varepsilon$  with  $x$  being a normal (or shear) strain  $\varepsilon_i$ . After  $n$  first-principles calculations upon the deformed lattices due to  $n$  sets of strains  $\varepsilon$ , the corresponding stress matrix  $\sigma$  with  $n$  sets of stresses is obtained. Based on Hook's law, the elastic stiffness constants matrix,  $C$ , is determined as,

$$C = \varepsilon^{-1} \sigma \quad (5.3)$$

where '-1' represents the pseudo-inverse, solved by the singular value decomposition method.

Recently, Tasnádi *et al.* [3] pointed out that using SQS approach to model the disordered state results in 21 elastic constant elements in the elastic tensor matrix of disordered solid solution, due to the point group symmetry broken by the SQS approach [1]. This implies the need for applying 21 independent deformation modes for deriving 21 elastic constants using the

---

energy-strain approach. Such a treatment is extremely computationally expensive. The stress-strain approach, on the contrary, is much more efficient as the six strains (Eq. 5.2) are sufficient to obtain a full elastic constants matrix [8,12]. Finally, the macroscopic cubic elastic constant,  $\overline{C_{11}}$ ,  $\overline{C_{12}}$ , and  $\overline{C_{44}}$ , are obtained by simple averaging [13]:

$$\overline{C_{11}} = (C_{11} + C_{22} + C_{33}) / 3 \quad (5.4)$$

$$\overline{C_{12}} = (C_{12} + C_{13} + C_{23}) / 3 \quad (5.5)$$

$$\overline{C_{44}} = (C_{44} + C_{55} + C_{66}) / 3 \quad (5.6)$$

Calculations are performed from  $x=\pm 0.007$  up to  $\pm 0.042$  with a step equal to 0.007, and different  $k$ -point meshes  $4 \times 4 \times 6$  to  $12 \times 12 \times 18$ , indicating that the predicted errors of  $C_{ij}$  are quite small ( $< 2\%$ ). Finally,  $x=\pm 0.007$  and  $k$ -point sampling  $6 \times 6 \times 9$  are chosen in the present work. Based on the single crystal elastic constants  $C_{ij}$ , the isotropic equivalents of polycrystalline properties are computed via the self-consistent Hershey approach [2].

## 5.3 Results and discussion

### 5.3.1 Equilibrium properties

We performed the calculations of c-Cr<sub>1-x</sub>Al<sub>x</sub>N in the PM and NM states and w-Cr<sub>1-x</sub>Al<sub>x</sub>N in the PM state. The calculated energy of formation,  $E_f$ , as a function of the AlN content,  $x$ , is presented in Fig. 5.1, where third-order polynomial fittings serve as guidelines for the eye.

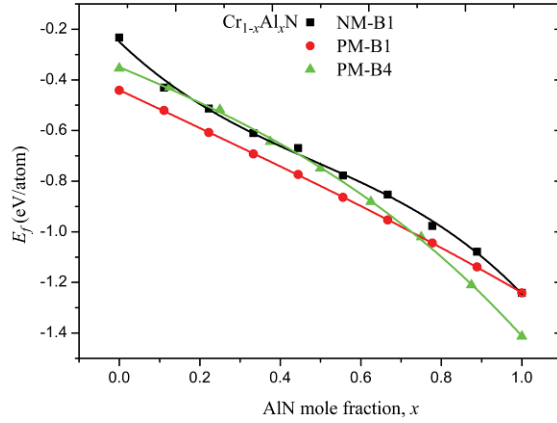


Figure 5.1: Energy of formation,  $E_f$ , as a function of  $x$  for  $\text{Cr}_{1-x}\text{Al}_x\text{N}$  in the NM (solid square), PM (solid circle) states cubic B1 structures and PM state B4 structure (solid triangle).

The  $E_f$  differences of c- $\text{Cr}_{1-x}\text{Al}_x\text{N}$  in the PM and NM states are significant;  $E_f$  differences of PM c- $\text{Cr}_{1-x}\text{Al}_x\text{N}$  is up to 0.1 eV/atom lower than that of NM state. This suggests that the PM state cannot be neglected. Comparing  $E_f$  of c- and w- $\text{Cr}_{1-x}\text{Al}_x\text{N}$  in the PM state yields the maximum solubility of AlN in c- $\text{Cr}_{1-x}\text{Al}_x\text{N}$  at around  $x \approx 0.75$ , a value consistent with previous experimental and theoretical calculation results [14,15].

The calculated lattice parameter,  $a$ , and bulk modulus,  $B$ , of c- $\text{Cr}_{1-x}\text{Al}_x\text{N}$  in the PM and NM states as a function of Al content,  $x$ , are shown in Figs. 2a and 2b.

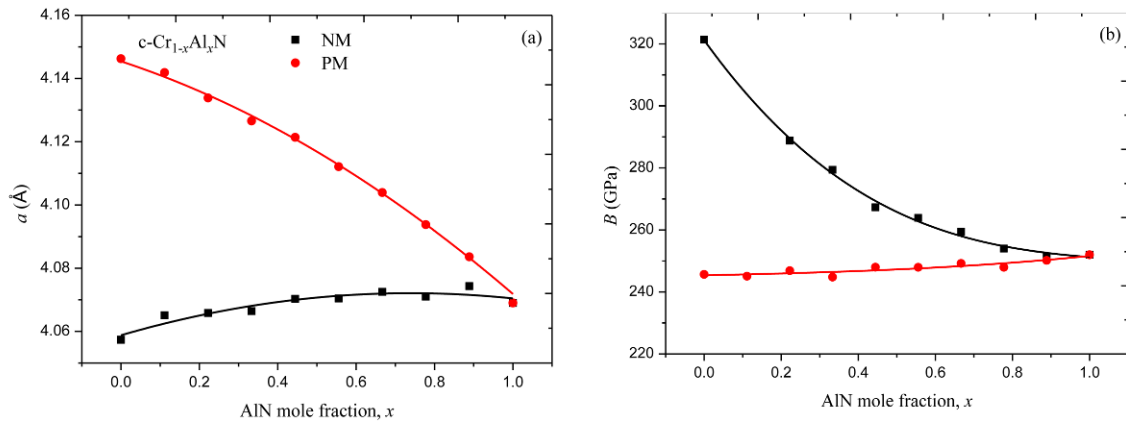


Figure 5.2: (a) Lattice parameter,  $a$ , and (b) calculated bulk modulus,  $B$ , variation with  $x$  for the NM (solid square) and PM (solid circle) state of c- $\text{Cr}_{1-x}\text{Al}_x\text{N}$ .

There is a small noise for the calculated lattice parameters, likely due to the limited size of the

---

SQS supercells and also due to magnetic spin arrangement (see section 5.3.1). As demonstrated in Fig. 5.2a, the calculated lattice parameters of c-Cr<sub>1-x</sub>Al<sub>x</sub>N in the PM and NM states as functions of AlN content have different trends. The lattice parameter of PM c-Cr<sub>1-x</sub>Al<sub>x</sub>N decreases from 4.145 Å to 4.069 Å as AlN content increases from 0 to 1, agreeing well with those previously reported in the literature [15], which is well supported by experimental results [16-19]. Contrarily, the lattice parameters of NM c-Cr<sub>1-x</sub>Al<sub>x</sub>N exhibit a small increase as AlN content increases from 0 to 1. Similar to other Al-containing cubic transition metal nitrides, also here we predict a positive bowing away from the Vegard's-like behavior [20]. The respective bowing parameters are 0.034 Å and 0.024 Å for PM and NM states, respectively. The bowing is attributed to a gradual change of the bonding character with Al content. One should notice that the bowing parameters mentioned here are derived from the curves fitted from the calculated lattice parameters. Actually, due to the small noise for the calculated lattice parameters as mentioned above, there is some uncertainty in bowing parameter. However, the uncertainty in bowing parameter should not be over-interpreted due to the scatter of the calculated lattice constants. The bulk modulus,  $B$ , of c-Cr<sub>1-x</sub>Al<sub>x</sub>N in the PM state presented in Fig. 5.2b is almost constant as increases from 0 to 1 (overall change of  $\approx 5$  GPa), while NM state calculations for c-Cr<sub>1-x</sub>Al<sub>x</sub>N show a steep decreasing trend, with  $B$  decreasing from 329 to 252 GPa as increases from 0 to 1. The bulk modulus  $B$  of c-Cr<sub>1-x</sub>Al<sub>x</sub>N in the PM state is smaller than that of the NM state in the whole composition range. This is mostly the effect of different equilibrium volumes of those two phases: according to the Murnaghan equations of state [11], the bulk modulus  $B$  increases with the pressure,  $B = B_0 + \frac{dB_0}{dP} P$ , i.e., with decreasing the lattice parameter at certain composition. Indeed, when e.g., the PM bulk modulus is extrapolated to the NM equilibrium volume, a value close to that of NM  $B_0$  is obtained. In agreement with Alling *et al.* [21], we once again conclude that the proper consideration of the PM state is essential for the Cr<sub>1-x</sub>Al<sub>x</sub>N alloy.

### 5.3.2 Accuracy of paramagnetic state model

In order to obtain the elastic constants, we fully relax the structure including optimizing cell

volume, shape as well as all internal atomic positions to obtain the equilibrium state. After imposing a series of strains on the equilibrium structure, only the relaxation of atomic positions according to strain-induced forces is allowed. The SQSs are used to address simultaneously magnetic and chemical disorder in the  $\text{Cr}_{1-x}\text{Al}_x\text{N}$  system. In reality, the heavy ions cannot follow the fast flipping of the spins and thus the artificial static displacements induced by the different orientations of local moments and different local magnetic environments in a static SQS calculation are questionable. Magnetic sample method [22,23] offers a solution to this problem. There, a large number of calculations with different random spin up and spin down magnetic arrangements are performed in parallel and the model of the paramagnetic state is constructed by statistically averaging the individual spin configurations. To gain some insight of the influence of the artificial spin-induced displacements on the elastic constants, test calculations are performed for five spin configurations of c- $\text{Cr}_{0.44}\text{Al}_{0.56}\text{N}$ . Based on the SQS supercell for the c- $\text{Cr}_{0.44}\text{Al}_{0.56}\text{N}$  in PM state, a series of random up and down spin arrangements are imposed on the Cr atoms and the elastic constants are calculated. The results show that the elastic constants from different randomly magnetic spin arrangements fluctuate with respect to each other (see Fig. 5.3), but the average values of elastic constants of randomly distributed magnetic spins are close to those of a single SQS supercell.

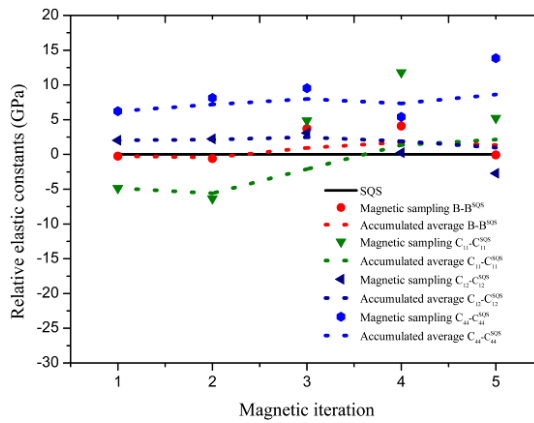


Figure 5.3: The relative elastic constants of five randomly magnetic sampling configurations based on the SQS supercell of c- $\text{Cr}_{0.44}\text{Al}_{0.56}\text{N}$  in the PM state. Magnetic iteration denotes the accumulated average (dot lines) of the randomly magnetic sampling using randomly magnetic sampling method.

The agreement improves as the number of magnetic samples increases. The largest deviation only up to ~5% is obtained for the  $C_{44}$  elastic constant ( $C_{44}^{\text{averaged}}=203$  GPa,  $C_{44}^{\text{SQS}}=194$  GPa).

Table 5.1: The elastic constants (in GPa) of c-CrN in the PM state derived from stress-strain method.

	$B$	$C_{11}$	$C_{12}$	$C_{44}$
Type i	248	516	115	116
Type ii	252	534	111	120
Type iii	250	524	113	118

Hence we can conclude that an optimized SQS yields almost the same results as much more computationally demanding magnetic sample method. Furthermore, pure CrN offers the possibility to study the influence of artificial magnetic displacement in a detail as no chemical disorder is present. We have performed three kinds of calculations for the pure CrN:

- (i) equilibrium structure with optimized cell shape and atomic positions relaxed during equilibrium as well as deformed structure calculations.
- (ii) equilibrium structure fully relaxed (cell shape and atomic positions), while atomic positions fixed during the stress-strain method.
- (iii) keeping the ideal B1 cubic structure (ideal atomic positions) for the equilibrium calculation, and the atomic positions keeping fixed in the subsequent deformed structures.

The results are summarized in table 5.1, the largest deviation between those model cases of ~4% is obtained for  $C_{11}$  and  $C_{44}$ . Moreover, the relative differences between type (i) and type (iii) calculations, which address the artificial displacement due to the magnetic moments, are well below 2%. Based on the above discussion, we therefore conclude that the static SQS structures are suitable model for simultaneously addressing chemical and magnetic disorder,

and are capable of predicting the elastic constants with accuracy better than ~5% as compared with more sophisticated, but also significantly more computationally demanding magnetic sample model.

### 5.3.3 Elastic properties

The compositional trends in the elastic response of c-Cr<sub>1-x</sub>Al<sub>x</sub>N in the PM state are studied using energy-strain and stress-strain methods. All independent components of the c-Cr<sub>1-x</sub>Al<sub>x</sub>N, as calculated by the stress-strain method, are summarized in table 5.2. The thus obtained elastic tensors exhibit small deviations from a strict cubic symmetry, similarly to the results of Tasnádi *et al.*[3] for Ti<sub>0.5</sub>Al<sub>0.5</sub>N. Figure 5.4a presents the obtained *ab initio* predicted cubic single-crystal elastic constants,  $C_{11}$ ,  $C_{12}$  and  $C_{44}$ , of c-Cr<sub>1-x</sub>Al<sub>x</sub>N as a function of Al content. For all compositions, the elastic constants fulfill the Born stability criteria [24] for cubic crystals,

$$C_{44} > 0, C_{11} > |C_{12}|, C_{11} + 2C_{12} > 0 \quad (5.7)$$

Table 5.2: Elastic tensors (in GPa) of c-Cr<sub>1-x</sub>Al<sub>x</sub>N calculated by stress-strain method.

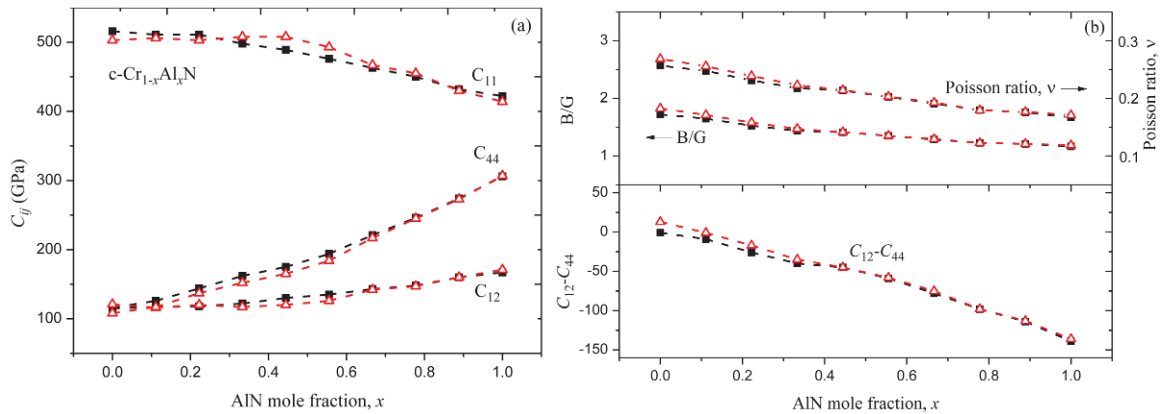
$x$	$C_{11}$	$C_{22}$	$C_{33}$	$C_{12}$	$C_{13}$	$C_{23}$	$C_{44}$	$C_{55}$	$C_{66}$	$C_{46}$	$C_{56}$
1	426	426	426	167	167	167	306	306	306	0	0
0.89	433	431	433	161	160	160	274	274	274	0	0
0.78	442	455	453	150	148	146	246	246	247	0	1
0.67	461	466	464	143	145	142	220	224	220	-1	1
0.56	466	494	468	134	140	131	188	202	193	1	0
0.44	474	504	488	129	136	123	167	183	175	1	-1

---

0.33	493	510	492	117	123	124	164	163	159	0	2
0.22	513	513	505	117	118	119	150	141	141	0	-1
0.11	515	518	499	119	117	115	123	132	123	-1	-1
0	521	515	512	111	118	115	109	127	111	0	0

---

The elastic constants from stress-strain and energy-strain methods show a good agreement. The elastic constants  $C_{11}$  of c- $\text{Cr}_{1-x}\text{Al}_x\text{N}$  are significantly stiffer than the other two elastic constants,  $C_{12}$  and  $C_{44}$ , in particular for the Cr-rich composition.  $C_{12}$  and  $C_{44}$  constants increase with the amount of Al, while  $C_{11}$ , in contrast, shows a small decrease as Al content increases. These compositional trends in the  $\text{Cr}_{1-x}\text{Al}_x\text{N}$  system are very similar to those predicted for the  $\text{Ti}_{1-x}\text{Al}_x\text{N}$  system [25]. Some insight in these trends brings the analysis of the chemical bonding. A strong hybridization of  $sp^3d^2$  orbitals accompanied with a weak hybridization of second next-nearest neighboring Cr  $d$  state takes place in CrN [26]. AlN, on the other hand, is a semiconductor with bonding of an ionic-covalent nature due to significantly larger charge transfer from cation to anion accompanying a strong Al  $3s$ -N  $2p$  hybridization [27,28]. We can therefore conclude that the weak  $d$ - $d$  bonding (metallic interaction) in CrN is responsible for the low value of the  $C_{44}$  elastic constant, while its high value in AlN is caused by strong Al-Al and N-N repulsion as they get closer under the shear deformation.



---

Figure 5.4: (a) Calculated elastic constants ( $C_{11}$ ,  $C_{12}$  and  $C_{44}$ ), and (b) calculated bulk modulus,  $B$ , polycrystalline Young's modulus,  $E$ , and shear modulus,  $G$  of PM c-Cr<sub>1-x</sub>Al<sub>x</sub>N. Solid squares and open triangle denote stress-strain and energy strain methods, respectively.

The calculated polycrystalline estimates of Young's modulus,  $E$ , and shear modulus,  $G$ , are given in Fig. 5.4b together with bulk modulus,  $B$ . The results from stress-strain and energy-strain methods agree well, which is not surprising given the excellent agreement of the single-crystal elastic constants. Values of the bulk modulus,  $B$ , obtained by the strain-energy method are those derived from the Birch-Murnaghan EOS i.e., those used to obtain the single crystal elastic constants by this method. On the contrary, the strain-stress method allowed us to obtain the single crystal elastic constants without using  $B$  from the EOS, and thus to independent estimate for  $B$ . The fact that the two datasets for  $B$  almost overlap is a proof of the consistency of our calculations. Additionally, the calculated bulk modulus  $B$  for the c-CrN in the PM state shows a good agreement with recent experimental result (257 GPa) [29]. The Young's modulus,  $E$ , and shear modulus,  $G$ , change smoothly and increase with the amount of Al. Both of them show almost a linear dependence on the composition in contrast to an almost practically constant value of  $B$ . By analyzing the hardness of cubic metal mononitrides, Fulcher *et al.* have recently pointed out that the Young's and shear moduli exhibit better correlations with hardness than bulk modulus [30]. Our results confirm this finding also for the case of the Cr<sub>1-x</sub>Al<sub>x</sub>N alloy. Indeed, the majority of experimental results state an indentation hardness increase with Al-content for Cr<sub>1-x</sub>Al<sub>x</sub>N from ~21 GPa [31] for CrN to ~32 GPa for c-Cr<sub>1-x</sub>Al<sub>x</sub>N with Al contents close to the B1/B4 transition [32].

To quantify the elastic anisotropy in the c-Cr<sub>1-x</sub>Al<sub>x</sub>N system, the Zener's anisotropy ratio [33],

$$A=2C_{44}/(C_{11}-C_{12}) \quad (5.8)$$

together with the ratio between the directional Young's modulus  $E_{\langle 111 \rangle}$  and  $E_{\langle 100 \rangle}$  are presented in Fig. 5.5a. The results indicate that the stiffest direction in c-Cr<sub>1-x</sub>Al<sub>x</sub>N changes from  $\langle 100 \rangle$  to  $\langle 111 \rangle$  direction as Al content increases. This is caused by softening of  $C_{11}$ , (weakening of the  $sp^3 d^2$  hybridization) and stiffening of  $C_{44}$  and  $C_{12}$  elastic constants (increasing charge transfer)

with the addition of Al. It is also worth noting that the ratio  $A$  and  $E_{\langle 111 \rangle} / E_{\langle 100 \rangle}$  are close to 1 at certain concentration. Herein highlighted in Fig. 5.5a for the stress-strain method, the isotropic composition is around  $x=0.44$ , while it equals to approximately 0.56 for the energy-strain method. We therefore predict that the directional dependence of Young's modulus almost diminishes for alloys with compositions close to  $\text{Cr}_{0.5}\text{Al}_{0.5}\text{N}$ .

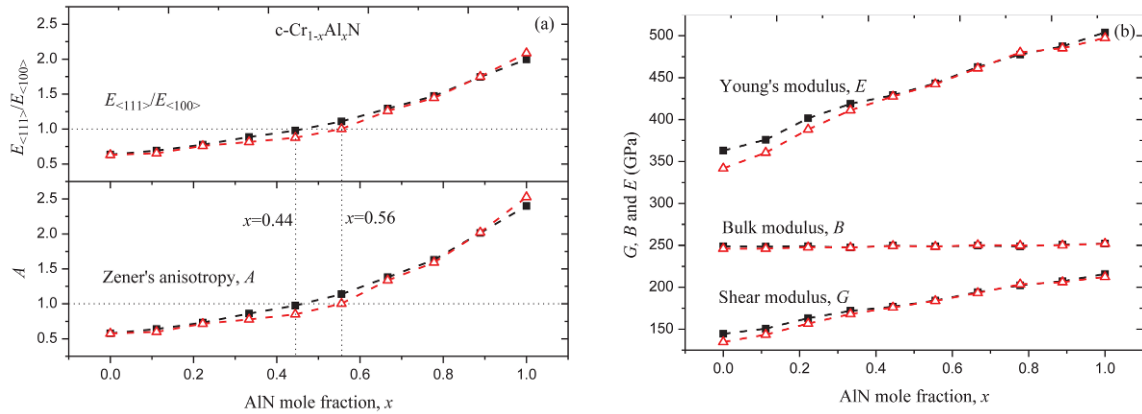


Figure 5.5: (a) Zener's anisotropy,  $A$  and  $E_{\langle 111 \rangle} / E_{\langle 100 \rangle}$  and (b) Poisson ratio  $\nu$ ,  $B/G$  and Cauchy pressure,  $C_{12}-C_{44}$ , of  $c\text{-Cr}_{1-x}\text{Al}_x\text{N}$  in PM state. The values are based on stress-strain (solid square) and energy strain (solid triangle) methods.

Figure 5.5b shows Poisson's ratio,  $\nu$ , and the  $B/G$  ratio as a function of Al content,  $x$ . Frantsevich *et al.* suggested that the Poisson's ratio can be used as an indicator for ductile ( $\nu > 1/3$ ) or brittle behavior ( $\nu < 1/3$ ) [34]. According to this criterion,  $c\text{-Cr}_{1-x}\text{Al}_x\text{N}$  can be regarded as a brittle material, since  $\nu$  is smaller than  $1/3$  over the whole composition range. Another criterion for ductility or brittleness is the value of the  $B/G$  ratio. The higher or lower the  $B/G$  ratio is, the more ductile or brittle the material is, respectively. The critical value which separates ductile and brittle materials is approximately 1.75 [35]. The  $B/G$  ratios calculated from stress-strain and energy-strain methods are again consistent with each other, and are below or close to 1.75. Hence, the  $B/G$  ratio in agreement with the Poisson's ratio criterion, confirms the brittle properties of  $c\text{-Cr}_{1-x}\text{Al}_x\text{N}$  over the whole composition range. The brittleness increases with increasing Al content resulting from gradually weakening of  $d-d$  metallic bonding in the  $c\text{-Cr}_{1-x}\text{Al}_x\text{N}$  with increasing Al content  $x$ .

---

It has been suggested in the literature that the Cauchy pressure [36],  $C_{12} - C_{44}$ , can be used to characterize the bonding type. Negative Cauchy pressure corresponds to more directional bonding, while positive values indicate predominant metallic bonding. The calculated Cauchy pressure for c-Cr<sub>1-x</sub>Al<sub>x</sub>N alloys is presented in the lower panel of Fig. 5.5b. Their values are close to zero or negative in the whole composition range, indicating that the predominant bonding behavior in c-Cr<sub>1-x</sub>Al<sub>x</sub>N alloys is directional. The decreasing Cauchy pressure with increasing Al content indicates a tendency towards stronger directional character of the bonds, which results in an increased resistance against shearing, a result reflected also by the increasing trend in  $C_{44}$ . As explained above, this is a consequence of the gradual change of the hybridization between Cr 3d and N 2p states to the ionic-covalent bonding between Al 3p and N 2p states. Indeed, Litimein *et al.* [27] pointed out that the Al 3s-N 2p hybridization in AlN is stronger than that of transitional metal nitrides due to the proximity of the N 2p and Al 3s orbital energies and also the shorter bond length of AlN, which also can be applied to CrN. In addition, the weak metal-metal *d-d* interaction in CrN is gradually reduced to zero as Al content increases. The stronger Al 3s-N 2p hybridization creates a significant resistance to initializing plastic flow by shear, thus resulting in an increased hardness consequently. Therefore, c-Cr<sub>1-x</sub>Al<sub>x</sub>N coatings with high Al-content are intrinsically harder than the low Al containing alloys.

## 5.4 Conclusions

In this chapter, the equilibrium properties of c-Cr<sub>1-x</sub>Al<sub>x</sub>N are calculated using first principles, indicating that the proper magnetic order (namely the paramagnetic state) cannot be neglected. The elastic properties of c-Cr<sub>1-x</sub>Al<sub>x</sub>N are obtained by two independent methods, the stress-strain and the energy-strain methods, which show an excellent agreement. Using the Hershey model we obtained the compositionally dependent polycrystalline Young's and shear moduli. Both exhibit a strong correlation with hardness, while the bulk modulus  $B$ , being almost constant, seems to be a poor indicator for hardness. The isotropic elastic response of c-Cr<sub>1-x</sub>Al<sub>x</sub>N is predicted for concentrations around  $x=0.50$ . Cubic structured Cr<sub>1-x</sub>Al<sub>x</sub>N is a brittle material in the whole composition range, and its brittleness increases with the Al content. The Cauchy

---

pressure suggests a tendency towards stronger directional character of the bonds as the Al content increases. All the strong compositional dependencies of the elastic response predicted for the c-Cr<sub>1-x</sub>Al<sub>x</sub>N system are closely linked with the changes in the electronic structure and bonding nature. Based on the results obtained we can conclude that high Al containing c-Cr<sub>1-x</sub>Al<sub>x</sub>N coatings are intrinsically harder than their low Al containing counterparts.

---

# References

- [1] S. H. Wei, L. G. Ferreira, J. E. Bernard, and A. Zunger, *Phys. Rev. B* **42**, 9622 (1990).
- [2] A. V. Hershey, *J. Appl. Mech* **21**, 236 (1954).
- [3] F. Tasnádi, M. Odín, and I. A. Abrikosov, *Phys. Rev. B* **85**, 144112 (2012).
- [4] G. Kresse and J. Furthmüller, *Phys. Rev. B* **54**, 11169 (1996).
- [5] G. Kresse and J. Hafner, *Phys. Rev. B* **47**, 558 (1993).
- [6] G. Kresse and D. Joubert, *Phys. Rev. B* **59**, 1758 (1999).
- [7] J. P. Perdew, K. Burke, and M. Ernzerhof, *Phys. Rev. Letters* **77**, 3865 (1996).
- [8] Y. Le Page and P. Saxe, *Phys. Rev. B* **65**, 104104 (2002).
- [9] Y. Le Page and P. Saxe, *Phys. Rev. B* **63**, 174103 (2001).
- [10] D. Holec, M. Friák, J. Neugebauer, and P. H. Mayrhofer, *Phys. Rev. B* **85**, 064101 (2012).
- [11] F. Birch, *Phys. Rev.* **71**, 809 (1947).
- [12] S. Shang, Y. Wang, and Z. K. Liu, *Appl. Phys. Lett.* **90**, 101909 (2007).
- [13] M. Moakher and A. N. Norris, *J. Elasticity* **85**, 215 (2006).
- [14] D. Holec, F. Rovere, P. H. Mayrhofer, and P. B. Barna, *Scripta Mater.* **62**, 349 (2010).
- [15] P. H. Mayrhofer, D. Music, T. Reeswinkel, H. G. Fuß, and J. M. Schneider, *Acta Mater.* **56**, 2469 (2008).
- [16] P. H. Mayrhofer, H. Willmann, and A. E. Reiter, *Surf. Coat. Technol.* **202**, 4935 (2008).
- [17] M. Kawate, A. Kimura, and T. Suzuki, *J. Vac. Sci. Technol., A* **20**, 569 (2002).
- [18] A. Kimura, M. Kawate, H. Hasegawa, and T. Suzuki, *Surf. Coat. Technol.* **169**, 367 (2003).

- 
- [19] Y. Makino and K. Nogi, *Surf. Coat. Technol.* **98**, 1008 (1998).
- [20] D. Holec, R. Rachbauer, L. Chen, L. Wang, D. Luef, and P. H. Mayrhofer, *Surf. Coat. Technol.* **206**, 1698-1704 (2011).
- [21] B. Alling, T. Marten, and I. A. Abrikosov, *Nat. Mater.* **9**, 283 (2010).
- [22] P. Steneteg, B. Alling, and I. A. Abrikosov, *Phys. Rev. B* **85**, 144404 (2012).
- [23] B. Alling, T. Marten, and I. A. Abrikosov, *Phys. Rev. B* **82** (2010).
- [24] J. F. Nye, *Physical Properties of Crystals, Their Representation by Tensors and Matrices* (Oxford University Press, Oxford, 1985).
- [25] F. Tasnádi, I. A. Abrikosov, L. Rogstrom, J. Almer, M. P. Johansson, and M. Odén, *Appl. Phys. Lett.* **97**, 231902 (2010).
- [26] B. Alling, A. Karimi, and I. A. Abrikosov, *Surf. Coat. Technol.* **203**, 883 (2008).
- [27] F. Litimein, B. Bouhafs, Z. Dridi, and P. Ruterana, *New J. Phys.* **4**, 64 (2002).
- [28] D. Holec, R. Rachbauer, D. Kiener, P. D. Cherns, P. M. F. J. Costa, C. McAleese, P. H. Mayrhofer, and C. J. Humphreys, *Phys. Rev. B* **83**, 165122 (2011).
- [29] S. Wang *et al.*, *Phys. Rev. B* **86**, 064111 (2012).
- [30] B. D. Fulcher, X. Y. Cui, B. Delley, and C. Stampfl, *Phys. Rev. B* **85** (2012).
- [31] A. Riedl, R. Daniel, M. Stefenelli, T. Schöberl, O. Kolednik, C. Mitterer, and J. Keckes, *Scripta Mater.*, **67**, 708-711 (2012).
- [32] L. M. Corliss, N. Elliott, and J. M. Hastings, *Phys. Rev.* **117**, 929 (1960).
- [33] S. I. Ranganathan and M. Ostoja-Starzewski, *Phys. Rev. Letters* **101**, 055504 (2008).
- [34] I. N. Frantsevich, F. F. Voronov, and S. A. Bokuta, *Naukova Dumka, Kiev, Elastic*

---

Constants and Elastic Moduli of Metals and Insulators, p. 60 (1983).

[35] S. F. Pugh, *Philos. Mag* **45**, 823 (1954).

[36] D. G. Pettifor, *Materials science and technology* **8**, 345 (1992).

---

# Chapter 6

## Impact of TM elements alloyed in CrN on structural and thermodynamic properties

---

### 6.1 Motivation

As stated in the introduction part, apart from the experimental reports for  $\text{Cr}_{1-x}\text{TM}_x\text{N}$  systems, the theoretical calculations are limited to only  $\text{Cr}_{1-x}\text{Ti}_x\text{N}$  [1]. Recently, plenty of examples have illustrated that a combination of theoretical studies with experimental work represent a successful approach to gain deeper understanding of the material behavior, which can be used in e.g. designing coatings with application tailored properties [2-5]. For this reason, in this chapter, a systematic theoretical study of the alloying effect on the lattice parameters, isostructural mixing enthalpies and ductility of the ternary nitride systems  $\text{Cr}_{1-x}\text{TM}_x\text{N}$  (TM=Sc, Y; Ti, Zr, Hf; V, Nb, Ta; Mo, W) in the cubic B1 structure is investigated using first-principles calculations.

### 6.2 Calculational methods

Density Functional Theory (DFT) based calculations are performed using the Vienna Ab initio Simulation Package (VASP) [6,7]. The ion-electron interactions are described by the projector augmented wave method (PAW) [8] and the generalized gradient approximation (GGA) is employed for the exchange-correction effects, as parameterized by Perdew–Burke–Ernzerhof (PBE) [9].

In order to simulate the chemical disorder between Cr and TM atoms on the metal sublattice of the cubic B1 structure (NaCl prototype, space group  $Fm\bar{3}m$ ), and also the paramagnetic state induced by Cr atoms, we use the special quasi-random structures (SQS) [10]

approach as implemented in our recent study of  $\text{Cr}_{1-x}\text{Al}_x\text{N}$  system [11].  $3\times 3\times 2$  supercells (36 atoms) described in detail in Ref. [11] are used for the  $\text{Cr}_{1-x}\text{TM}_x\text{N}$ . Mixing of  $\text{Cr}^\uparrow$ ,  $\text{Cr}^\downarrow$  and TM atoms takes place on one sublattice while the other sublattice is fully occupied with N atoms. The short range order parameters (SROs) are optimized for pairs at least up to the fifth order. The alloying effect on the ductility has been assessed by evaluating elastic properties of  $\text{Cr}_{0.89}\text{TM}_{0.11}\text{N}$  using stress-strain method [11]. All the calculations are performed with plane wave cutoff energy of 500 eV together with  $6\times 6\times 9$  Monkhorst-Pack  $k$ -point meshes, which guarantee the total energy accuracy in the order of meV per atom.

## 6.3 Results and discussion

### 6.3.1 Structural properties

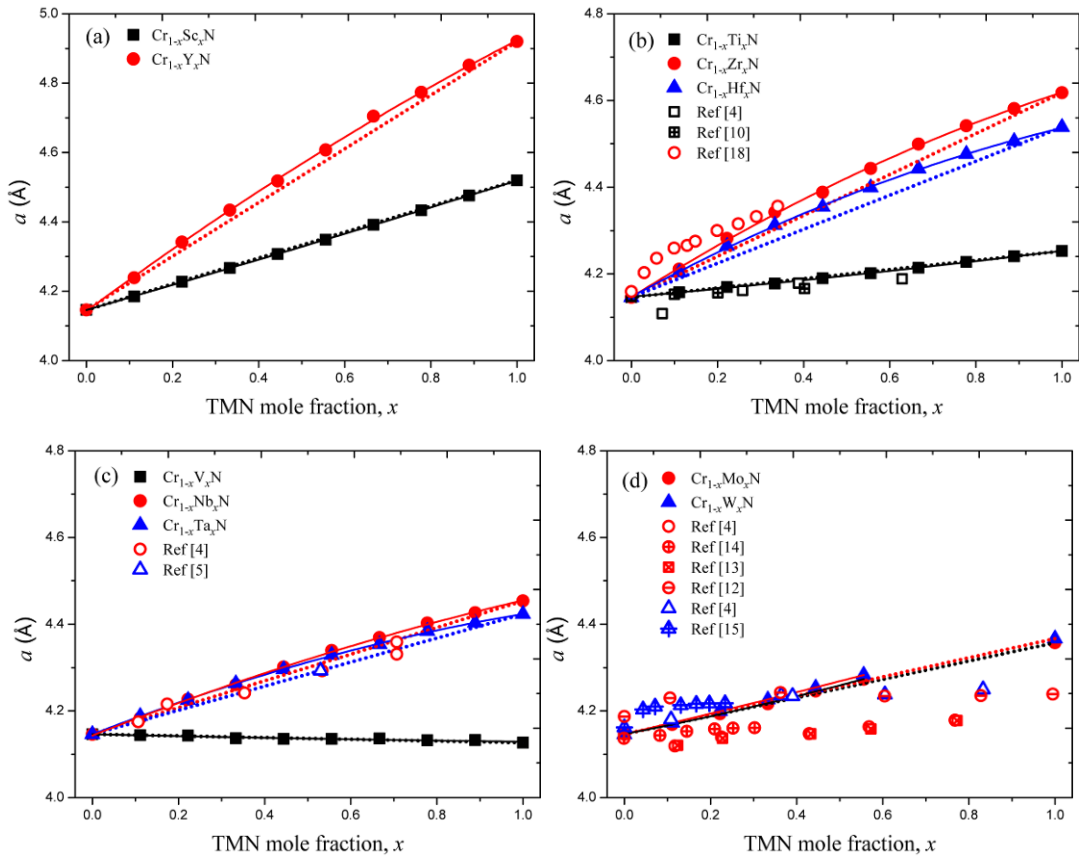


Figure 6.1: Calculated equilibrium lattice parameters in comparing with experimental results for  $\text{Cr}_{1-x}\text{TM}_x\text{N}$  (TM=Sc, Y, Ti, Zr, Hf, V, Nb, Ta, Mo and W) solid solutions as a function of TMN content. The dotted lines indicate Vegard's linear behavior. Open symbols correspond to

the experimental data. The Figure is divided into a, b, c, and d, according to the TM groups, IIIB, IVB, VB, and VIB, respectively.

The supercell volume and shape, as well as internal atomic positions are optimized with respect to total energy in order to obtain equilibrium properties of cubic B1  $\text{Cr}_{1-x}\text{TM}_x\text{N}$  solid solutions using the Birch–Murnaghan equation of state [12]. The resulting lattice parameters for  $\text{Cr}_{1-x}\text{TM}_x\text{N}$  phases are shown in Fig. 6.1. Please note that Fig. 6.1 is divided into a, b, c, and d, according to the TM groups, IIIB, IVB, VB, and VIB, respectively. The calculated values are fitted with a quadratic polynomial:

$$a(x) = xa_{\text{TMN}} + (1-x)a_{\text{CrN}} + bx(1-x) \quad (1)$$

where  $b$  is a bowing parameter describing the deviation from linear, Vegard’s-like behavior [13]. The bowing parameter,  $b$ , for each  $\text{Cr}_{1-x}\text{TM}_x\text{N}$  system together with the optimized lattice constants,  $a_0$ , their experimental values,  $a_{\text{exp}}$ , for comparison [14,15], and energies of formation,  $E_f$ , for TMN compounds are listed in Table 6.1.

Table 6.1: The bowing parameters,  $b$ , for each cubic  $\text{Cr}_{1-x}\text{TM}_x\text{N}$  phase together with the optimized lattice constants  $a_0$ , experimental values,  $a_{\text{exp}}$ , and formation energies,  $E_f$  and VEC for different binary cubic TM compounds (TM = Sc, Y, Ti, Zr, Hf, V, Nb, Ta, Cr, Mo and W).

	$b$ (Å)	$a_0$ (Å)	$a_{\text{exp}}$ (Å) [14-15]	$E_f$ (eV/atom)	VEC
ScN	-0.018	4.520	4.440	-1.923	8
YN	0.138	4.921	4.894	-1.698	8
TiN	-0.017	4.253	4.241	-1.727	9
ZrN	0.155	4.618	4.578	-1.686	9
HfN	0.152	4.538	4.525	-1.758	9

---

VN	-0.005	4.127	4.139	-0.983	10
NbN	0.079	4.454	4.389	-0.874	10
TaN	0.110	4.423	4.358	-0.854	10
CrN		4.146	4.135	-0.441	11
MoN	-0.062	4.357	4.340	0.025	11
WN	-0.024	4.367	4.250	0.329	11

---

The calculated lattice parameters result in slightly larger values than the experimental ones (with the exception of VN), which is expected behavior for DFT-GGA calculation. Good agreement with previous theoretical calculations [16,17] is also obtained. One should notice that the experimental lattice constants of cubic B1 MoN and WN denote the lattice constants of their substoichiometric N-deficient configurations, as the stoichiometric configurations are mechanically unstable [18,19]. Energies of formation in Table 6.1 express the total energy difference between the binary nitride and the corresponding elements in their ground-state configurations (crystalline TM or N<sub>2</sub> molecule). The thus obtained trends are the same as reported before by Rovere *et al.* and Holec *et al.* [16,17].  $E_f$  becomes less negative as the valence electron concentration (VEC) of TM increases. The positive energies of formation of MoN and WN further illustrate their instability.

The bowing parameters,  $b$ , for the Cr<sub>1-x</sub>TM<sub>x</sub>N (TM=Y, Zr, Hf, Nb and Ta) solid solutions have positive values, which denotes a positive deviation (i.e., to large values) from Vegard's linear interpolation. A positive deviation can be qualitatively rationalized in these cases where the lattice spacings of the constituents are very different. Compressing the larger compound is energetically more costly than to expand the smaller one, due to the anharmonicity of the binding energy curve [20]. For other Cr<sub>1-x</sub>TM<sub>x</sub>N (TM=Sc, Ti, V, Mo and W) solid solutions, the bowing parameters show small negative values. This negative deviation from Vegard's linear

---

interpolation is caused by the stronger interatomic bonds connected with an ordering tendency, hence decreasing the lattice parameter for the intermediate compositions. Especially, the lattice parameters of  $\text{Cr}_{1-x}\text{Sc}_x\text{N}$ ,  $\text{Cr}_{1-x}\text{Ti}_x\text{N}$  and  $\text{Cr}_{1-x}\text{V}_x\text{N}$  show almost a linear behavior, which can be ascribed to the same  $sp^3d^2$  hybridization in the 3d group TMNs, consisting of two 3d and one s electrons from TM site and three 2p electrons donated by nitrogen atom. Comparing the calculated lattice parameters with the experimental data yields good agreement for  $\text{Cr}_{1-x}\text{TM}_x\text{N}$  (TM=Zr, Ti, Ta and Nb). In the case of  $\text{Cr}_{1-x}\text{Zr}_x\text{N}$ , the experimental data of Kim *et al.* [21] confirm our predictions for positive bowing of the  $\text{Cr}_{1-x}\text{Zr}_x\text{N}$  lattice parameter, although the deviation from the Vegard's line predicted here seems to be smaller than that observed experimentally. This disagreement could be caused by residual stresses present in the thin films. The calculated lattice parameters of  $\text{Cr}_{1-x}\text{Ti}_x\text{N}$ ,  $\text{Cr}_{1-x}\text{Nb}_x\text{N}$  and  $\text{Cr}_{1-x}\text{Ta}_x\text{N}$  agree well with the experimentally observed values [22-24], aside from the fact that the calculated values always show slightly larger values than the experimental ones. In addition to the overestimation of lattice constants with respect to experiment when GGA is used, substoichiometry of nitrogen reported in the experiment might be an important factor. Panel (d) in Fig. 6.1 shows the optimized lattice parameters of  $\text{Cr}_{1-x}\text{Mo}_x\text{N}$  and  $\text{Cr}_{1-x}\text{W}_x\text{N}$  solid solutions in comparison with experimental data [22,25-28]. Because of the mechanical instability of cubic B1 MoN and WN, only the calculated results for the TM content  $x$  between 0 to 0.56 are presented. It follows that the calculated lattice parameters of  $\text{Cr}_{1-x}\text{Mo}_x\text{N}$  and  $\text{Cr}_{1-x}\text{W}_x\text{N}$  solid solutions are very close to each other. The lattice parameters near TM-rich side agree well with experimental measurements, but the difference between theoretical and experimental results increases as TM content increases. This is more prominent for  $\text{Cr}_{1-x}\text{Mo}_x\text{N}$ . Such behavior can be explained by large substoichiometry of nitrogen in  $\text{Cr}_{1-x}\text{Mo}_x\text{N}$  and  $\text{Cr}_{1-x}\text{W}_x\text{N}$  solid solutions as it has been reported [22]. Finally, no experimental data are available for the lattice parameters of ternary  $\text{Cr}_{1-x}\text{TM}_x\text{N}$  (TM=Sc, Y, Hf and V) solid solutions, which we report here for the first time. The knowledge of lattice parameters of nitrides as given in Table 6.1 and Fig. 6.1, provides useful information for designing coatings and for interpretation of experimental results.

### 6.3.2 Phase stability

The isostructural mixing enthalpy,  $H_{\text{mix}}$ , as a function of TMN content in each cubic B1  $\text{Cr}_{1-x}\text{TM}_x\text{N}$  solid solution is calculated as:

$$H_{\text{mix}} = E(\text{Cr}_{1-x}\text{TM}_x\text{N}) - x E(\text{TMN}) - (1-x) E(\text{CrN}) \quad (2)$$

where  $E(\text{XN})$  and  $E(\text{Cr}_{1-x}\text{TM}_x\text{N})$  are the total energy of binary cubic XN and ternary  $\text{Cr}_{1-x}\text{TM}_x\text{N}$ , respectively.

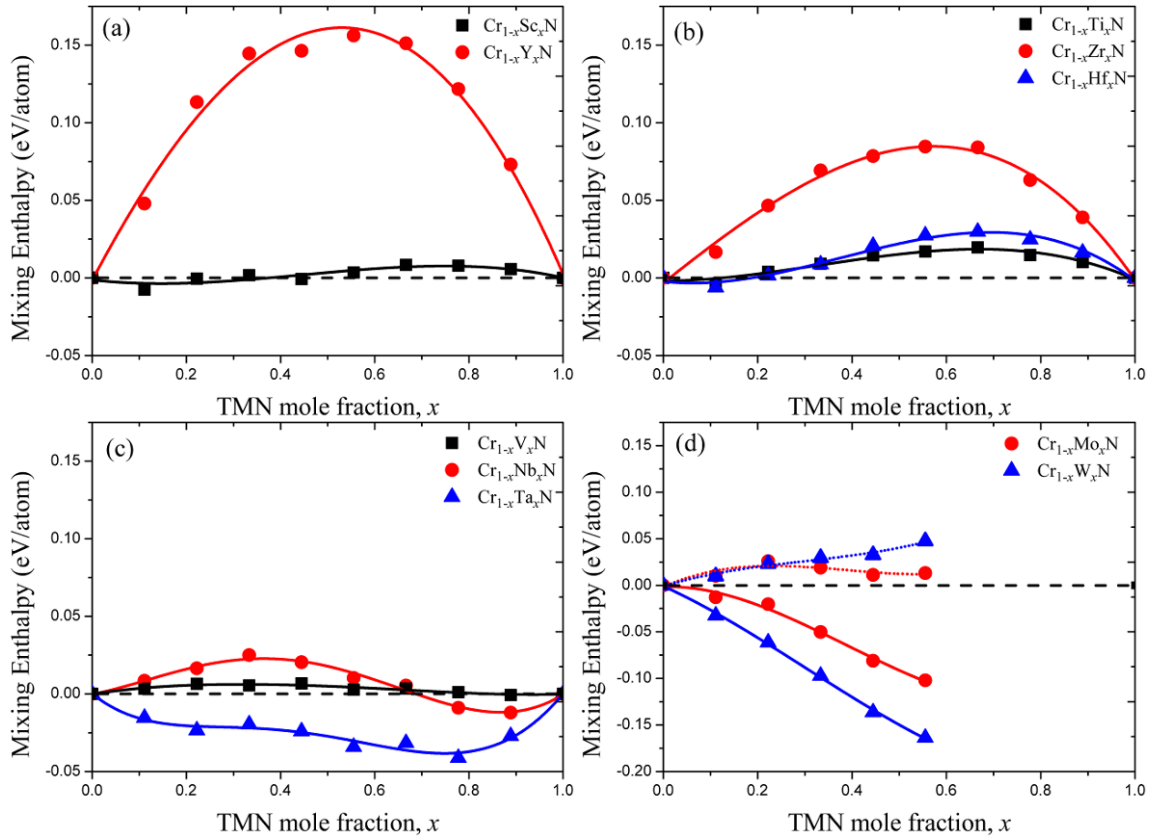


Figure 6.2: Calculated isostructural mixing enthalpy of  $\text{Cr}_{1-x}\text{TM}_x\text{N}$  (TM=Sc, Y, Ti, Zr, Hf, V, Nb, Ta, Mo, and W) solid solutions as a function of TMN content. The Figure is divided into a, b, c, and d, according to the TM groups, IIIB, IVB, VB, and VIB, respectively.

Figure 6.2 summarizes the calculated mixing enthalpies of the  $\text{Cr}_{1-x}\text{TM}_x\text{N}$  solid solutions. Please note that Fig. 6.2 is divided into a, b, c, and d, according to the TM groups, IIIB, IVB, VB, and VIB, respectively. Compared with other  $\text{Cr}_{1-x}\text{TM}_x\text{N}$  solid solutions,  $\text{Cr}_{1-x}\text{Y}_x\text{N}$  displays much

---

larger positive mixing enthalpy with a maximum value of about 0.16 eV/atom at  $x \approx 0.55$ , indicating a thermodynamic driving force for phase separation into its binary constituents. Recently, Rovere *et al.* [4] reported a considerably larger maximum mixing enthalpy of 0.24 eV/atom, which is likely to be a supercell size effect already which has been pointed out by Žukauskaitė *et al.* [29]. The large positive values of  $H_{\text{mix}}$  are the consequence of the large lattice mismatch of YN and CrN, as shown in Fig. 6.1a. Hence,  $\text{Cr}_{1-x}\text{Y}_x\text{N}$  will not tend to mix under realistic equilibrium conditions. On the other hand, the mixing enthalpies of  $\text{Cr}_{1-x}\text{Sc}_x\text{N}$  exhibit values very close to zero. The prominently different behavior for the mixing enthalpies between isoelectronic  $\text{Cr}_{1-x}\text{Y}_x\text{N}$  and  $\text{Cr}_{1-x}\text{Sc}_x\text{N}$  can be traced down to an interplay between lattice mismatch and the electronic effect. The bonding in the TMN can be divided into the hybridized  $sp^3d^2$ , N-*p*-TM-*d* interaction and metal-metal *d-d* bonding [11,30]. The stability is related to the extent of the populated nonbonding or antibonding states as reflected by the density of states (DOS) at Fermi level ( $E_F$ ) [3,17]. High DOS at  $E_F$  suggests an increasing destabilizing effect due to the population of energetically unfavorable states. In the case of ScN [31] and YN [29] where small band gap can be found at  $E_F$ , while negligible DOS or small gap at  $E_F$  depending on the exchange-correlation functional in CrN [1] is ascribed to the magnetic spin polarization of spin-up and spin-down states. Hence, the addition of Y [4] and Sc into CrN has a stabilizing effect for the CrN due to depletion of non-bonding or antibonding states. This electronic stabilizing effect is compensated or overcompensated by the lattice strain in the  $\text{Cr}_{1-x}\text{Sc}_x\text{N}$  or  $\text{Cr}_{1-x}\text{Y}_x\text{N}$ , respectively, resulting in near-to-zero mixing enthalpies of  $\text{Cr}_{1-x}\text{Sc}_x\text{N}$ , and large positive mixing enthalpies in the  $\text{Cr}_{1-x}\text{Y}_x\text{N}$  solid solution.

The mixing enthalpy of  $\text{Cr}_{1-x}\text{Zr}_x\text{N}$  is much larger than that of  $\text{Cr}_{1-x}\text{Ti}_x\text{N}$  and  $\text{Cr}_{1-x}\text{Hf}_x\text{N}$  in addition to a strongly asymmetric shape, see Fig. 6.2b. The maximum values are close to 0.08, 0.03 and 0.02 eV/atom for  $\text{Cr}_{1-x}\text{Zr}_x\text{N}$ ,  $\text{Cr}_{1-x}\text{Hf}_x\text{N}$  and  $\text{Cr}_{1-x}\text{Ti}_x\text{N}$ , respectively, at a TM content around 0.6. It becomes obvious that the larger lattice mismatch between ZrN and CrN as compared with CrN-TiN and CrN-HfN is responsible for the large positive mixing enthalpies of  $\text{Cr}_{1-x}\text{Zr}_x\text{N}$ . In contrast with the electronic stabilizing effect of Sc and Y, the addition of IV, V and VI B group TM elements into CrN causes destabilization effect due to the surplus *d* electrons

---

localized at TM sites, which results in increasing of DOS at  $E_F$  and consequently large electronic driving force for decomposition at high TM content.  $\text{Cr}_{1-x}\text{V}_x\text{N}$  displays similar magnitude of mixing enthalpies close to zero as one can see in Fig. 6.2c, which is ascribed to the electronic destabilizing effect counteracted by the much smaller lattice mismatch between VN and CrN.  $\text{Cr}_{1-x}\text{Ta}_x\text{N}$  is the only system in the present study displaying negative  $H_{\text{mix}}$  in the full compositional range, indicating TaN and CrN binaries are soluble. However, one should be careful about interpreting the absolute values of  $H_{\text{mix}}$ . The cubic B1 structures are only metastable states of NbN and TaN. When the thermodynamical ground state of TaN i.e., the hexagonal  $B_h$  structure (TaN prototype, space group  $P6/mmm$ ), is taken as a reference state, positive values of  $H_{\text{mix}}$  are obtained also for  $\text{Cr}_{1-x}\text{Ta}_x\text{N}$ . This indicates that the system is actually thermodynamically unstable, but the decomposition is unlikely to proceed via spinodal process (i.e., decomposition into cubic Cr- and Ta-rich phases).

In the case of  $\text{Cr}_{1-x}\text{Mo}_x\text{N}$  and  $\text{Cr}_{1-x}\text{W}_x\text{N}$  solid solutions, only results in a limited compositional range are presented here. In Fig. 6.2d, two different sets of reference states for calculating the mixing enthalpy of  $\text{Cr}_{1-x}\text{Mo}_x\text{N}$  and  $\text{Cr}_{1-x}\text{W}_x\text{N}$  are chosen. The solid lines denote the mixing enthalpy with cubic CrN and TMN as the reference states, while the dotted lines denote mixing enthalpy with respect to CrN and  $\text{TM}_2\text{N}+\text{N}_2$ . From Fig. 6.3d, one can see that the mixing enthalpies of  $\text{Cr}_{1-x}\text{TM}_x\text{N}$  calculated with respect to cubic B1 CrN and TMN show more negative values as TM content increases, which suggests increasing stability of these ternary alloys. However, it has been experimentally demonstrated that the deposited  $\text{Cr}_{1-x}\text{Mo}_x\text{N}$  and  $\text{Cr}_{1-x}\text{W}_x\text{N}$  coatings are mixtures of CrN and  $\text{TM}_2\text{N}$  (TM=Mo and W) [32]. In fact, substoichiometry of nitrogen is always experimentally observed in  $\text{Cr}_{1-x}\text{Mo}_x\text{N}$  and  $\text{Cr}_{1-x}\text{W}_x\text{N}$  solid solutions, and also the stable cubic  $\gamma\text{-Mo}_2\text{N}$  and  $\gamma\text{-W}_2\text{N}$  compounds can be detected in the deposited coatings. We therefore suggest that using CrN+ $\text{TM}_2\text{N}+\text{N}_2$  as reference states is more meaningful. The mixing enthalpies of  $\text{Cr}_{1-x}\text{Mo}_x\text{N}$  and  $\text{Cr}_{1-x}\text{W}_x\text{N}$  with respect to CrN+ $\text{TM}_2\text{N}+\text{N}_2$  have positive values (see Fig. 6.2d), which denotes the possibility for isostructural decomposition, and is consistent with the experimental findings [32]. More detailed results on  $\text{Cr}_{1-x}\text{TM}_x\text{N}_{1-y}$  will be presented elsewhere.

### 6.3.3 Alloying influence on mechanical behavior

In order for evaluating the alloying effect on the ductility, the bulk-to-shear modulus ratio,  $B/G$ , and also Cauchy pressure,  $C_{12}-C_{44}$ , as a function of valence electron concentration (VEC) are plotted in Fig. 6.3.

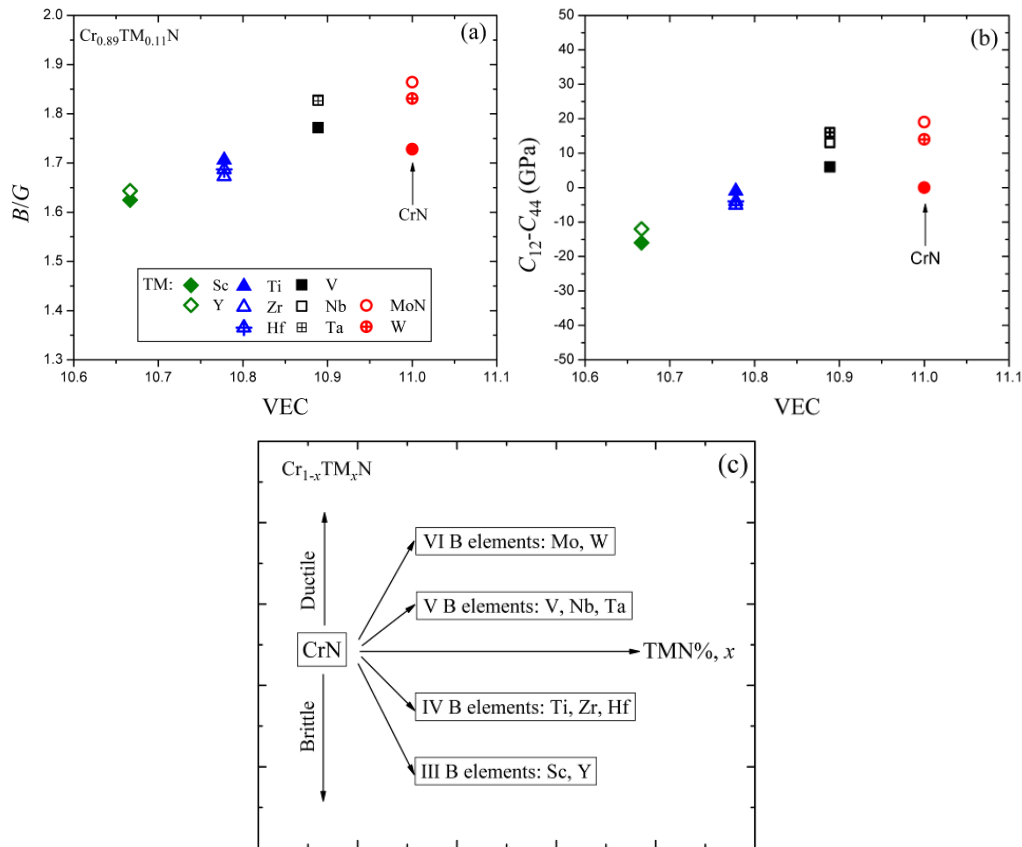


Figure 6.3: (a) The bulk to shear modulus ratio,  $B/G$ , versus VEC, (b) VEC effect on Cauchy pressure,  $C_{12}-C_{44}$ , in CrN based nitrides, and (c) the alloying-related trends in ductility of  $\text{Cr}_{1-x}\text{TM}_x\text{N}$  as functions of TM elements and also TM content. The red solid circle denotes CrN.

VEC is calculated as an average value of valence electrons per formula unit. According to Pugh *et al.* [33], the higher or lower the  $B/G$  ratio is, the more ductile or brittle the material is, respectively. The critical value which separates ductile and brittle materials is approximately 1.75. Figure 6.3a demonstrates that the  $B/G$  ratio of the ternary  $\text{Cr}_{0.89}\text{TM}_{0.11}\text{N}$  solid solutions increases as the VEC increases, which has the same trend with another similar coating system TiTMN. The alloying effect is evaluated through comparing the  $B/G$  ratio of  $\text{Cr}_{0.89}\text{TM}_{0.11}\text{N}$

---

with that of CrN. It is clear that adding small amounts of V, Nb, Ta, Mo and W into CrN coatings will increase  $B/G$  ratio above 1.75, which denotes the improved ductility. The Cauchy pressure,  $C_{12}-C_{44}$ , can be used to characterize the bonding type [34]. Negative Cauchy pressure corresponds to more directional, while positive values indicate predominant metallic bonding. As the VEC is increased, Cauchy pressure values are increased, which is obviously showing the same trend with  $B/G$  ratio for the  $\text{Cr}_{0.89}\text{TM}_{0.11}\text{N}$  and suggests the gradual changes in the bonding from directional bonding towards metallic bonding type. A comparison of CrN with  $\text{Cr}_{0.89}\text{TM}_{0.11}\text{N}$  yields that alloying V, Nb, Ta, Mo, and W increases the metal-metal  $d-d$  orbital hybridization, which is responsible for more ductile behavior, similarly to another system TiTMN [5]. Based on the trends for the  $B/G$  ratio and Cauchy pressure,  $C_{12}-C_{44}$ , the promising candidates for improving ductility by alloying include V, Nb, Ta, Mo, and W. Figure. 6.3c summaries qualitatively the alloying trends on mechanical behavior of CrN, and as such can be used as a guide for tailoring the coating properties.

## 6.4 Conclusions

In this chapter, a systematic study of the TM-alloying effect to CrN coatings on the lattice parameters, isostructural mixing enthalpies and mechanical properties has been performed using first-principles calculations. The bowing parameters for the lattice parameters of  $\text{Cr}_{1-x}\text{TM}_x\text{N}$  (TM=Sc, Y; Ti, Zr, Hf; V, Nb, Ta; Mo, W) in the cubic B1 structure are obtained and the positive deviation from Vegard's linear behavior has been found for  $\text{Cr}_{1-x}\text{TM}_x\text{N}$  (TM=Y; Zr, Hf; Nb, Ta) solid solutions, while  $\text{Cr}_{1-x}\text{TM}_x\text{N}$  (TM=Sc; Ti; V; Mo, W) solid solutions show a negative bowing. The large lattice mismatch between CrN and YN induces maximum mixing enthalpy of  $\text{Cr}_{1-x}\text{Y}_x\text{N}$  and finally results in a strong preference for phase separation, while  $\text{Cr}_{1-x}\text{Ta}_x\text{N}$  shows a negative mixing enthalpy in the whole compositional range, indicating that TaN and CrN binaries are miscible.  $\text{Cr}_{1-x}\text{Sc}_x\text{N}$  and  $\text{Cr}_{1-x}\text{V}_x\text{N}$  have their mixing enthalpy close to zero due to the mutual compensation between electronic effect and the lattice strain. The  $B/G$  ratio and Cauchy pressure,  $C_{12}-C_{44}$ , of the ternary  $\text{Cr}_{0.89}\text{TM}_{0.11}\text{N}$  solid solutions show a strong dependence on valence electron concentration. V, Nb, Ta, Mo, and W have been shown to be

---

promising candidates for improving ductility of CrN, which is the result of increasing metal-metal *d-d* orbital hybridization.

---

## References

- [1] B. Alling, Phys. Rev. B **82**, 054408 (2010).
- [2] P. H. Mayrhofer, D. Music, T. Reeswinkel, H. G. Fuß and J. M. Schneider, Acta Mater. **56**, 2469 (2008).
- [3] B. Alling, A. Karimi, and I. A. Abrikosov, Surf. Coat. Technol. **203**, 883 (2008).
- [4] F. Rovere, D. Music, J. M. Schneider, and P. H. Mayrhofer, Acta Mater. **58**, 2708 (2010).
- [5] D. G. Sangiovanni, V. Chirita, and L. Hultman, Phys. Rev. B **81**, 104107 (2010).
- [6] G. Kresse and J. Furthmüller, Phys. Rev. B **54**, 11169 (1996).
- [7] G. Kresse and J. Hafner, Phys. Rev. B **47**, 558 (1993).
- [8] G. Kresse and D. Joubert, Phys. Rev. B **59**, 1758 (1999).
- [9] J. P. Perdew, K. Burke, and M. Ernzerhof, Phys. Rev. Lett. **77**, 3865 (1996).
- [10] S. H. Wei, L. G. Ferreira, J. E. Bernard, and A. Zunger, Phys. Rev. B **42**, 9622 (1990).
- [11] L. Zhou, D. Holec, and P. H. Mayrhofer, J. Appl. Phys. **113**, 043511 (2013).
- [12] F. Birch, Phys. Rev. **71**, 809 (1947).
- [13] L. Vegard, Z. Phys. Chem. **5**, 17 (1921).
- [14] Powder diffraction files 00-045-0978 (ScN), 00-035-0779 (YN), 03-065-0565 (TiN), 00-035-0753 (ZrN), 00-033-0592 (HfN), 00-035-0768 (VN), 03-065-5011 (NbN), 03-065-9404 (TaN), 00-065-2899 (CrN), International center for diffraction data, PDF-2/release 2007
- [15] L. E. Koutsokeras, G. M. Matenoglou, and P. Patsalas, Thin Solid Films **528**, 49 (2013).
- [16] D. Holec, M. Friák, J. Neugebauer, and P. H. Mayrhofer, Phys. Rev. B **85** (2012).
- [17] F. Rovere, D. Music, S. Ershov, M. T. Baben, H. G. Fuss, P. H. Mayrhofer, and J. M. Schneider, J. Phys. D: Appl. Phys. **43**, 035302 (2010).
- [18] W. Chen and J. Z. Jiang, J. Alloys Compd. **499**, 243 (2010).
- [19] M. B. Kanoun, S. Goumri-Said, and M. Jaouen, Phys. Rev. B **76**, 134109 (2007).
- [20] B. Alling, C. Höglund, R. Hall-Wilton, and L. Hultman, Appl. Phys. Lett. **98**, 241911 (2011).
- [21] G. Kim, B. Kim, S. Lee, and J. Hahn, Surf. Coat. Technol. **200**, 1669 (2005).

- 
- [22] P. Hones, R. Sanjin , and F. L y, *Thin Solid Films* **332**, 240 (1998).
- [23] X. Jin, L. Gao, and J. Sun, *Acta Mater.* **54**, 4035 (2006).
- [24] Y. I. Chen, K. Y. Lin, and C. C. Chou, *Thin Solid Films.* **544**, 606–611 (2013).
- [25] B. S. Yau, C. W. Chu, D. Lin, W. Lee, J. G. Duh, and C. H. Lin, *Thin Solid Films* **516**, 1877 (2008).
- [26] P. Hones, M. Diserens, R. Sanjin , and F. L y, *J. Vac. Sci. Technol., B* **18**, 2851 (2000).
- [27] K. Ho Kim, E. Young Choi, S. Gyun Hong, B. Gyu Park, J. Hong Yoon, and J. Hae Yong, *Surf. Coat. Technol.* **201**, 4068 (2006).
- [28] P. Hones, R. Sanjin , F. L y, and O. Shojaei, *J. Vac. Sci. Technol., A* **17**, 1024 (1999).
- [29] . Agn *et al.*, *J. Phys. D: Appl. Phys.* **45**, 422001 (2012).
- [30] D. Holec, R. Rachbauer, L. Chen, L. Wang, D. Luef, and P. H. Mayrhofer, *Surf. Coat. Technol.* **206**, 1698 (2011).
- [31] S. Kerdsonpanya, B. Alling, and P. Eklund, *Phys. Rev. B* **86**, 195140 (2012).
- [32] B. Gu, J. P. Tu, X. H. Zheng, Y. Z. Yang, and S. M. Peng, *Surf. Coat. Technol.* **202**, 2189 (2008).
- [33] S. F. Pugh, *Philos. Mag.* **45**, 823 (1954).
- [34] D. G. Pettifor, *Mater. Sci. Technol.* **8**, 345 (1992).

---

# Chapter 7

## Off-stoichiometry in $\text{Cr}_{1-x}\text{TM}_x\text{N}_y$ (TM=Mo and W)

---

### 7.1 Motivation

The significant deviation for the lattice parameters of cubic  $\text{Cr}_{1-x}\text{TM}_x\text{N}$  (TM = Mo or W) between theoretical and experimental data in our previous chapter 6, suggests that the vacancies in these cubic  $\text{Cr}_{1-x}\text{TM}_x\text{N}$  solid solutions play an indispensable and significant role. In order to clarify these controversies and the debated results in literature, as stated in the introduction part, in this chapter, we have performed a comprehensive investigation on understoichiometric cubic  $\text{Cr}_{1-x}\text{Mo}_x\text{N}_y$  and  $\text{Cr}_{1-x}\text{W}_x\text{N}_y$  solid solutions by the evaluation of the structural and mechanical properties using first-principles calculations. The results are compared with experimentally obtained lattice parameters of sputter deposited  $\text{Cr}_{1-x}\text{Mo}_x\text{N}_y$  coatings.

### 7.2 Methods

#### 7.2.1 Calculation details

Density Functional Theory (DFT) based calculations are performed using the Vienna Ab initio Simulation Package (VASP) [19, 20]. The ion-electron interactions are described by the projector augmented wave method (PAW) [21] and the generalized gradient approximation (GGA) as parameterized by Perdew–Burke–Ernzerhof (PBE) [22] is employed for the exchange-correction effects.

In order to simulate the chemical disorder between Cr and TM atoms on the metal sublattice of the cubic B1 structure, and also the paramagnetic state induced by Cr atoms, we used the

---

Special Quasi-random Structures (SQS) approach [23] as implemented and tested in our previous studied CrN-based systems [6, 24, 25]. The content of nitrogen vacancies is assumed to be dependent on the composition of  $\gamma$ -TM<sub>2</sub>N, and the chemical formula Cr<sub>1-x</sub>TM<sub>x</sub>N<sub>1-0.5x</sub> (a linear combination of cubic B1-CrN and  $\gamma$ -TM<sub>2</sub>N) is used to describe the cubic (Cr, TM)N solid solutions. The full compositional profile for the nitrogen vacancies, i.e., varying Cr/TM ratio on the metal sublattice and vacancy content on the nitrogen sublattice (which is similar to Refs. [26, 27]), was not accounted for. This is due to the fact that it is very difficult to incorporate more nitrogen atoms into vacant octahedral sites in  $\gamma$ -TM<sub>2</sub>N [18, 28]. 2x2x2 supercells containing 64 atoms are used for the Cr<sub>1-x</sub>TM<sub>x</sub>N<sub>1-0.5x</sub> in the present work. The short range order parameters (SROs) are optimized for pairs at least up to the fifth coordination shell. The stress-strain method used in our previous work [6, 25] is employed to evaluate the elastic properties of Cr<sub>1-x</sub>TM<sub>x</sub>N<sub>1-0.5x</sub>. Monkhorst-Pack grids [29] of 5x5x5 *k*-point mesh is used for the 64-atoms supercells. All the calculations were performed with plane wave cutoff energy of 500 eV, hence guaranteeing with an accuracy in the order of meV per atom.

## 7.2.2 Experimental details

All coatings in this study were deposited using a modified DC magnetron sputtering system Leybold Heraeus Z400. In order to vary the chemical composition, cubes of Cr (99.99% purity, 3x3x3mm) were uniformly arranged on the race track of a Mo target (99.99% purity and 75 mm in diameter), and reactively sputtered in a mixed N<sub>2</sub>/Ar atmosphere onto single crystal silicon (100) and austenite substrates. Before the deposition, the chamber was evacuated to a high vacuum of  $5 \cdot 10^{-4}$  Pa, and a constant total pressure of 0.35 Pa was kept during all sputtering processes. The substrate temperature of  $450 \pm 20$  °C guaranteed for a dense columnar growth microstructure. This temperature regime corresponds to an homologous temperature  $T/T_m \sim 0.3$  [30] and thus belongs to the transition zone T according to Thornton's zone model [31]. The glow discharge current was set to 0.4 A.

Phase analyses were performed using an X-ray diffractometer Philips X'Pert with monochromized Cu  $K_\alpha$  radiation. The lattice constants were obtained by fitting the peak positions in the diffraction patterns, which are recorded in Bragg-Brentano geometry.

Elemental composition was determined by means of energy dispersive X-ray spectroscopy (EDXS) using a FEI Quanta 200 FEGSEM scanning electron microscope equipped with a Schottky emitter, which provides an excellent spatial resolution of about 2 nm. Indentation moduli were measured with a UMIS unit using a Berkovich diamond tip and applying loads between 3 and 45 mN. The Young's moduli were evaluated according to the procedure after Oliver and Pharr [32], and plotted as a function of the penetration depth. The best estimation of the film-only elastic modulus can be achieved by extrapolating the measured data back to a zero penetration depth [33]. In order to verify the obtained results of the elastic moduli, series of measurements were carried out on different reference samples with well-known values of Young's modulus. The coatings on austenite substrates were used due to the better adhesion, since even microscopic delamination will influence the evaluation of the Young's modulus.

### 7.3 Results and discussion

Figure 7.1 presents the crystal structures of cubic B1-CrN,  $\gamma$ -TM<sub>2</sub>N (TM = Mo and W),  $\beta$ -TM<sub>2</sub>N, and t-TM<sub>2</sub>N.  $\gamma$ -TM<sub>2</sub>N has a defective cubic B1 structure with 50% disordered vacancies in the nitrogen sublattice [34].

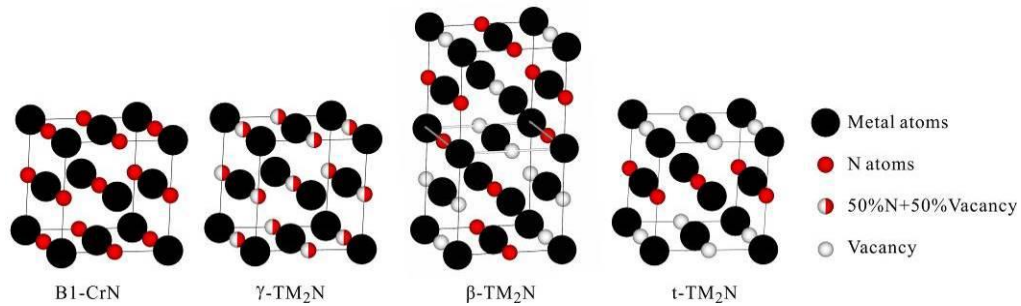


Figure 7.1: Crystallographic structures of cubic B1-CrN,  $\gamma$ -TM<sub>2</sub>N,  $\beta$ -TM<sub>2</sub>N, and t-TM<sub>2</sub>N.

Table 7.1: Calculated total energy,  $E_{total}$  (eV/atom), lattice parameter,  $a$  (Å), volume per atom  $V$  (Å<sup>3</sup>/atom), and bulk modulus,  $B$  (GPa). The experimental data is presented for comparison.

	$\gamma$ -Mo <sub>32</sub> N <sub>16</sub>	$\beta$ -Mo <sub>2</sub> N	t-Mo <sub>2</sub> N	$\gamma$ -Mo <sub>2</sub> N	$\gamma$ -W <sub>32</sub> N <sub>16</sub>	$\beta$ -W <sub>2</sub> N	t-W <sub>2</sub> N	$\gamma$ -W <sub>2</sub> N
$E_{total}$	-10.213	-10.248	-10.191		-11.472	-11.481	-11.406	

		$a=4.27$	$a=4.22$		$a=4.30$	$a=4.22$		
$a, b, c$	$a=4.19$	$c=8.04$	$c=4.18$	4.16 [34]	$a=4.20$	$c=7.98$	$c=4.19$	4.19 [18]
$V$	12.26	12.26	12.44	12.00 [34]	12.35	12.35	12.53	12.26 [18]
$B$	298	288	303	$301 \pm 7$ [37]	346	340	340	

$\beta$ -TM<sub>2</sub>N (space group  $I4_1/amd$ ) is a low-temperature tetragonal phase with an ordering of vacancies on the non-metal sublattice from  $\gamma$ -TM<sub>2</sub>N [35]. Tetragonal t-Mo<sub>2</sub>N is constructed from perfect cubic B1-TMN by removing 50% of the nitrogen atoms in the [100] and [010] directions in order to obtain 50% vacancies on the non-metal sublattice [36]. Three different structural configurations are tested for  $\gamma$ -TM<sub>2</sub>N and the results are listed in Table 7.1, where  $\gamma$ -TM<sub>32</sub>N<sub>16</sub> denotes the SQS configuration.

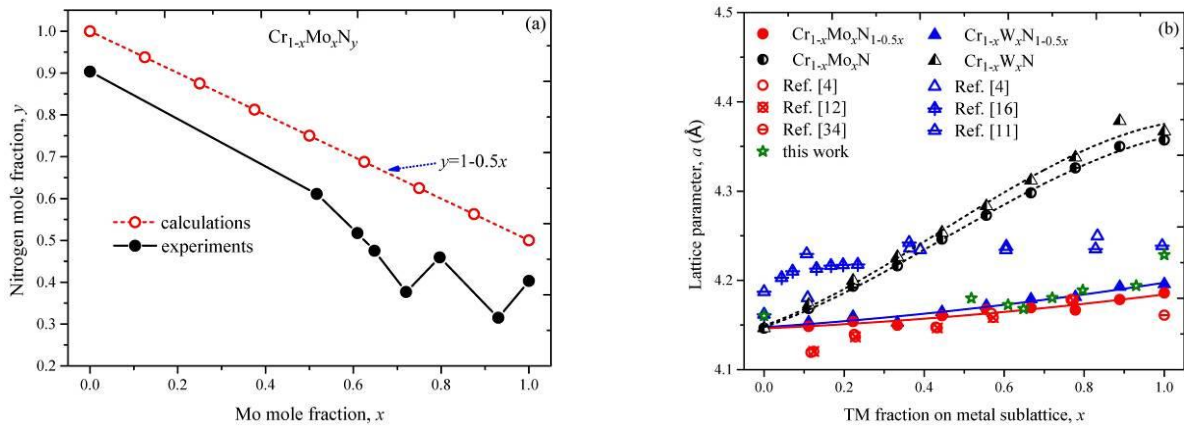


Fig. 7.2. (a) The nitrogen content of deposited Cr-Mo-N thin films (solid symbols) as a function of the Mo content. The nitrogen compositions used in the calculations (open symbols) are added for comparison. (b) The lattice parameters of  $\text{Cr}_{1-x}\text{TM}_x\text{N}$  (half-open symbols) and  $\text{Cr}_{1-x}\text{TM}_x\text{N}_{1-0.5x}$  (solid symbols) (TM = Mo and W) as function of TM fraction on metal sublattice, together with experimental values (open symbols) [4, 11, 12, 16, 34] for comparison.

It clearly shows that different structural configurations only little influence the total energies, lattice spacing, and bulk moduli, therefore they are not further considered. Especially, the experimental bulk moduli and the lattice parameters of  $\gamma$ -TM<sub>2</sub>N [18, 37] show a good

---

agreement with calculated results.

We present the nitrogen content for Cr-Mo-N coatings as a function of their Mo content, see Fig. 7.2a, and their lattice parameters, Fig. 7.2b. Figure 7.2a clearly shows that the nitrogen content within our Cr-Mo-N coatings strongly depends on their Mo content. The experimental observations (solid symbols) can nicely be described with our calculated model solid solutions (open symbols). Based on this agreement we can conclude that the nitrogen vacancies have to be taken into account for these material systems. The calculated lattice parameters of stoichiometric cubic  $\text{Cr}_{1-x}\text{TM}_x\text{N}$  (TM = Mo and W) show a significant deviation from experimental data [4, 11, 12, 16, 34] and the deviation increase with increasing Mo or W content [6], see Fig. 7.2b. On the other hand, the calculated results for cubic  $\text{Cr}_{1-x}\text{TM}_x\text{N}_{1-0.5x}$  with N vacancies yield a good agreement with the experimental results. The lattice parameters of cubic  $\text{Cr}_{1-x}\text{Mo}_x\text{N}_{1-0.5x}$  and  $\text{Cr}_{1-x}\text{W}_x\text{N}_{1-0.5x}$  are close to each other, and show a linear Vegard-like behavior [38]. This indicates that the nitrogen content in the cubic Cr-Mo-N and Cr-W-N solid solutions is linearly dependent on the fraction of  $\gamma\text{-TM}_2\text{N}$  and hence varies along the  $\text{CrN}+\gamma\text{-TM}_2\text{N}$  tie line, which has recently been confirmed by an independently experimental work [39], which is not published yet. Therefore, we propose using chemical formula  $\text{Cr}_{1-x}\text{TM}_x\text{N}_{1-0.5x}$  to describe the chemical composition of cubic Cr-Mo-N and Cr-W-N solid solutions. Here we should notice that under some extreme conditions, it is still possible to prepare  $\text{Cr}_{1-x}\text{TM}_x\text{N}$  materials, but just with a limited maximum Mo or W content, for example, using a very high (pure)  $\text{N}_2$  pressure to prepare the these coatings. While the theoretical and experimental lattice constants yield an excellent agreement for  $\text{Cr}_{1-x}\text{Mo}_x\text{N}_{1-0.5x}$ , the experimental lattice constants of  $\text{Cr}_{1-x}\text{W}_x\text{N}_{1-0.5x}$  show a small positive deviation from the theoretical results, which is more likely due to the excessive nitrogen atoms at the grain boundaries for overstoichiometric  $\text{WN}_x$  thin films [18]. As mentioned above, Cr-Mo-N and Cr-W-N solid solutions exhibit a strong tendency for N substoichiometry, and hence using  $\text{Cr}_{1-x}\text{TM}_x\text{N}_{1-0.5x}$  as the chemical formula for cubic Cr-Mo-N and Cr-W-N solid solutions is more precise than the conventionally used  $\text{Cr}_{1-x}\text{TM}_x\text{N}$  as it expresses the correct information about the chemical composition of cubic Cr-Mo-N and Cr-W-N solid solutions.

Previous theoretical calculations have illustrated that the mixing enthalpies of  $\text{Cr}_{1-x}\text{TM}_x\text{N}$  with respect to cubic B1-CrN and TMN are in contrast with experimental observations [6], and thus cannot be used to evaluate the phase stability of cubic Cr-Mo-N and Cr-W-N systems. In an earlier work, we have argued that this is because cubic B1-MoN and B1-WN are mechanically unstable, and therefore lead to the anomalous negative mixing enthalpies [6]. Therefore, we have suggested that using  $\text{CrN}+\text{TM}_2\text{N}+\text{N}_2$  as the reference state for evaluating the mixing enthalpies of  $\text{Cr}_{1-x}\text{TM}_x\text{N}$  is more meaningful [6]. Although the mixing enthalpies of  $\text{Cr}_{1-x}\text{TM}_x\text{N}$ , when using  $\text{CrN}+\text{TM}_2\text{N}+\text{N}_2$  as the reference state, predict the possibility of isostructural decomposition, the description is not really correct, as the large substoichiometry of nitrogen in Cr-Mo-N and Cr-W-N solid solutions is not taken into account.

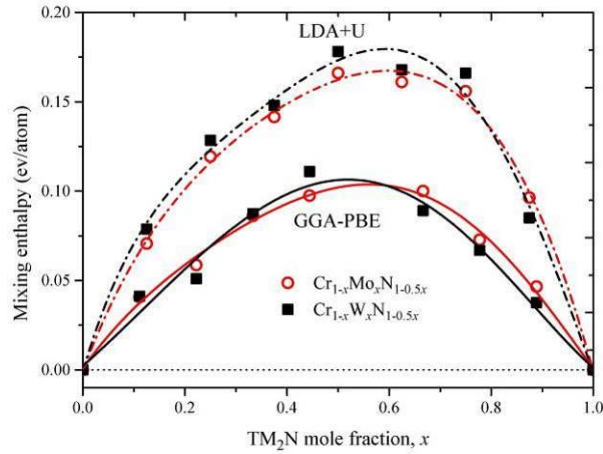


Figure 7.3: Calculated isostructural mixing enthalpies of  $\text{Cr}_{1-x}\text{Mo}_x\text{N}_{1-0.5x}$  (open circle symbols with red lines) and  $\text{Cr}_{1-x}\text{W}_x\text{N}_{1-0.5x}$  (solid square symbols with black lines) as functions of the  $\text{TM}_2\text{N}$  content. The solid lines denote the results from the GGA scheme with 64-atoms supercells, while the dotted lines denote the results derived from the LDA+U ( $U-J = 3$  eV) scheme with 128-atoms supercells.

Therefore, in addition to our previous studies also the mixing enthalpies of cubic  $\text{Cr}_{1-x}\text{Mo}_x\text{N}_{1-0.5x}$  and  $\text{Cr}_{1-x}\text{W}_x\text{N}_{1-0.5x}$  are evaluated with respect to cubic B1-CrN and  $\gamma\text{-TM}_2\text{N}$  (Fig. 7.3). Consequently, these materials correspond to the quasi-binary tie line CrN–Mo<sub>2</sub>N and CrN–W<sub>2</sub>N. Inspired by recent works [24, 40], showing that the strong electron correlation effects play a crucial role on the phase stability, the local density approximation (LDA) plus a

---

Hubbard U-term method within the framework of the Dudarev formulation [41, 42] is employed. This allows to consider the impact of strong electron correlation effects on the mixing enthalpy, together with 4x4x4 supercells containing 128 atoms ( $k$ -point meshes: 3x3x3). The black lines denote the mixing enthalpies of cubic  $\text{Cr}_{1-x}\text{TM}_x\text{N}_{1-0.5x}$  from GGA scheme using 64-atoms supercells. Their mixing enthalpies evaluated from LDA+U scheme, with the value of effective U-J = 3eV using 128-atoms supercells, are represented by dotted lines.

The cubic  $\text{Cr}_{1-x}\text{Mo}_x\text{N}_{1-0.5x}$  and  $\text{Cr}_{1-x}\text{W}_x\text{N}_{1-0.5x}$  systems exhibit a similar mixing behavior, with the same maximum mixing enthalpies of about 0.11 and 0.17 eV/atom from GGA and LDA+U schemes, respectively. The higher mixing enthalpies for cubic  $\text{Cr}_{1-x}\text{Mo}_x\text{N}_{1-0.5x}$  and  $\text{Cr}_{1-x}\text{W}_x\text{N}_{1-0.5x}$  systems from LDA+U scheme originate from the impact of considering strong electron correlations effects, which make the  $d$ -states more localized and finally weaken the hybridization between the neighboring metal-metal bonds as compared to GGA exchange-correlation approximation. The large positive mixing enthalpies of cubic  $\text{Cr}_{1-x}\text{Mo}_x\text{N}_{1-0.5x}$  and  $\text{Cr}_{1-x}\text{W}_x\text{N}_{1-0.5x}$  are mainly due to the significantly larger covalent radii of Mo (1.45 Å) and W (1.46 Å) as compared with Cr (1.27 Å) [43]. Although our data explicitly address only certain content of nitrogen vacancies (corresponding to the  $\text{Cr}_{1-x}\text{TM}_x\text{N}_{1-0.5x}$  chemical formula), they represent the lower limit of the mixing enthalpies of cubic  $\text{Cr}_{1-x}\text{Mo}_x\text{N}_{1-y}$  (with  $y < 0.5x$ ). This conclusion is also based on experimental observations showing that it is extremely difficult to incorporate more nitrogen atoms into  $\gamma$ - $\text{TM}_2\text{N}$ . Actually, for nitrogen contents above 50 at.%, the  $\gamma$ - $\text{TM}_2\text{N}$  transforms into other structures [28, 37]. The large positive mixing enthalpies for  $\text{Cr}_{1-x}\text{Mo}_x\text{N}_{1-0.5x}$  and  $\text{Cr}_{1-x}\text{W}_x\text{N}_{1-0.5x}$  are comparable to the well-investigated  $\text{Ti}_{1-x}\text{Al}_x\text{N}$  system with a maximum mixing enthalpy of about 0.11 eV/atom, which experiences a spontaneous spinodal decomposition into coherent cubic domains of AlN and Ti-enrich  $\text{Ti}_{1-x}\text{Al}_x\text{N}$  [44]. This implies that cubic Cr-Mo-N and Cr-W-N systems show great tendency towards isostructural phase decomposition and by near-equilibrium deposition techniques it will be difficult to synthesize single phase cubic  $\text{Cr}_{1-x}\text{Mo}_x\text{N}_{1-0.5x}$  and  $\text{Cr}_{1-x}\text{W}_x\text{N}_{1-0.5x}$  solid solutions. This is consistent with recent experimental observations, showing that even for the lowest concentrations (~1 at.%), spontaneous phase segregation into Mo- and W-rich regions

---

occurs [9]. We envision that the deposited Cr-TM-N thin films were misleadingly evaluated as single phase cubic solid solutions [10-12], because it is difficult to distinguish the cubic B1-CrN and  $\gamma$ -TM<sub>2</sub>N just from conventional XRD measurements due to their similarity in lattice parameters. Based on our results we can conclude, that the huge positive mixing enthalpies clearly provide a strong explanation for the large tendency for isostructural phase decomposition in Cr-Mo-N and Cr-W-N systems. The B1-CrN and  $\gamma$ -Mo<sub>2</sub>N or  $\gamma$ -W<sub>2</sub>N phases may not be mixed with each other under near-equilibrium conditions.

However, by physical vapor deposition, especially when using only moderate substrate temperatures (below 0.3 of the melting point of the prepared coating), solid solutions far from the thermodynamic equilibrium (i.e., metastable and even thermodynamically unstable) can be realized [3]. The calculated elastic constants  $C_{11}$ ,  $C_{12}$ , and  $C_{44}$ , for cubic Cr<sub>1-x</sub>Mo<sub>x</sub>N<sub>1-0.5x</sub> and Cr<sub>1-x</sub>W<sub>x</sub>N<sub>1-0.5x</sub> solid solutions (Fig. 7.4), fulfill the corresponding Huang-Born stability criteria [45]. Consequently, cubic Cr<sub>1-x</sub>Mo<sub>x</sub>N<sub>1-0.5x</sub> and Cr<sub>1-x</sub>W<sub>x</sub>N<sub>1-0.5x</sub> are mechanically stable over the entire composition range. This is a further strong argument (in addition to the excellent agreement between calculated and measured nitrogen content and the calculated mixing enthalpy), that for these material systems the content of nitrogen vacancies scales with 0.5 of the Mo or W content, hence their chemical formula is Cr<sub>1-x</sub>TM<sub>x</sub>N<sub>1-0.5x</sub>. The calculated elastic constant  $C_{12}$  increases with the content of  $\gamma$ -TM<sub>2</sub>N, while  $C_{44}$  keeps an almost constant value in the whole composition range. Consequently, the Cauchy pressure,  $C_{12}-C_{44}$ , increases with increasing Mo or W content and thereby, also the metallic bonding character and ductility of Cr<sub>1-x</sub>TM<sub>x</sub>N<sub>1-0.5x</sub>.

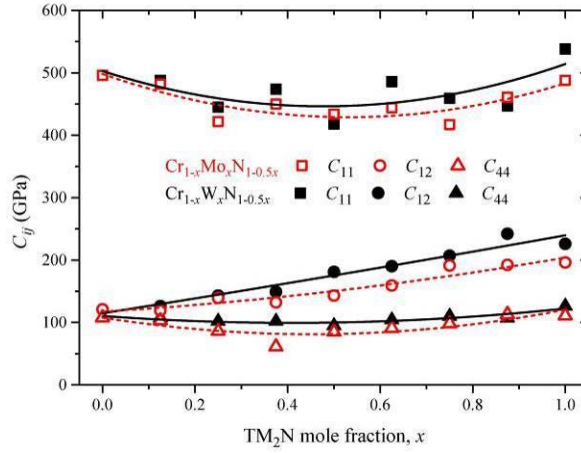


Figure 7.4: Calculated single crystal elastic constants  $C_{11}$ ,  $C_{12}$ , and  $C_{44}$  of  $\text{Cr}_{1-x}\text{Mo}_x\text{N}_{1-0.5x}$  and  $\text{Cr}_{1-x}\text{W}_x\text{N}_{1-0.5x}$ .

Deposited thin films usually have a fibrous growth texture with a preferred orientation along a certain  $\langle hkl \rangle$  direction perpendicular to the substrate surface [46]. Therefore, we calculated directionally dependent Young's moduli,  $E_{hkl}$ , for cubic  $\text{Cr}_{1-x}\text{Mo}_x\text{N}_{1-0.5x}$  and  $\text{Cr}_{1-x}\text{W}_x\text{N}_{1-0.5x}$  compositions in  $\langle 100 \rangle$ ,  $\langle 110 \rangle$ , and  $\langle 111 \rangle$  directions, Fig. 7.5.

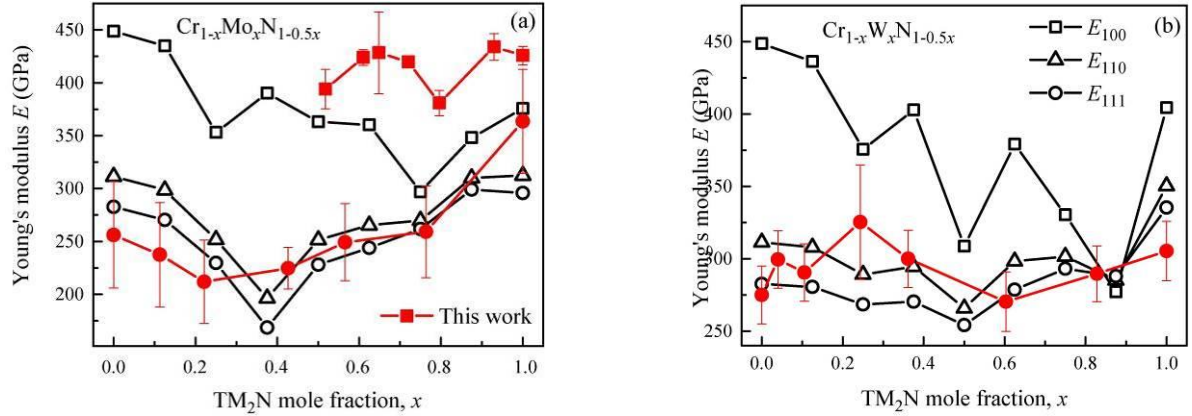


Figure 7.5: Young's moduli in the  $\langle 100 \rangle$  (square symbols),  $\langle 110 \rangle$  (triangle symbols), and  $\langle 111 \rangle$  (circle symbols) directions of  $\text{Cr}_{1-x}\text{TM}_x\text{N}_{1-0.5x}$  (TM = Mo and W) as functions of the  $\text{TM}_2\text{N}$  content. The experimental Young's moduli (solid circle symbols) [12, 13] are presented for comparison.

Both cubic solid solutions,  $\text{Cr}_{1-x}\text{Mo}_x\text{N}_{1-0.5x}$  and  $\text{Cr}_{1-x}\text{W}_x\text{N}_{1-0.5x}$ , exhibit direction dependent Young's moduli in the whole composition range, with  $\langle 100 \rangle$  direction being significantly

---

stiffer than the other directions. This behavior follows the single crystal elastic constant  $C_{ij}$ , Fig. 7.4, due to the strongest contribution of  $C_{11}$  to  $E_{100}$ . The calculated  $E_{100}$  data are in excellent agreement to the experimentally obtained Young's moduli of our coatings with a strong  $\langle 100 \rangle$  growth texture. The literature data, with a reported preferred  $\langle 111 \rangle$  orientation [12, 13], are in excellent agreement with our  $E_{111}$  calculations. Our data clearly shows that the Young's moduli can be significantly different for various directions. Consequently, this needs to be considered when comparing experimental and theoretical data.

## 7.4 Conclusions

In this chapter, the nitrogen substoichiometry in cubic Cr-Mo-N and Cr-W-N solid solutions was systemically studied by first-principles calculations and compared with experimental data of the lattice spacing, mixing thermodynamics, and elastic properties. Cubic Cr-Mo-N and Cr-W-N systems intrinsically contain a significant amount of vacancies on N sublattice. The content of vacancies increases with increasing Mo or W fraction. Based on our comprehensive investigations we propose a new chemical formula for cubic Cr-Mo-N and Cr-W-N systems,  $\text{Cr}_{1-x}\text{TM}_x\text{N}_{1-0.5x}$ , which reflects the increasing amount of vacancies on the N sublattice, and consequently is more precise than with the conventionally used  $\text{Cr}_{1-x}\text{TM}_x\text{N}_{1-0.5x}$ . The large positive mixing enthalpies of cubic  $\text{Cr}_{1-x}\text{Mo}_x\text{N}_{1-0.5x}$  and  $\text{Cr}_{1-x}\text{W}_x\text{N}_{1-0.5x}$  indicate a significant thermodynamic driving force for isostructural phase decomposition into cubic B1-CrN and  $\gamma\text{-TM}_2\text{N}$ . The elastic constants show that cubic  $\text{Cr}_{1-x}\text{Mo}_x\text{N}_{1-0.5x}$  and  $\text{Cr}_{1-x}\text{W}_x\text{N}_{1-0.5x}$  solid solutions are mechanically stable in the whole composition range and the positive Cauchy pressure,  $C_{12} - C_{44}$ , indicates the increasing ductility with increasing content of Mo or W. An excellent agreement of Young's moduli is obtained between theoretical and experimental results once the coating's texture is considered.

---

## References

- [1] G. Berg *et al.*, Surf. Coat. Technol. **86**, 184 (1996).
- [2] P. H. Mayrhofer, H. Willmann, and A. E. Reiter, Surf. Coat. Technol. **202**, 4935 (2008).
- [3] P. H. Mayrhofer *et al.*, Prog. Mater Sci. **51**, 1032 (2006).
- [4] P. Hones, R. Sanjinés, and F. L. Lévy, Thin Solid Films **332**, 240 (1998).
- [5] B. Gu *et al.*, Surf. Coat. Technol. **202**, 2189 (2008).
- [6] L. Zhou, H. David, and H. M. Paul, J. Phys. D: Appl. Phys. **46**, 365301 (2013).
- [7] A. Magnéti, Acta Crystallographica **6**, 495 (1953).
- [8] G. Gassner *et al.*, Surf. Coat. Technol. **201**, 3335 (2006).
- [9] C. X. Quintela, B. Rodríguez-González, and F. Rivadulla, Appl. Phys. Lett. **104**, 022103 (2014).
- [10] K. Ho Kim *et al.*, Surf. Coat. Technol. **201**, 4068 (2006).
- [11] P. Hones *et al.*, J. Vac. Sci. Technol., B **18**, 2851 (2000).
- [12] P. Hones *et al.*, J. Vac. Sci. Technol., A **17**, 1024 (1999).
- [13] F. L. Lévy *et al.*, Surf. Coat. Technol. **120-121**, 284 (1999).
- [14] G. L. W. Hart, and B. M. Klein, Phys. Rev. B **61**, 3151 (2000).
- [15] F.-B. Wu, S.-K. Tien, and J.-G. Duh, Surf. Coat. Technol. **200**, 1514 (2005).
- [16] B. S. Yau *et al.*, Thin Solid Films **516**, 1877 (2008).
- [17] P. Hones *et al.*, J. Phys. D: Appl. Phys. **36**, 1023 (2003).
- [18] Y. G. Shen, and Y. W. Mai, Mater. Sci. Eng., A **288**, 47 (2000).
- [19] G. Kresse, and J. Hafner, Phys. Rev. B **47**, 558 (1993).
- [20] G. Kresse, and J. Furthmüller, Phys. Rev. B **54**, 11169 (1996).
- [21] G. Kresse, and D. Joubert, Phys. Rev. B **59**, 1758 (1999).
- [22] J. P. Perdew, K. Burke, and M. Ernzerhof, Phys. Rev. Lett. **77**, 3865 (1996).
- [23] S. H. Wei *et al.*, Phys. Rev. B **42**, 9622 (1990).
- [24] L. Zhou, F. Körmann, D. Holec, M. Bartosik, B. Grabowski, J. Neugebauer, and P. H. Mayrhofer, Phys. Rev. B **90**, 184102 (2014).
- [25] L. Zhou, D. Holec, and P. H. Mayrhofer, J. Appl. Phys. **113**, 043511 (2013).

- 
- [26] M.T. Baben, L. Raumann, D. Music, J.M. Schneider, *J. Phys.: Condens. Matter* **24**, 155401 (2012).
- [27] B. Alling, A. Karimi, L. Hultman, I.A. Abrikosova, *Appl. Phys. Lett.* **92**, 071903 (2008).
- [28] D. Machon *et al.*, *physica status solidi (a)* **203**, 831 (2006).
- [29] H. J. Monkhorst, and J. D. Pack, *Phys. Rev. B* **13**, 5188 (1976).
- [30] H. Jehn, and P. Ettmayer, *Journal of the Less Common Metals* **58**, 85 (1978).
- [31] J. A. Thornton, *J Vac Sci Technol* **12**, 830 (1975).
- [32] W. C. Oliver, and G. M. Pharr, *J. Mater. Res.* **7**, 1564 (1992).
- [33] A. C. Fischer-Cripps, *Surf. Coat. Technol.* **200**, 4153 (2006).
- [34] C. L. Bull *et al.*, *J. Solid State Chem.* **179**, 1762 (2006).
- [35] P. Ettmayer, *Monatsh. Chem.* **101**, 127 (1970).
- [36] I. Matanović, F. H. Garzon, and N. J. Henson, *PCCP* **16**, 3014 (2014).
- [37] E. Soignard *et al.*, *Phys. Rev. B* **68**, 132101 (2003).
- [38] L. Vegard, *Z. Phys. Chem.* **5**, 17 (1921).
- [39] Fedor *et al.*, in preparation (2014).
- [40] B. Alling *et al.*, *Appl. Phys. Lett.* **102**, 031910 (2013).
- [41] V. I. Anisimov, J. Zaanen, and O. K. Andersen, *Phys. Rev. B* **44**, 943 (1991).
- [42] S. L. Dudarev *et al.*, *Phys. Rev. B* **57**, 1505 (1998).
- [43] A. M. James, and M. P. Lord, *Macmillan's Chemical and Physical Data* (Macmillan, London, UK, 1992).
- [44] D. Holec *et al.*, *Surf. Coat. Technol.* **206**, 1698 (2011).
- [45] M. Born, K. Huang, and G. Britain, *Dynamical theory of crystal lattices* (Clarendon Press Oxford, 1954).
- [46] K. J. Martinschitz *et al.*, *J. Appl. Crystallogr.* **42**, 416 (2009).

---

# Chapter 8

## Structure, mechanical and electric properties of quaternary Cr-Al-TM-N

---

### 8.1 Motivation

In the previous chapter 6, the alloying effects of transition metal (TM) elements on the CrN have been discussed. This chapter, further extends the calculational alloy design by studying alloying effects of III B, IV B, and V B transition metal (TM) elements on  $\text{Cr}_{1-x}\text{Al}_x\text{N}$ . The impact of such a fourth element on the phase stability, structural and mechanical properties is systematically discussed using *ab initio* calculations.

### 8.2 Computational methods

The chemical disorder between Cr, Al, and TM atoms on the metal sublattice of the cubic B1 structure (NaCl prototype, space group  $Fm\bar{3}m$ ), and also the paramagnetic state induced by Cr atoms are obtained by the special quasi-random structures (SQS) approach [1,2] as implemented in our previous studies. Mixing of  $\text{Cr}^\uparrow$ ,  $\text{Cr}^\downarrow$ , Al, and TM atoms takes place on the metal-sublattice while the nitrogen-sublattice is fully occupied with N atoms.  $4 \times 3 \times 2$  (48 atoms) and  $3 \times 2 \times 2$  (48 atoms) supercells are used for the cubic B1 and wurtzite B4  $\text{Cr}_{1-x-y}\text{Al}_x\text{TM}_y\text{N}$  structures, respectively. The short range order parameters (SROs) are optimized for pair correlations of fifth order at least.

The Density Functional Theory based calculations are performed using the Vienna Ab initio Simulation Package (VASP) [3,4]. The ion-electron interactions are described by the projector augmented wave method (PAW) [5] with an energy cutoff of 500 eV, and the generalized gradient approximation (GGA) for the exchange-correction effects as parameterized by

---

Perdew–Burke–Ernzerhof (PBE) [6]. The  $k$ -point meshes are  $5 \times 6 \times 7$  and  $5 \times 8 \times 4$  for the cubic B1 and the wurtzite B4 structures, respectively. The energy convergence criterion for the electronic self-consistency was set to 0.1 meV/atom.

## 8.3 Results and discussions

### 8.3.1 Impact of the quaternary additions on maximum Al solubility in the cubic phase

The stability of the quaternary systems is determined from their energy of formation,  $E_f$ , calculated as

$$E_f = E(\text{Cr}_{1-x-y}\text{Al}_x\text{TM}_y\text{N}) - 0.5[(1-x-y)E(\text{Cr}^{\text{bcc}}) + xE(\text{Al}^{\text{fcc}}) + yE(\text{TM}^\xi) + 0.5E(\text{N}_2)] \quad (8.1)$$

where  $E(\text{Cr}_{1-x-y}\text{Al}_x\text{TM}_y\text{N})$  is the total energy per atom of  $\text{Cr}_{1-x-y}\text{Al}_x\text{TM}_y\text{N}$ ,  $E(\text{Cr}^{\text{bcc}})$ ,  $E(\text{Al}^{\text{fcc}})$ , and  $E(\text{TM}^\xi)$  are the total energies of the respective elements in their stable configurations.

$E(\text{N}_2)$  denotes the total energy of a nitrogen molecule. Figure 8.1 presents the maximum AlN content  $x$  in the cubic  $\text{Cr}_{1-x-y}\text{Al}_x\text{TM}_y\text{N}$  phase as a function of the TM content  $y$  based on the energy of formation differences between B1 and B4 structures, evaluated according to Eq. 8.1. Clearly, all elements cause a decrease of the maximum Al solubility in the cubic  $\text{Cr}_{1-x-y}\text{Al}_x\text{TM}_y\text{N}$  phase. We ascribe this to larger lattice distortions resulting from the typically larger atomic radius of the III B, IV B, and V B TMs than that of Cr and Al.

For our studies, the alloying effect of TM elements on the cubic  $\text{Cr}_{1-x}\text{Al}_x\text{N}$  phase, the presentation of the quaternary  $\text{Cr}_{1-x-y}\text{Al}_x\text{TM}_y\text{N}$  phases within a pseudo-binary system of  $\text{Cr}_{1-x}\text{Al}_x\text{N}$  and TMN is more illustrative. The influence of Ti and V on the maximum solubility of Al is significantly smaller than that of the other elements. Our results suggest that the lattice parameters exhibit a major role in promoting either the B1 or B4 structure (the B4 structure, wurtzite-type, has a significantly larger specific volume), although the binding characteristics

are important as well. The nitrides VN and TiN exhibit the smallest lattice parameters among the alloying TMN's studied here, with  $a = 4.127$  and  $4.253$  Å, respectively. These are very similar to that of  $\text{Cr}_{1-x}\text{Al}_x\text{N}$  with  $a$  between  $\sim 4.11$  and  $4.16$  Å for Al-contents  $x$  between 0.7 and 0, respectively. The TMN's of III B (ScN), IV B (ZrN, HfN), and V B (TaN, NbN) have very comparable effects on the phase stability ranges, due to their very similar lattice parameters of 4.4–4.6 Å. The addition of YN to  $\text{Cr}_{1-x}\text{Al}_x\text{N}$  causes a pronounced reduction of the maximum Al solubility, because YN exhibits also the largest lattice parameter of 4.921 Å.

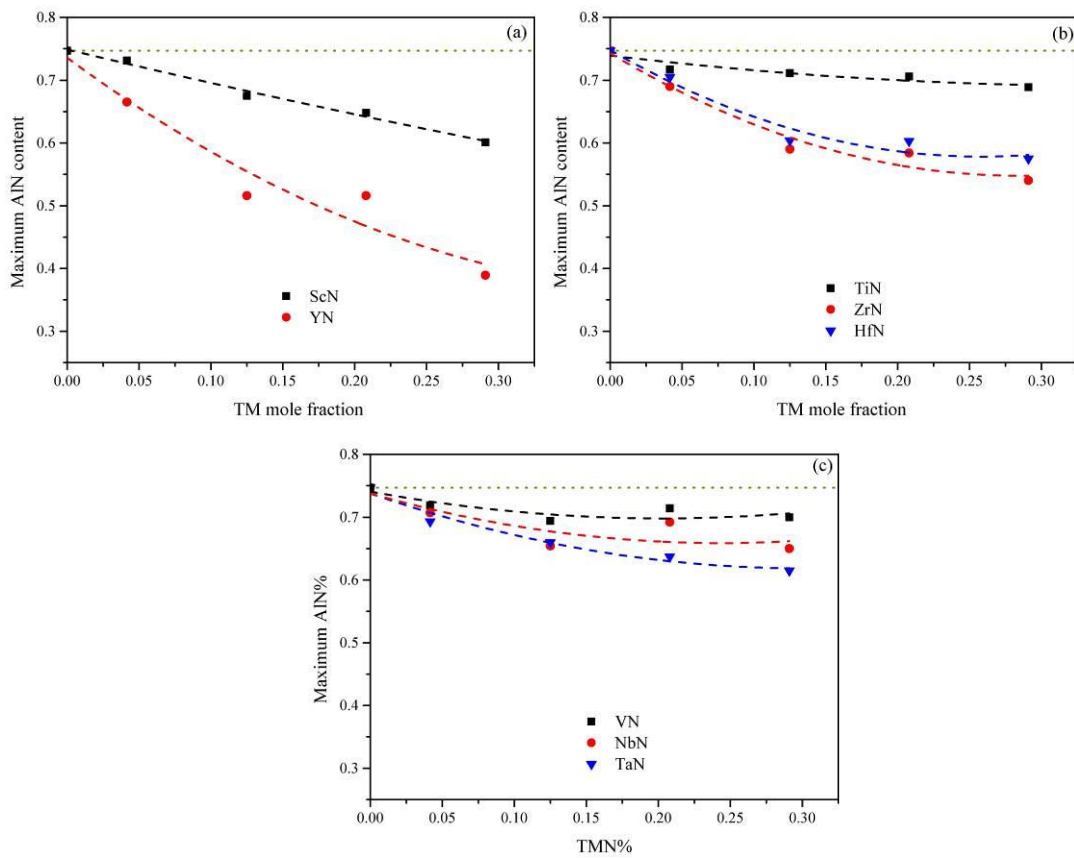


Figure 8.1: The maximum AlN content in the cubic  $\text{Cr}_{1-x-y}\text{Al}_x\text{TM}_y\text{N}$  phases as a function of the TMN addition. The horizontal dotted lines denote the maximum AlN content in the cubic  $\text{Cr}_{1-x}\text{Al}_x\text{N}$  phase.

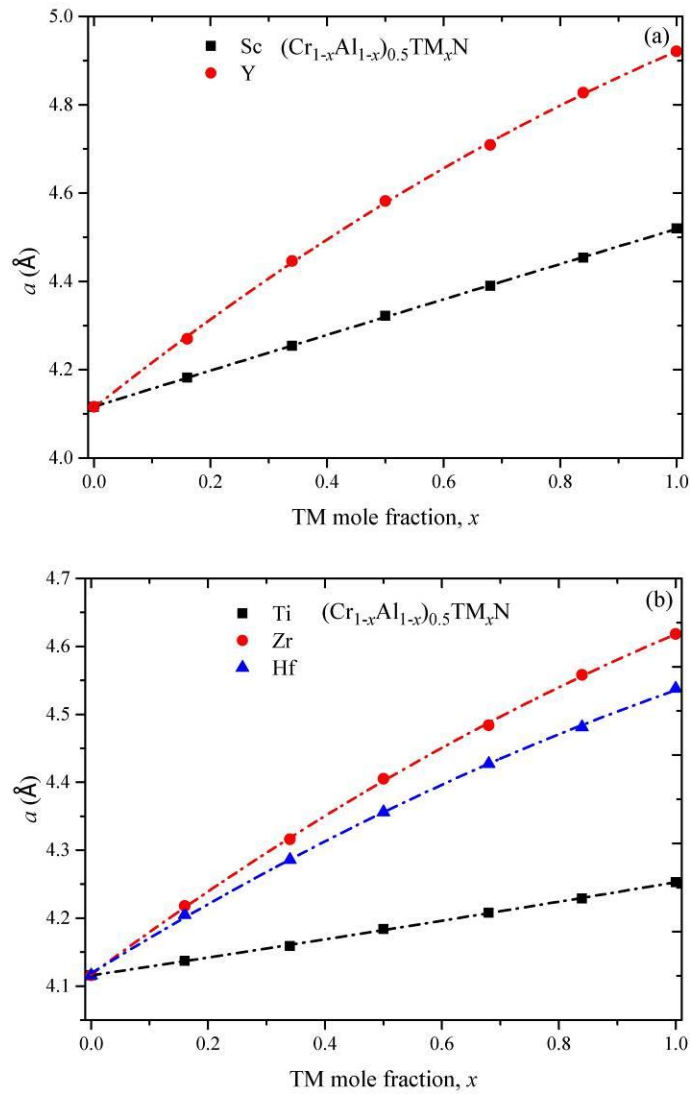
### 8.3.2 Structural properties

As mentioned in the section above, the quaternary  $\text{Cr}_{1-x-y}\text{Al}_x\text{TM}_y\text{N}$  alloys can be treated as pseudo-binary systems between  $\text{Cr}_{1-x}\text{Al}_x\text{N}$  and TMN, which provides a straightforward

approach to quantify the alloying effect of TMs on the structural and mechanical properties of  $\text{Cr}_{1-x}\text{Al}_x\text{N}$ . The following calculations were performed for the  $(\text{Cr}_{0.5}\text{Al}_{0.5})_{1-y}\text{TM}_y\text{N}$  systems with a compositional step of  $y=0.167$ . The calculated values were fitted with a quadratic polynomial after

$$a(y) = ya_{\text{TMN}} + (1-y)a_{\text{Cr}_{0.5}\text{Al}_{0.5}\text{N}} + by(1-y) \quad (8.2)$$

where  $b$  is a bowing parameter describing the deviation from the linear Vegard's-like behaviour,  $a_{\text{TMN}}$  and  $a_{\text{Cr}_{0.5}\text{Al}_{0.5}\text{N}}$  are the lattice constants of TMN and  $\text{Cr}_{0.5}\text{Al}_{0.5}\text{N}$ , respectively, and  $a(y)$  is the lattice constant of  $(\text{Cr}_{0.5}\text{Al}_{0.5})_{1-y}\text{TM}_y\text{N}$ .



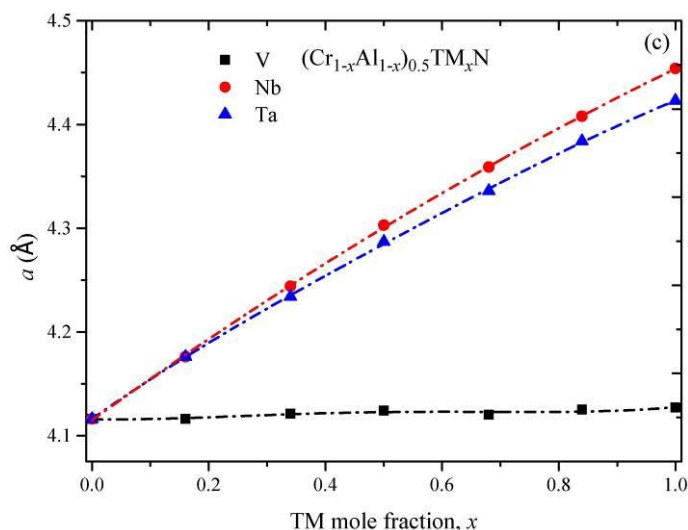


Figure 8.2: Calculated equilibrium lattice parameters for  $(\text{Cr}_{0.5}\text{Al}_{0.5})_{1-y}\text{TM}_y\text{N}$  (TM=Sc, Y, Ti, Zr, Hf, V, Nb, and Ta) solid solutions as a function of the TMN content,  $y$ . The Figure is divided into  $a$ ,  $b$ , and  $c$  panels, according to the TM groups, IIIB, IVB, and VB, respectively.

Figure 8.2 presents the lattice parameters of  $(\text{Cr}_{0.5}\text{Al}_{0.5})_{1-y}\text{TM}_y\text{N}$  (TM=Sc, Y, Ti, Zr, Hf, V, Nb, and Ta) phase as a function of TMN content, and the corresponding bowing parameters are listed in Table 8.1. The bowing parameters of  $(\text{Cr}_{0.5}\text{Al}_{0.5})_{1-y}\text{TM}_y\text{N}$  with TM = Sc, Ti, and V, are significantly smaller than those for the other systems. Consequently, these systems provide the most linear behaviour out of these systems, in agreement with the results obtained for Sc, Ti and V alloyed Cr-N reported in the previous chapter 6 and in Ref [7]. We speculate that this is related with the fact that the covalent  $sp^3d^2$  hybridization is formed from the same  $d$  orbitals supplied by  $3d$  group TM elements. VN has almost the same lattice constant as  $\text{Cr}_{0.5}\text{Al}_{0.5}\text{N}$  and hence there is only a minimum variation of the lattice constant of  $(\text{Cr}_{0.5}\text{Al}_{0.5})_{1-y}\text{V}_y\text{N}$  with VN mole fraction,  $y$ . Cubic lattice parameters of  $(\text{Cr}_{0.5}\text{Al}_{0.5})_{1-y}\text{TM}_y\text{N}$  (with TM = Y, Zr, Hf, Nb, and Ta) systems exhibit distinct bowing towards larger values, hence, a distinct positive deviation from the Vegard's estimations. This behaviour suggests that compressing larger compounds is energetically more expensive than expanding smaller ones, which is in agreement with the slightly asymmetric bonding energy potential curve.

The lattice parameters, as given in Table 8.1 and Figure 8.2, provide useful information for designing coatings, and especially for the interpretation of experimental observations. For

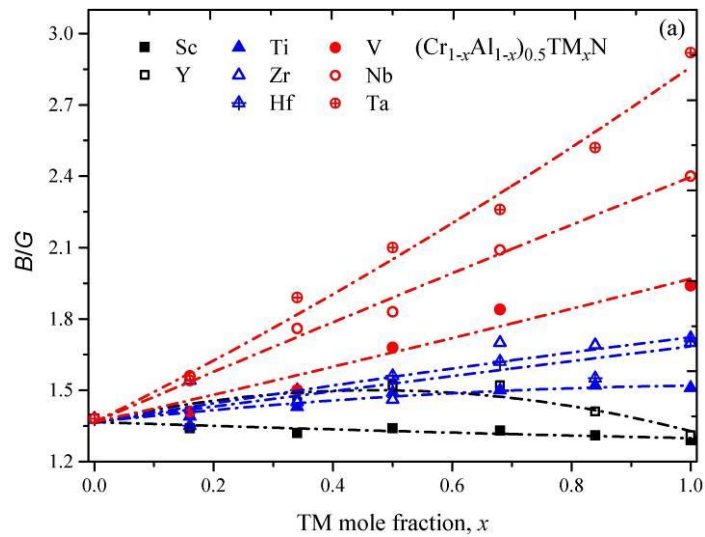
example, the nearly constant behaviour of the lattice constant of  $(\text{Cr}_{0.5}\text{Al}_{0.5})_{1-y}\text{V}_y\text{N}$  with VN mole fraction could be potentially interesting for epitaxial, coherency stress-free multilayers of  $(\text{Cr}_{0.5}\text{Al}_{0.5})_{1-y}\text{V}_y\text{N}$  and VN.

Table 8.1. The bowing parameters,  $b$ , for each cubic  $(\text{Cr}_{0.5}\text{Al}_{0.5})_{1-y}\text{TM}_y\text{N}$  (with TM = Sc, Y, Ti, Zr, Hf, V, Nb, and Ta) phase.

	ScN	YN	TiN	ZrN	HfN	VN	NbN	TaN
$b$ (Å)	0.007	0.241	-0.007	0.137	0.115	0.002	0.065	0.62

### 8.3.3 Mechanical properties

The alloying effect of TMN's on the mechanical properties is discussed in terms of impact on ductility or brittleness. The single-crystal elastic constants,  $C_{ij}$ , were calculated employing the stress-strain method as described in Refs. [8,9]. Subsequently, the isotropic equivalents of polycrystalline properties are computed via the self-consistent Hershey approach [10] from single-crystal elastic constants.



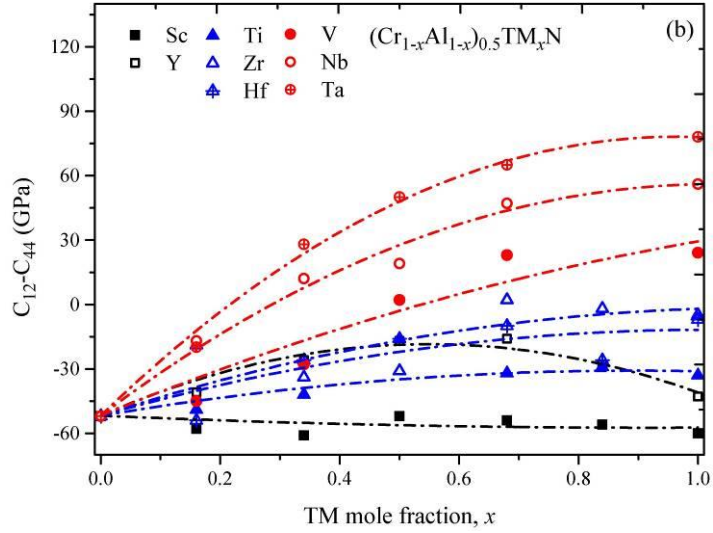


Figure 8.3: The  $B/G$  (a) and the Cauchy pressure,  $C_{12}-C_{44}$ , (b) of cubic  $(Cr_{0.5}Al_{0.5})_{1-y}TM_yN$  (with  $TM = Sc, Y, Ti, Zr, Hf, V, Nb,$  and  $Ta$ ) solid solutions as a function of the TMN content,  $y$ .

According to the criteria proposed by Pettifor and Pugh [11,12], positive Cauchy pressure ( $C_{12}-C_{44} > 0$ ) values, and bulk-to-shear moduli ratios ( $B/G$ ) above 1.75 indicate ductile behaviour of materials. Consequently, our results suggest that alloying IVB and VB group elements (Ti, Zr, Hf, V, Nb, and Ta) significantly increase the  $B/G$  ratio and the Cauchy pressure of  $Cr_{0.5}Al_{0.5}N$ , see Fig. 7.3. But only for the addition of V B nitrides, VN, NbN, and TaN,  $B/G$  ratios above 1.75 and positive Cauchy pressures ( $C_{12}-C_{44} > 0$ ) are obtained. Especially TaN exhibits an extremely positive effect on the ductility of  $Cr_{0.5}Al_{0.5}N$ , as already for additions of  $y \sim 0.2$ , the Pettifor and Pugh criteria are obtained. This can be attributed to the changes of the bonding characteristic: IVB elements decrease the directional character slightly while VB elements even revert the dominant character to metallic bonding. Alloying  $Cr_{1-x}Al_xN$  with group IIIB elements (Sc and Y) causes no improvement in ductility, as the  $B/G$  ratio as well as the Cauchy pressure is almost unchanged over the whole composition range.

The alloying impact on the brittle/ductile trends of our  $Cr_{1-x}Al_xN$  is closely related with their changes in the electronic structure. Sangiovanni *et al.* pointed out that there is a relationship between the Cauchy pressure and the valence electron concentration (VEC) [13-15], suggesting that improved ductility can benefit from higher VEC. However, it is not always the case that higher VEC shows higher ductility. Cubic  $(Cr_{0.5}Al_{0.5})_{1-y}TM_yN$  with TMs from the same group

---

has all the same VEC, while their ductile behaviour differs. The most prominent example is  $(\text{Cr}_{0.5}\text{Al}_{0.5})_{1-y}\text{Ta}_y\text{N}$  with significantly higher B/G and Cauchy pressures (hence, higher suggested inherent ductility) than  $(\text{Cr}_{0.5}\text{Al}_{0.5})_{1-y}\text{V}_y\text{N}$ , although both elements belong to VB. This is because the essence of inherent ductility is related with bonding character rather than with VEC. Consequently, the key point for ductility is to analyze the bonding character, as conducted here for  $(\text{Cr}_{0.5}\text{Al}_{0.5})_{1-y}\text{TM}_y\text{N}$ .

Figure 8.4 presents the total density of states (DOS) of cubic  $\text{Cr}_{0.42}\text{Al}_{0.42}\text{TM}_{0.16}\text{N}$  (with TM = Sc, Y, Ti, Zr, Hf, V, Nb, and Ta) along with the comparison to the  $\text{Cr}_{0.5}\text{Al}_{0.5}\text{N}$  reference material. Alloying Sc and Y to cubic  $\text{Cr}_{0.5}\text{Al}_{0.5}\text{N}$  has a much smaller effect on their electronic structure than alloying other TMs. By the addition of Sc and Y, the band gap is almost unchanged and open. This may be understood by the fact that both nitrides, ScN and YN, are semiconductors on their own. Furthermore, also the directional bonding character of  $\text{Cr}_{0.5}\text{Al}_{0.5}\text{N}$  is unchanged, and hence there is no improvement of the ductile behaviour. The addition of IVB elements increases the metallic behaviour by occupying some conduction band states. Thereby, metal-metal *d-d* bonding is enhanced and the ductility of cubic  $\text{Cr}_{0.5}\text{Al}_{0.5}\text{N}$  increases. However, there is a large pseudo-gap very close to the Fermi level for Ti, Zr, and Hf alloyed cubic  $\text{Cr}_{0.42}\text{Al}_{0.42}\text{TM}_{0.16}\text{N}$  (TM = Ti, Zr, and Hf), which represents the semiconducting character and limits the improvement of the ductility. However, alloying cubic  $\text{Cr}_{0.5}\text{Al}_{0.5}\text{N}$  with group VB elements even closes this pseudo-gap. Hence, a fully metallic behaviour is obtained leading to the enhanced ductility. Furthermore, the addition of Nb and Ta induces a peak splitting at the Fermi level together with a development of a second peak just above the Fermi level, which stems mainly from their TM *d*-states. This is similar to the behaviour reported for the  $\text{Ti}_{1-x-y}\text{Al}_x\text{TM}_y\text{N}$  (TM = Nb and Ta) quaternary system [16-18]. The peak splitting indicates a significant enhancement in metal-metal *d-d* bonding. Therefore, the alloying of  $\text{Cr}_{0.5}\text{Al}_{0.5}\text{N}$  with Nb and Ta is superior with respect to ductility improvement than the alloying with the same VB group element V.

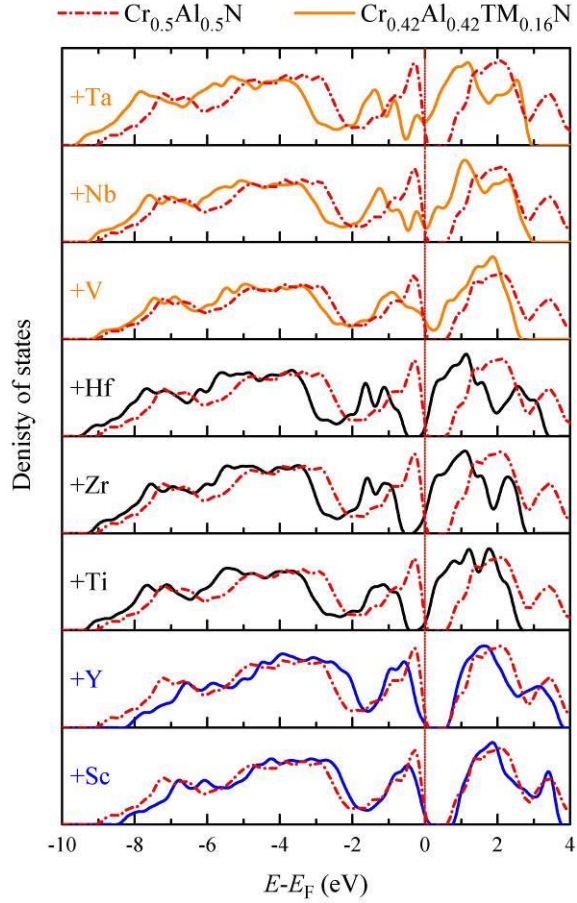


Figure 8.4: The total density of states (DOS) of cubic  $Cr_{0.42}Al_{0.42}TM_{0.16}N$  (with  $TM = Sc, Y, Ti, Zr, Hf, V, Nb,$  and  $Ta$ ) phase (solid lines). The red dash dotted lines denote the total DOS for  $Cr_{0.5}Al_{0.5}N$  as a reference.

## 8.4 Conclusions

The alloying effect of transition metal elements from the groups IIIB, IVB, and VB on the phase stability, structural, and mechanical properties of cubic  $Cr_{1-x}Al_xN$  is investigated in detail by *ab initio* calculations. Our results clearly show that the maximum solubility of Al within cubic structured  $Cr_{1-x}Al_xTM_yN$  (with  $TM = Sc, Y, Ti, Zr, Hf, V, Nb,$  and  $Ta$ ) mainly depends on the lattice parameter of the corresponding cubic structured TMN. The addition of Y significantly decreases the maximum solubility of Al within cubic structured  $Cr_{1-x}Al_xN$ , while the addition of V and Ti has the smallest effect among the TMs studied. The lattice parameters of the quaternary  $Cr_{1-x}Al_xTM_yN$  system increase both from  $3d$  to  $5d$  as well as from IIIB to VB. This

---

behaviour suggests for a combined effect of valence electrons and atom size on the lattice parameters of  $\text{Cr}_{1-x-y}\text{Al}_x\text{TM}_y\text{N}$ . More pronounced is the obtained effect on the ductility, which significantly increases by the addition of Ta or Nb, as thereby the bonding character of cubic  $\text{Cr}_{1-x}\text{Al}_x\text{N}$  massively changes towards metallic. Based on our results we can conclude that even for the same valence electron concentrations a different ductile behaviour is obtained, as the individual elements have a different effect on the binding characteristics, which determine ductility.

---

## References

- [1] S. H. Wei, L. G. Ferreira, J. E. Bernard, and A. Zunger, *Phys. Rev. B* **42**, 9622 (1990).
- [2] A. Zunger, S. H. Wei, L. G. Ferreira, and J. E. Bernard, *Phys. Rev. Lett.* **65**, 353 (1990).
- [3] G. Kresse and J. Furthmüller, *Phys. Rev. B* **54**, 11169 (1996).
- [4] G. Kresse and J. Hafner, *Phys. Rev. B* **47**, 558 (1993).
- [5] G. Kresse and D. Joubert, *Phys. Rev. B* **59**, 1758 (1999).
- [6] J. P. Perdew, K. Burke, and M. Ernzerhof, *Phys. Rev. Lett.* **77**, 3865 (1996).
- [7] L. Zhou, D. Holec, and P. H. Mayrhofer, *J. Phys. D: Appl. Phys.* **46**, 365301 (2013).
- [8] L. Zhou, D. Holec, and P. H. Mayrhofer, *J. Appl. Phys.* **113**, 043511 (2013).
- [9] D. Holec, F. Tasnádi, P. Wagner, M. Friák, J. Neugebauer, P. H. Mayrhofer, and J. Keckes, *Phys. Rev. B* **90**, 184106 (2014).
- [10] A. V. Hershey, *J. Appl. Mech.* **21**, 236 (1954).
- [11] D. G. Pettifor, *Materials Science and Technology* **8**, 345 (1992).
- [12] S. F. Pugh, *Philos. Mag.* **45**, 823 (1954).
- [13] D. G. Sangiovanni, V. Chirita, and L. Hultman, *Phys. Rev. B* **81**, 104107 (2010).
- [14] D. G. Sangiovanni, V. Chirita, and L. Hultman, *Thin Solid Films* **520**, 4080 (2012).
- [15] D. G. Sangiovanni, L. Hultman, and V. Chirita, *Acta Mater.* **59**, 2121 (2011).
- [16] D. Holec, L. Zhou, R. Rachbauer, and P. H. Mayrhofer, *J. Appl. Phys.* **113**, 113510 (2013).
- [17] R. Rachbauer, D. Holec, M. Lattmann, L. Hultman, and P. H. Mayrhofer, *Int. J. Mater. Res* **102**, 735 (2011).
- [18] R. Rachbauer, D. Holec, and P. H. Mayrhofer, *Surf. Coat. Technol.* **211**, 98 (2012).

# APPENDIX A

## Supercell Structures and short range order parameters

Table A.1: Arrangement of  $3 \times 3 \times 2$  supercells used for the calculation of the cubic B1 phases. The fractional coordinates are expressed in a cell with lattice vectors  $a_1=a(1.5, 1.5, 0)$ ,  $a_2=a(0, 1.5, 1.5)$ ,  $a_3=a(1, 0, 1)$ . Only atoms on the metallic sublattice are listed. The positions given here correspond to the starting configurations before any relaxation takes place.

Fractional coordinate			Al content on the metallic sublattice								
$x$	$y$	$z$	0.000	0.111	0.222	0.333	0.444	0.556	0.667	0.778	0.889
0.667	0.000	0.000	Cr↑	Cr↓	Cr↓	Cr↑	Cr↓	Cr↓	Al	Al	Cr↑
0.000	0.333	0.500	Cr↑	Cr↑	Cr↑	Cr↓	Al	Al	Cr↑	Al	Cr↓
0.000	0.000	0.000	Cr↓	Cr↑	Cr↑	Cr↓	Cr↑	Al	Cr↓	Al	Al
0.000	0.000	0.500	Cr↓	Cr↓	Cr↓	Cr↑	Al	Al	Al	Cr↑	Al
0.000	0.333	0.000	Cr↑	Cr↑	Cr↓	Cr↓	Cr↓	Cr↑	Al	Al	Al
0.000	0.667	0.000	Cr↑	Cr↓	Al	Al	Al	Al	Al	Cr↑	Al
0.000	0.667	0.500	Cr↑	Cr↑	Cr↓	Cr↓	Cr↓	Al	Al	Al	Al
0.333	0.000	0.000	Cr↑	Cr↓	Cr↑	Al	Cr↑	Al	Cr↑	Cr↓	Al
0.333	0.000	0.500	Cr↓	Al	Cr↑	Al	Cr↓	Cr↑	Al	Al	Al
0.333	0.333	0.000	Cr↓	Cr↑	Cr↑	Al	Al	Cr↓	Al	Al	Al
0.333	0.333	0.500	Cr↓	Cr↓	Cr↓	Cr↑	Al	Al	Al	Al	Al
0.333	0.667	0.000	Cr↓	Al	Cr↓	Cr↑	Al	Al	Cr↓	Al	Al
0.333	0.667	0.500	Cr↓	Cr↓	Al	Cr↑	Cr↑	Cr↓	Cr↑	Al	Al

---

0.667	0.000	0.500	Cr↑	Cr↑	Cr↑	Cr↓	Cr↓	Cr↓	Cr↓	Al	Al
0.667	0.333	0.000	Cr↓	Cr↓	Al	Cr↑	Al	Al	Al	Al	Al
0.667	0.333	0.500	Cr↑	Cr↓	Al	Al	Cr↑	Cr↑	Al	Al	Al
0.667	0.667	0.000	Cr↑	Cr↑	Cr↓	Cr↓	Cr↑	Cr↑	Al	Al	Al
0.667	0.667	0.500	Cr↓	Cr↑	Cr↑	Al	Al	Al	Al	Cr↓	Al

---

Table A.2: Arrangement of  $2 \times 2 \times 2$  supercells used for the calculation of the wurtzite B4 phases. The fractional coordinates are expressed in a cell with lattice vectors  $a_1 = a(1, 0, 0)$ ,  $a_2 = a(-0.5, 0.866, 0)$ ,  $a_3 = a(0, 0, c/a)$ . Only atoms on the metallic sublattice are listed. The positions given here correspond to the starting configurations before any relaxation takes place.

Fractional coordinate			Al content on the metallic sublattice							
$x$	$y$	$z$	0.000	0.125	0.250	0.375	0.500	0.625	0.750	0.875
0.167	0.333	0.500	Cr $\uparrow$	Cr $\downarrow$	Cr $\downarrow$	Al	Al	Cr $\downarrow$	Al	Cr $\uparrow$
0.667	0.333	0.500	Cr $\uparrow$	Cr $\uparrow$	Cr $\downarrow$	Cr $\downarrow$	Al	Cr $\uparrow$	Al	Cr $\downarrow$
0.167	0.333	0.000	Cr $\downarrow$	Cr $\downarrow$	Cr $\uparrow$	Cr $\uparrow$	Al	Al	Al	Al
0.333	0.167	0.250	Cr $\uparrow$	Cr $\downarrow$	Cr $\uparrow$	Cr $\downarrow$	Cr $\uparrow$	Al	Al	Al
0.333	0.167	0.750	Cr $\downarrow$	Cr $\downarrow$	Cr $\downarrow$	Al	Al	Al	Al	Al
0.167	0.833	0.000	Cr $\downarrow$	Cr $\uparrow$	Cr $\uparrow$	Cr $\uparrow$	Cr $\downarrow$	Al	Cr $\downarrow$	Al
0.333	0.667	0.250	Cr $\uparrow$	Cr $\uparrow$	Cr $\downarrow$	Al	Al	Cr $\downarrow$	Al	Al
0.167	0.833	0.500	Cr $\uparrow$	Cr $\uparrow$	Cr $\downarrow$	Al	Cr $\downarrow$	Cr $\uparrow$	Al	Al
0.333	0.667	0.750	Cr $\downarrow$	Cr $\downarrow$	Cr $\downarrow$	Al	Al	Cr $\downarrow$	Al	Al
0.667	0.333	0.000	Cr $\uparrow$	Cr $\downarrow$	Al	Cr $\downarrow$	Cr $\uparrow$	Al	Al	Al
0.833	0.167	0.250	Cr $\downarrow$	Cr $\uparrow$	Al	Cr $\downarrow$	Cr $\downarrow$	Al	Al	Al
0.833	0.167	0.750	Cr $\downarrow$	Al	Al	Cr $\uparrow$	Al	Al	Cr $\uparrow$	Al
0.667	0.833	0.000	Cr $\downarrow$	Cr $\uparrow$	Cr $\uparrow$	Cr $\downarrow$	Cr $\uparrow$	Al	Al	Al
0.833	0.667	0.250	Cr $\uparrow$	Cr $\uparrow$	Cr $\uparrow$	Cr $\uparrow$	Cr $\uparrow$	Al	Cr $\downarrow$	Al
0.667	0.833	0.500	Cr $\downarrow$	Al	Cr $\uparrow$	Al	Al	Al	Al	Al
0.833	0.667	0.750	Cr $\uparrow$	Cr $\downarrow$	Al	Cr $\uparrow$	Cr $\downarrow$	Cr $\uparrow$	Cr $\uparrow$	Al

Table A.3: Short-range order (SRO) parameters for the supercells used to model the different fractions of AlN in this work (Table A.1.). The shells correspond to nearest distances between atoms on the metallic sublattice. Cr-Al denotes averaged short range order parameters between Cr $\downarrow$ -Al and Cr $\uparrow$ -Al and Cr $\downarrow$ -Cr $\uparrow$  denotes short range order parameters of Cr $\downarrow$ -Cr $\uparrow$ .

Cubic B1										
	Shell 1		Shell 2		Shell 3		Shell 4		Shell 5	
AlN%	Cr-Al	Cr $\downarrow$ -Cr $\uparrow$								
0.889	-0.13	1.00	0.06	-2.00	-0.03	-0.50	0.06	1.00	-0.03	-0.50
0.778	-0.12	0.25	-0.07	1.00	0.09	-1.25	-0.07	1.00	-0.07	0.25
0.667	-0.13	0.00	0.00	0.00	0.04	-0.33	-0.04	0.33	-0.04	0.17
0.556	-0.09	-0.13	-0.13	0.63	0.04	-0.36	-0.01	-0.03	-0.09	0.44
0.444	-0.09	-0.14	-0.13	0.40	0.04	-0.23	-0.01	0.04	-0.09	0.28
0.333	-0.13	0.00	0.00	0.00	0.00	-0.13	0.00	0.00	0.00	0.00
0.222	-0.07	-0.13	0.04	-0.04	-0.07	0.04	-0.02	0.02	0.04	-0.04
0.111	-0.03	-0.13	-0.13	0.06	-0.03	-0.02	0.06	-0.05	-0.13	0.06
0.000		-0.04		-0.04		-0.09		0.04		0.00

Table A.4: Short-range order (SRO) parameters for the supercells used to model the different fractions of AlN in this work (Table A.2). The shells correspond to nearest distances between atoms on the metallic sublattice. Cr-Al denotes averaged short range order parameters between Cr $\downarrow$ -Al and Cr $\uparrow$ -Al and Cr $\downarrow$ -Cr $\uparrow$  denotes short range order parameters of Cr $\downarrow$ -Cr $\uparrow$ .

Wurtzite B1										
	Shell 1		Shell 2		Shell 3		Shell 4		Shell 5	
AlN%	Cr-Al	Cr $\downarrow$ -Cr $\uparrow$								
0.875	0.05	-1.67	-0.14	1.00	-0.14	1.00	-0.02	-0.78	-0.14	1.00
0.750	-0.11	0.67	0.00	-1.00	0.33	-3.00	-0.11	0.56	-0.11	-0.33
0.625	0.02	-0.19	0.20	-1.67	-0.07	1.00	-0.01	0.01	-0.42	0.41
0.500	0.04	-0.33	-0.25	1.00	0.00	0.00	0.06	-0.33	-0.33	0.00
0.375	0.11	-0.28	-0.33	0.68	-0.07	0.36	0.11	-0.28	-0.42	-0.07
0.250	-0.06	0.07	-0.33	0.33	0.33	-0.33	-0.04	0.01	-0.11	-0.48
0.125	-0.05	-0.01	-0.14	0.02	-0.14	0.02	-0.02	-0.02	-0.14	-0.31
0.000		0.00		0.00		0.00		0.00		-0.33

---

# List of publications

---

The following is a list of my publications directly related to the topics of this dissertation. These papers were submitted for publication during the course of this research work.

## Publication I

First-principles study of elastic properties of cubic  $\text{Cr}_{1-x}\text{Al}_x\text{N}$  alloys.

Zhou L, Holec D, Mayrhofer P.H. J. Appl. Phys. 113, 043511 (2013).

<http://dx.doi.org/10.1063/1.4789378>

## Publication II

Ab initio study of the alloying effect of transition metals on structure, stability and ductility of CrN.

Zhou L, Holec D, Mayrhofer P.H. J. Phys. D: Appl. Phys. 46, 365301 (2013).

[doi:10.1088/0022-3727/46/36/365301](https://doi.org/10.1088/0022-3727/46/36/365301)

## Publication III

Structural stability and thermodynamics of CrN magnetic phases from ab initio calculations and experiment.

Zhou L, Körmann F, Holec D, Bartosik M, Grabowski B, Neugebauer J, Mayrhofer P H. Phys. Rev. B. 184102, 90 (2014)

---

<http://dx.doi.org/10.1103/PhysRevB.90.184102>

### **Publication IV**

Impact of point defects on the electronic structure of paramagnetic CrN

Holec D, Zhou L, Zhang Z, Mayrhofer P.H.

<http://arxiv.org/abs/1410.0758>

### **Publication V**

Structural and mechanical properties of nitrogen-deficient cubic Cr-Mo-N and Cr-W-N systems

Zhou L, Klimashin F, Holec D, and Mayrhofer P.H.

Manuscript prepared to submit.

### **Publication VI**

Alloying trends in quaternary Cr-Al-TM-N

Zhou L, Holec D, Mayrhofer P.H.

Manuscript in preparation.

---

## Other publications

---

Alloying-related trends from first principles: An application to the Ti-Al-X-N system.

Holec D, Zhou L, Rachbauer R, Mayrhofer P.H. J. Appl. Phys. 113, 113510 (2013).

<http://dx.doi.org/10.1063/1.4795590>

Alloy-based design of materials from first principles: An application to functional hard coatings

Holec D, Zhou, L, Rachbauer, R, Mayrhofer, P.H.

Book Chapter, Density Functional Theory: Principles, Applications and Analysis, 259-284 (2013).

Influence of ZrN on oxidation resistance of Ti-Al-N coating

Chen L, He L, Xu Y, Zhou L, Pei F, and Du Y. Surf. Coat. Technol, 87–91, 244 (2014)

[doi:10.1016/j.surfcoat.2014.01.063](https://doi.org/10.1016/j.surfcoat.2014.01.063)

Improved thermal stability and oxidation resistance of Al–Ti–N coating by Si addition

Chen L, Yang B, Xu Y, Pei F, Zhou L, and Du Y. Thin Solid Films, 369–375, 556 (2014)

[doi:10.1016/j.tsf.2014.01.072](https://doi.org/10.1016/j.tsf.2014.01.072)

---

# Curriculum Vitae

---

Name: **Liangcai Zhou**

Birth date: 15.12.1985

Birth place: Hunan, Chian

Nationality: China

Institute of Materials Science & Technology

Email: [zhlc1985@gmail.com](mailto:zhlc1985@gmail.com)

Technische Universit ä Wien

Mobile: 00436507401736

Getreidemarkt 9/E308, A-1060 Wien

## Education

- 2013-now Doctoral programme in Engineering Sciences, Technische Universit ä Wien, Austria.
- 2012-2013 Doctoral programme in Materials Sciences, Montanuniversit ä Leoben Leoben, Austria.
- 2008-2011 M.S. Materials Science, Central South University, Changsha, China.
- 2004-2008 B.S. Powder Materials Science and Engineering, Central South University, Changsha, China.

## Research Interests

- Materials response of nitrides.
- Surface and Interface calculation.
- Phase stability, mechanical and thermodynamical properties of bulk phases.

## Research Experience

Based on first-principles calculations and using Density Functional Theory (DFT) software VASP to study the materials properties of transitional metal nitrides. Through phonon calculations and taking lattice vibrations and thermal electronics into account within quasi-harmonic approach, studying the finite-temperature thermodynamic properties of the key metastable phases in the lightweight Al-based alloys. Constructing surface and interface model based on experimental observation to study the surface and interface existing in the alloys.

## Honors and Awards

- Li Xun Scholarship, Central South University, 2011.
- Deutscher Akademischer Austausch Dienst (DAAD) Scholarship to attend the 1<sup>st</sup>

---

International DAAD-Summer-Academy (Structure Formation – From a Cloud of Atoms to a crystal) in Chemnitz University of Technology from September 13-16, 2009.

- Huang Peiyun Education Scholarship, Central South University, 2008.
- First Prize of Scholarship, Central South University, 2004-2007.

## Publications

- First-principles study of elastic properties of cubic  $\text{Cr}_{1-x}\text{Al}_x\text{N}$  alloys. **Zhou L**, Holec D, Mayrhofer P.H. *J. Appl. Phys.* 113, 043511 (2013).
- Ab initio study of the alloying effect of transition metals on structure, stability and ductility of CrN. **Zhou L**, Holec D, Mayrhofer P.H. *J. Phys. D: Appl. Phys.* 46, 365301 (2013).
- Structural stability and thermodynamics of CrN magnetic phases from ab initio calculations and experiment. **Zhou L**, Körmann F, Holec D, Bartosik M, Grabowski B, Neugebauer J, Mayrhofer P.H. *Phys. Rev. B.* 184102, 90 (2014)
- Impact of point defects on the electronic structure of paramagnetic CrN  
Holec D, **Zhou L**, Zhang Z, Mayrhofer P.H. <http://arxiv.org/abs/1410.0758>
- Alloying-related trends from first principles: An application to the Ti-Al-X-N system.  
Holec D, **Zhou L**, Rachbauer R, Mayrhofer P.H. *J. Appl. Phys.* 113, 113510 (2013).
- Alloy-based design of materials from first principles: An application to functional hard coatings. Holec D, **Zhou L**, Rachbauer, R, Mayrhofer, P.H. Book Chapter, *Density Functional Theory: Principles, Applications and Analysis*, 1-322 (2013).
- Influence of ZrN on oxidation resistance of Ti-Al-N coating. Chen L, He L, Xu Y, **Zhou L**, Pei F, and Du Y. *Surf. Coat. Technol*, 87–91, 244 (2014)
- Improved thermal stability and oxidation resistance of Al–Ti–N coating by Si addition. Chen L, Yang B, Xu Y, Pei F, **Zhou L**, and Du Y. *Thin Solid Films*, 369–375, 556 (2014)
- Spatial and electronic structure of the Ni<sub>3</sub>P surface. **Zhou L**, Kong Y, Du Y, Wang J, Zhou Y. *Appl. Surf. Sci.*, 7692–7695, 256 (2010).

## References

Univ.Prof. Dipl.-Ing. Dr.mont. Paul Heinz Mayrhofer,

[paul.mayrhofer@tuwien.ac.at](mailto:paul.mayrhofer@tuwien.ac.at) +43 (1) 58801 30811

Dr. David Holec, david.holec@unileoben.ac.at +43 (0) 3842-4024211